FEATURE DETECTION ALGORITHMS IN COMPUTED IMAGES

A Thesis
Presented to
The Academic Faculty

by

Ali Cafer Gurbuz

In Partial Fulfillment
of the Requirements for the Degree
Doctor of Philosophy in the
School of Electrical and Computer Engineering

Georgia Institute of Technology
August 2008

FEATURE DETECTION ALGORITHMS IN COMPUTED IMAGES

Approved by:

Dr. James H. McClellan, Advisor
School of Electrical and Computer Engineering
Georgia Institute of Technology

Dr. Waymond R. Scott
School of Electrical and Computer Engineering
Georgia Institute of Technology

Dr. Justin K. Romberg
School of Electrical and Computer Engineering
Georgia Institute of Technology

Dr. Patricio A. Vela
School of Electrical and Computer Engineering
Georgia Institute of Technology

Dr. Brani Vidakovic
School of Industrial and Systems Engineering
Georgia Institute of Technology

Date Approved: 28 May 2008

To my love Sevgi,

my first born Alperen and

my dad Lutfi, mom Emine and sister Aysegul:

Thanks for your love, encouragement and support.

ACKNOWLEDGEMENTS

It has been said that "Even the best laid plans of mice and men always go astray." Upon starting the PhD program at Georgia Tech in Fall 03, little did I know that I would have much more in my mind than just engineering. After one semester at Tech, I met the girl who would one year later become my wife. Five months into our marriage, we found out she was pregnant, and nine months later our son Alperen was born. Busier than bee dealing with school and family, life took another unexpected turn when my mother-in-law suddenly passed away from a cancerous brain tumor that doctors failed to diagnose during the 4 months she was ill.

Throughout all the joy and sorrow, however, I was fortunate to have an advisor, Dr. James H. McClellan who supported and encouraged me all the way. He taught me how to create my own path, rather than defining one for me. He was a great mentor for me and will always serve as a role model in my life. Thus first and foremost I would like to thank my advisor Dr. McClellan for everything he has done and is.

I also would like to thank Dr. Waymond Scott helping me understand the physical reasons of the problems. His comments always helped me to improve my work. I would like to specially thank Dr. Justin Romberg who helped me a lot to understand the basics of Compressive Sensing which covers an important part of this thesis. I also would like to thank other committee members Dr. Patricio Vela and Dr. Brani Vidakovic taking their time to be in my committee.

I have so many friends to thank. First my project group mates: Mubashir Alam, Kangwook Kim, Pelham Norville, Tegan Counts, Gregg Larson. I have learned a lot rom each of you and I will never forget tons of stones we carried for our experiments. I would like to thank for my CSIP meeting group: Volkan Cevher, Rajbabu

Velmerugan, Milind Borkar, Faisal Shah, Quang Lee, Sam Lee and Yeangsoon Lee for your comments, ideas and presentations you made each week. My CSIP friends: Tarik Arici, Toygar Akgun, Umut Demircin, Ali Cengiz Begen, Zafer Aydin, Aytac Azgin, Salih Dikbas, Sibel Yaman, Osman Sezer, Ibrahim Pekkucuksen, Soner Ozgur. Thanks to you all for sharing this PhD life with me.

I am grateful to the CSIP staff, Tammy Scott, Lisa Gardner, and Catherine Gholson, for helping me solve my administrative problems. I would like to also thank our CSIP faculty that created this unique study environment.

Finally, I would like to thank to my family: Sevgi Zubeyde Gurbuz, my wife for always being there when I needed her or when I didn't need her. Without you this life would be without joy and happiness. I will always love you and be on your side through eternity. My special thanks goes to my son Alperen who provided us many sleepless nights to work for our PhDs :). I should also admit that without the love, he brought to our small family we wouldn't be able to go through all the things we did in the last several years. I also deeply thank Lutfi Gurbuz, my father who worked a lot for me to reach this point; Emine Gurbuz, my mother, who was my life support; Aysegul Gurbuz, my sister who trusted and encouraged me all the way. I would like to thank my grandmother Fatma Tezer for her deepest prayers. I would like remember and thank all the ones that would like to share this with me but wouldn't be here: my mother-in-law Nazmiye Ertan, my grandfathers Ali Gurbuz, Ismail Tezer and my grandmother Ayse Gurbuz.

TABLE OF CONTENTS

DEDICATION iii

ACKNOWLEDGEMENTS iv

LIST OF TABLES ix

LIST OF FIGURES x

SUMMARY xv

I INTRODUCTION 1

1.1 Subsurface Imaging Sensors 1

1.1.1 Existing Subsurface Imaging Algorithms 3

1.1.2 Problems with existing imaging methods and proposed solutions 5

1.2 Feature Detection Algorithms in Subsurface Images 6

1.2.1 Existing Feature Detection Algorithms 7

1.2.2 Hough Transform and Its Variations 8

1.2.3 Random Sample Consensus Based Algorithms 12

1.2.4 Regularized Feature Detection 13

1.3 Contributions and Organization of The Thesis 17

II COMPRESSIVE SENSING FOR SUBSURFACE IMAGING USING GPR 20

2.1 Compressive Sensing 21

2.2 Compressive Subsurface Imaging Using Impulse GPRs 24

2.2.1 Creating a dictionary for GPR data 24

2.2.2 Compressive Sensing Data Acquisition 26

2.2.3 GPR Imaging with Compressive Sensing 28

2.2.4 Selection of Algorithm Parameters 29

2.2.5 Discussion 31

2.2.6 A Simulated Imaging Example 35

2.2.7 Performance in Noise 38

2.2.8 Effect of the Measurement Matrix $\mathbf{\Phi}$ 39
2.2.9 Random Spatial Sampling 41
2.2.10 Experimental Results 43
2.3 Random Sampling for Stepped Frequency GPRs 48
2.3.1 Theory of Compressive Imaging for SFCW GPRs 50
2.3.2 Simulated Example for SFCW GPR Imaging 54
2.3.3 Performance in Noise 56
2.3.4 Random Spatial Sampling 58
2.3.5 Increased Resolution Property 60
2.3.6 Effect of Bandwidth 61
2.3.7 Experimental Results 62
2.4 Conclusions 65
III HOUGH TRANSFORM BASED FEATURE DETECTION 67
3.1 Iterative Detection of Linear Objects in GPR and Seismic Images . 67
3.1.1 Estimating Linear Object Area 68
3.1.2 Termination Criterion 70
3.1.3 Simulation Results 70
3.1.4 Experimental GPR and Seismic System for Detecting Tunnels 72
3.2 Detecting Curved Buried Features Using Partial Hough Transforms 76
IV DETECTING IMAGE FEATURES USING ADAPTIVE RANDOM SAMPLE THEORY 82
4.1 Feature Detection by Adaptive Random Sample Theory 85
4.1.1 Algorithm Steps 85
4.1.2 Selection of Algorithm Parameters 88
4.2 Results 90
4.2.1 Performance of the algorithm for different σ values: 91
4.2.2 Performance of the proposed method for varying SNR . . . 92
4.2.3 Experimental Data Results in 3D 93

V COMPRESSIVE SENSING OF PARAMETERIZED SHAPES 96
5.1 Shape Detection using Compressive Sensing 97
5.1.1 Selection of Algorithm Parameters 99
5.1.2 Detecting Linear Structures 100
5.1.3 Joint Detection of Circles and Lines 101
5.1.4 Performance in Noise 103
5.1.5 Test on Number of Compressive Measurements 104
5.1.6 Detecting Buried Pipes in Seismic or GPR Images 105
5.2 Shape Detection Using Compressive Sensor Measurements 107
5.2.1 Simulation Results 110
5.2.2 Experimental Results 112
VI CONCLUSIONS 115
REFERENCES 117
VITA 124

LIST OF TABLES

1 Randomized Hough Transform Algorithm 11

2 RANSAC Algorithm 13

3 Mutual Coherence for Different Types of Measurement Matrices . . . 40

4 Image variance with varying number of spatial samples for time domain GPRs 42

5 Image variance with varying number of spatial samples for stepped-frequency GPRs 59

6 True and Detected Target Parameters 91

7 Average Run Times (secs) of the Algorithms in 2D 93

8 Experimental Results with 3-D Data Comparing the ARST to the HT 95

LIST OF FIGURES

1 Photographs of the seismic and GPR sensors used in our experiments [25]. 3

2 Bistatic GPR measurement setup and impulse response of the GPR data acquisition process 4

3 Example backprojecton of a sample space-time domain GPR data taken over 4 buried targets 5

4 2D Hough Transform on seismic surface energy image 9

5 Example line detection using RANSAC 14

6 Example beamlets at various scales,locations and orientations 15

7 A beamlet decorated recursive dyadic partition (BD-RDP) and its associated tree structure. 16

8 Thesis Outline and Contributions 18

9 GPR measurement setup 25

10 Standard time samples vs. compressive samples of the a signal. 26

11 Possible implementation of compressive sensing data acquisition for impulse GPR. 27

12 Average of the 100 independent imaging assuming the propagation velocity is (a) 1×10^{10} cm/s, (b) 1.5×10^{10} cm/s, (c) 2×10^{10} cm/s, (d) 2.5×10^{10} cm/s. 32

13 Distance of the estimated target point from the true target location as a function of the assumed velocity. 32

14 Model GPR data (a) for a target at $(x, z) = (0, -8)$ using $v = 2 \times 10^{10}$ cm/s and (b) for a target at $(x, z) = (0, -4)$ using $v = 1 \times 10^{10}$ cm/s. 33

15 Two point targets in a homogeneous medium. 33

16 Normalized variability of the created images as a function of assumed velocity for three different transmitted pulses. The true velocity is taken as $v = 2 \times 10^{10}$ cm/s. 34

17 Simulated example for compressive sensing for target space imaging using Impulse GPR 36

18 (a) Variance on target positions vs. SNR. (b) Variance on the created images vs. SNR. Comparison with variance of SBP and the proposed method. M is the number of measurements at each aperture for the proposed algorithm. SBP measures the full space-time domain data which has 220 measurements for each aperture. 39

19 Variance vs. Measurement number for different types of random matrices. 40

20 Random spatial sampling result for impulse GPR 42

21 Photo and diagram of the experimental GPR system 44

22 (a) Experimental setup for GPR Imaging,(b) Space-time domain measured GPR Response of a $1''$ metal sphere in air. (c) Compressive measurements of the space-time domain data shown in (b) when different $\mathbf{\Phi}_i$ is used at each aperture i and (d) when same $\mathbf{\Phi}_i$ is used at each aperture i. 45

23 (a) Target space image found with CS imaging method using the measurement set in Fig. 22(c), (b) Target space image found using the measurement set in Fig. 22(d), and (c) Target space image found with standard time domain backprojection. 46

24 (a) Picture of the buried targets, (b) Burial map of targets in sand. The numbers in parentheses are the buried depths of the targets. . . 47

25 (a) Space-time domain GPR data for the $x = 0\,\text{cm}$ line scan of the burial scenario shown in Fig. 24. Image of the target space slice obtained by (b) backprojection and (c) compressive sensing. 47

26 The surface energy image created by (a) Backprojection,(b) Compressive sensing. (c) 3D isosurface (-30dB) image of the selected region in (b) by dashed lines. 48

27 GPR measurement setup 51

28 (a) Target space, (b) Noisy space-frequency domain target space response at $SNR = 10\,\text{dB}$ for 30 aperture points, (c) Black points indicate the randomly measured frequencies when 20% of the total frequencies are used, (d) Frequency domain backprojection image using all the space-frequency domain data from (b), (e) Frequency domain backprojection method using only the randomly selected 20%, (f) Solution obtained with the proposed method using (40). 55

29 (a) Target position variance vs. SNR. (b) Variance of the created images vs. SNR. Comparison between variances of BP and the CS method. M is the number of frequencies used. 57

30 (a) Space-time domain response of the target space to the GPR data acquisition process at randomly sampled spatial aperture positions, (b) Compressive measurements at the sampled aperture positions, (c) Target space image obtained with the proposed method, (d) Target space image obtained with time domain backprojection. 58

31 Increased resolution property results: (a) Backprojection (b) compressive sensing images when source separation is 10 cm. (c) Backprojection (d) compressive sensing images when source separation is 5 cm. . 60

32 Comparison of effect of the used bandwidth on the target space image created by both backprojection and the proposed method. (a), (b) and (c) are target space images created by BP at bandwidths of 1[3.5-4.5], 3[2.5-5.5] and 7[0.5-7.5] GHz respectively. (d),(e) and (f) are target space images created by PM at bandwidths of 1, 3 and 7 GHz respectively. 62

33 (a) Experimental setup for GPR Imaging,(b) Magnitude of the space-frequency domain measured GPR Response of a 1″ metal sphere in air. (c) Top image uses all space-frequency data and generated by backprojection. Middle and bottom images are random frequency selection results generated by backprojection and CS method. (d) Uniform frequency selection results. Circle on the images indicates the true location and size of the sphere. 64

34 Experimental data compressive sensing result 65

35 (a) Simulated linear object signature in seismic or GPR backprojected images, (b) Hough Transform of the image,(c) Estimation of y-crossing values for upper and lower bound lines, (d) Linear object length estimation 69

36 (a) Simulated image with two Tunnels, (b) Hough transform of image in (a), (c) Iteration 2 Image, (d) Hough transform of image in (c), (e) Iteration 3 image, (f) Hough transform of image in (e). 71

37 (a) Simulated image with two Tunnels and 3 clutter objects, (b) HT of image in (a), (c) Iteration 2 Image, (d) HT of image in (c), (e) Iteration 3 image, (f) HT of image in (e), (g) Iteration 4 image, (h) HT of image in (g), (i) Iteration 5 image, (j) HT of image in (i) 73

38 Positioning of buried targets in tunnel detection experiments 75

39 (a) Experimental seismic surface energy image, (b) HT of image in (a), (c) Iteration 2 Image, (d)HT of image in (c), (e) Iteration 3 image, (f) HT of image in (e). 76

40 (a) Experimental GPR surface energy image, (b) HT of image in (a), (c) Iteration 2 Image, (d) HT of image in (c). 77

41 Estimating a curve from partial linear approximations 78

42 (a) Processing results with HT and PHT detected for the noise-free case. (b) Detected structures for HT and PHT on a 20-dB surface energy image. 80

43 1/MSE for varying SNR and batch size values. 81

44 (a) Randomly selected strip region, (b) Parameter space corresponding to the strip region in (a). 87

45 (a) Two Linear features, (b) Detected lines from Stage I (random selection) and Stage II (refined by the HT) of the proposed algorithm on the noisy image of SNR 0 dB. 90

46 (a) Average run time of stage I of the algorithm versus σ/s_i where s_i is the size of the image and 100 for this simulation. (b) Average run time of stage II of the algorithm, (c) Total average run time of the algorithm. 92

47 Probability of detection (P_D) vs. SNR for the compared feature detection algorithms. 93

48 Positioning of buried targets in tunnel detection experiments 94

49 (a) 3D iso-figures at -15 dB of the 4" tunnel using the GPR sensor measurements. Dashed and solid lines show the detected lines for HT and ARST method respectively. 95

50 (a) Image showing true line locations, (b) Noisy image with additive white Gaussian noise ($\sigma = 0.5$), (c) Compressive measurements, (d) Parameter space image obtained with ℓ_2-norm minimization, (e) Hough Transform using all the image pixels, (f) ℓ_1-minimization using the Dantzig Selector. 100

51 Joint Line and Circle Detection 102

52 (a) Noisy image with additive white Gaussian noise ($\sigma = 0.2$), (b) Results from ℓ_1-minimization of the Dantzig Selector. 103

53 Detection ratio vs. SNR. K is the number of random projections. . . 104

54 Detection ratio vs. measurement number for varying types of random matrices (Solid, dashed and diamond marked dotted lines correspond to 1, 2, and 3 targets respectively). 105

55 (a) Experimental Backprojected Seismic Image, (b) Hough Transform of the backprojected image, (c) Compressive measurements created by projections of the image in (a) to random Gaussian vectors, (d) The least squares solution. 106

56 Parameter space created by the CS shape detection algorithm. 107

57 Experimental data compressive sensing result 108

58 Compressive sensing for target space imaging 111

59 (a) 400 CS measurements, (b) Solution obtained with the proposed method using (67). 111

60 (a) Model in the sand tank of a 10 cm tunnel buried approximately 58–60 cm deep from the surface, (b) Backprojected image using all the space-time raw GPR data. The line drawn is obtained from (d). (c) HT of the image shown in (b), (d) Parameter space obtained by the proposed method. 113

SUMMARY

This thesis focuses on algorithms to create images of sensed media and to detect features in those images. We are mostly interested in generating subsurface images and detecting targets like landmines, tunnels, pipes and so on. Ground penetrating radar (GPR) and the seismic sensor are the basic sensors used to probe the subsurface area.

For subsurface imaging we introduce a new data acquisition and imaging method based on spatial sparsity of the target space, i.e., a small number of point like targets. We show that the target space image can be constructed using a much smaller number of non-adaptive linear measurements by solving an ℓ_1 minimization problem when the target space is sparse. This new imaging method creates less cluttered images and uses fewer measurements which leads to lower data acquisition times. The algorithm has been developed for both time-domain and stepped- frequency GPRs.

For detecting structures like tunnels or pipes in the subsurface images, the Hough transform (HT) is a widely used method. The HT uses a parameterized model of each feature to transform it into a parameter space where detection is easier. Although the HT is capable of detecting parameterized shapes, it suffers from several problems.

First, the HT can detect only known parameterized shapes. To detect curving structures partial Hough transform (PHT) was developed. Second, problems of detecting very weak features hidden by high clutter or noise, which can not be directly detected by the HT, were solved through iterative detection and removal of objects. A third problem with the HT is its high computational cost. Several existing methods which were aimed at reducing the computational cost of the HT also suffer a loss in performance compared to the full HT, or can only be applied to binary images. A

feature detection algorithm based on random sample theory was developed to detect features in highly noisy images faster than the HT and without the degradation in performance suffered by existing algorithms.

Most feature detection methods require the existence of a computed image before doing any kind of detection. However, we were able to combine the compressive sensing (CS) ideas with the information about sparseness of shapes in the parameter space to define a new method that can directly form the parameter space result without creating the target space image using fewer compressive measurements. All the algorithms developed in this thesis were tested on both computer simulated data and experimental data to validate their performance.

CHAPTER I

INTRODUCTION

In recent years, there has been great interest in detecting and imaging subsurface targets in a wide variety of areas such as civil engineering [43], landmine detection [40, 37, 45], archeological investigations[81] and environmental applications [58]. Various sensing tools have been used to get better performance in different situations. The main sensors used are electromagnetic induction (EMI), ground penetrating radar (GPR), seismic and infrared (IR) sensors. These sensors rely on different operating principles and provide different levels of information about the sensed medium based on their capabilities. An EMI sensor is sensitive to conductivity and basically is used to find objects with metallic content. IR is attractive for its high standoff distance sensing. Seismic sensors are sensitive to the mechanical properties of objects. GPR has been shown to be an efficient subsurface imaging tool due to its low cost non-destructive capability of detecting both metal and non-metal objects. In this thesis we will be mostly focusing on creating subsurface images and detecting features in these images using GPR and seismic sensors.

1.1 Subsurface Imaging Sensors

Ground-penetrating radar (GPR) is a geophysical method that uses electromagnetic radiation in the microwave band of the radio spectrum, and detects the reflected signals from subsurface structures. GPRs often use bistatic or multistatic antennas. Bistatic systems use two different antennas separated by a fixed distance, one for transmitting and one for receiving. A multistatic system is a combination of several bistatic pairs at varying separations.

In traditional impulse GPR the transmitting antenna radiates short pulses of

the high-frequency EM waves into the ground. When the wave encounters a buried object or a boundary with different dielectric properties it reflects and is received by the receiving antenna. Another type of GPR which is becoming increasingly popular is the stepped frequency continuous waveform (SFCW) GPR [59, 75]. A stepped-frequency signal probes the environment with a discrete set of frequencies. A stepped frequency GPR has several advantages over an impulse GPR. The main advantage is the greater measurement accuracy inherent in a frequency domain system. For example, since it is much easier to synthesize a pure tone at a given frequency than it is to measure a time delay, the accuracy with which the frequencies are set in the SFCW GPR is much greater than the measurement times used in an impulse GPR. The operating frequency range can be adjusted to suit the specific ground conditions. For example, the low-frequency range can be used for relatively deep targets while higher frequencies are used for shallow objects. The dwell time at each aperture point and for each frequency before the GPR steps up the next frequency depends on several issues, such as the switching time for the sources, time to allow the transmitted signal to reach the receiver from a chosen maximum range, and time for the receiver to build up sufficient signal to noise ratio.

The seismic system might consist of an aero-acoustic source and a ground contacting receiver. Seismic waves are sensitive to the differences between the mechanical properties of an object and the soil. The acoustic source and receiver are scanned across the surface. The general principle is to send sound energy waves into the ground, and then interfaces between regions and objects having different mechanical properties reflect back this energy. The reflected energy is captured by the ground contacting receivers. Received signals are processed to detect objects, changes in material, voids and cracks. Photographs of the sensors used for different experiments are shown in Fig. 1.

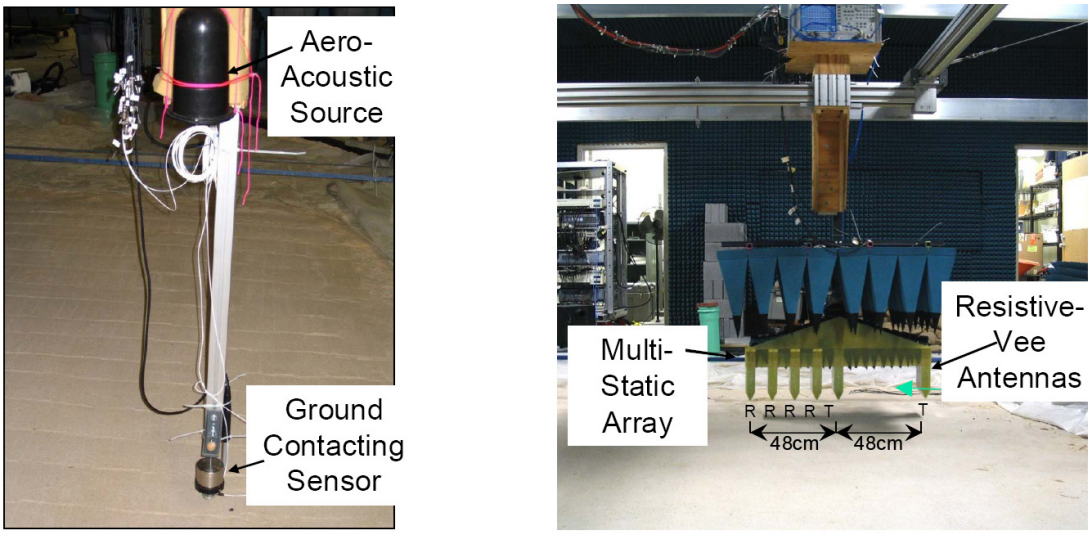

Figure 1: Photographs of the seismic and GPR sensors used in our experiments [25].

1.1.1 Existing Subsurface Imaging Algorithms

Subsurface imaging algorithms for seismic and GPR sensors are similar and depend on the data acquisition process. Standard imaging algorithms for both types of sensors do matched filtering of the measured data with the impulse response of the data acquisition process for each spatial location. Here we will give a brief summary using GPR as an example.

As the GPR antenna scans a region, the radar transmits and receives a series of pulses. Although the response of targets can be quite complex, it can be assumed that the received signal reflected from a point target at p is a time delayed and scaled version of the transmitted signal $s(t)$, i.e.,

$$\zeta_i(t) = As(t - \tau_i(p)) \tag{1}$$

where $\tau_i(p)$ is the total round-trip delay between the transmitter and the target at position p for the ith receive aperture point, and A is a scaling factor used to account for any attenuation and spreading losses.

Calculation of τ_i requires knowledge of the path the wave travels from the transmitter antenna to the target and then to the receiver, as well as the wave velocities in the media. An example bistatic GPR scenario is shown in Fig. 2(a). At the boundary

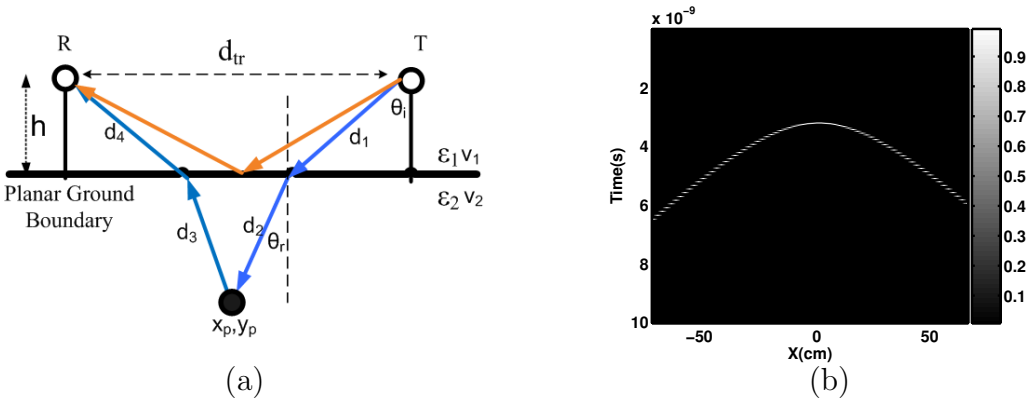

Figure 2: (a) GPR measurement setup showing a bistatic scenario, (b) Impulse response of the GPR data acquisition process for a single point target.

between two different media (such as air and soil), the propagation direction changes according to Snell's law. Taking wave refraction into account is especially critical for near-field imaging problems such as mine detection since the distance between the antenna and the target is relatively small. The exact calculation of the refraction point requires the solution of a 4th degree polynomial. Several approximations to compute the refraction point are available [62]. After finding the refraction points, the distances $d_{1:4}$ shown in Fig. 2(a) are known and the τ_i times can be calculated as

$$\tau_i = \frac{d_1 + d_4}{v_1} + \frac{d_2 + d_3}{v_2}. \tag{2}$$

The GPR transmissions spanning a region of interest form a synthetic aperture, whose impulse response follows a spatially variant curve in the space-time domain. Figure 2(b) shows the response of the GPR synthetic aperture data acquisition process for a single point target.

Standard imaging algorithms do matched filtering of the measured data with the impulse response of the data acquisition process (Fig. 2(b)) for each spatial location.

Time-domain standard backprojection (SBP) [37, 76, 62] can be formulated as follows.

$$f(x_n, y_n, z_n) = \iint w(u_x, u_y) d(u_x, u_y, t) \delta(t - \tau(u_x, u_y, z_n)) dt du_x du_y, \tag{3}$$

where $d(u_x, u_y, t)$ is the measured GPR space-time data, $w(u_x, u_y)$ is the aperture weighting function, $f(x_n, y_n, z_n)$ is the created subsurface image, and $\tau(u_x, u_y, z_n)$ is the total time delay from the antenna to the imaging point (x_n, y_n, z_n) and back to the receiver. Frequency domain imaging algorithms [42, 86] also apply a similar matched filtering operation in the space-frequency domain. An example of subsurface imaging is shown in Fig. 3. Figure 3(a) shows the space-time domain raw GPR data taken

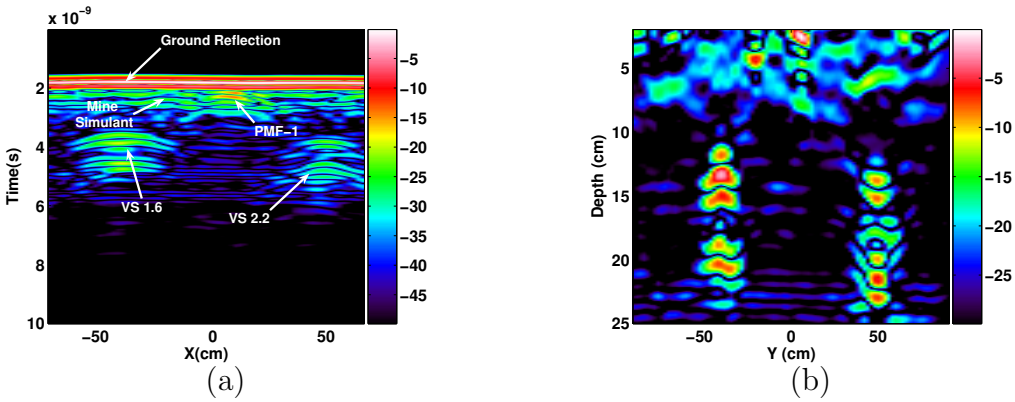

Figure 3: (a) Space-time domain raw GPR data taken over 4 targets. One VS 1.6 and one VS 2.2 antitank mines, one mine simulant and one PMF-1 mine. (b) Backprojected subsurface image.

over four targets. The buried targets are VS-1.6 and VS-2.2 antitank mines, one mine simulant and a PMF-1 mine. Hyperbolic signatures of the targets are apparent in the measured raw data. However, the targets are more clear and visibly quite pronounced in the backprojected image shown in Fig. 3(b).

1.1.2 Problems with existing imaging methods and proposed solutions

All of the existing imaging algorithms require fine spatial sampling and Nyquist rate time sampling of the received signals. It is not possible to exploit any prior information about the target space with the current imaging method framework. Also, the

data acquisition times are very high which becomes a bottleneck in most GPR imaging systems. For example, in [24] it is reported that scanning a $1.8 \times 1.8\ m^2$ area with 2 cm spatial resolution and using 401 frequency steps takes approximately 14 hours. Thus there is a need for a new data acquisition and imaging algorithm that would decrease the number of measurements without degrading the imaging performance.

In this thesis, we present a novel data acquistion and imaging algorithm for GPRs that significantly reduces the data acqustion time and creates less cluttered target space images compared to standard imaging methods. The method depends on a basic assumption of spatial sparsity. Generally potential targets cover a small part of the total subsurface volume to be imaged. Thus we exploit *a priori* information that the target space is sparse. This fact is not exploited by the standard imaging methods. Spatial sparsity means that the number of targets is much less than the total number of spatial positions. Recent results in compressive sensing (CS) [31, 15, 4] provide the theory of how a sparsely representable signal can be sampled with a very few measurements and reconstructed. We apply the ideas from CS to the problem of subsurface imaging and show that less cluttered target space images can be constructed using many fewer measurements compared to standard imaging techniques. This part of the thesis is detailed in Chapter 2.

1.2 Feature Detection Algorithms in Subsurface Images

Feature detection requires the extraction of necessary information about a feature from an image by means of signal processing tools. It is an important and broad topic extensively studied in areas like image processing [61, 28], computer vision [23, 61] and subsurface imaging [51, 29]. This thesis focuses on detection of underground structures like tunnels or pipes in subsurface images. This is a problem of great interest in industrial and civil engineering, as well as military applications. Reliable feature detection in subsurface images with a reasonable false alarm rate is a hard

problem due to changing environmental conditions. Soil is a complex, lossy, and very inhomogeneous media. Many of the inhomogeneities in the soil such as layering, moisture variations, rocks, roots, etc. can cause a sensor to give false alarms. Research on buried linear object detection has focused on cross bore-hole tomography [84], neural detection of linear signatures [41], and a variety of techniques applying the Hough Transform to both GPR and seismic data [87, 51, 29].

In Chapter 3 and 4 varying Hough Transform (HT) algorithms are developed for subsurface feature detection problem. Partial Hough Transform (PHT) is used to detect curving structures. Very weak features hidden by high clutter and noise are detected by iterative detection and removal of objects. Chapter 4 introduces a new feature detection algorithm based on random sample theory reducing the computational cost of HT without the degradation in performance suffered by existing algorithms. Finally, Chapter 5 uses ideas from compressive sensing and sparsity of shapes to define a new method that can directly form the parameter space from a small number of sensor measurements without forming an image of the medium. Next we briefly summarize some of the existing feature detection algorithms.

1.2.1 Existing Feature Detection Algorithms

Feature detection in images has been extensively studied and many different kinds of algorithms have been developed. We will give a brief summary of the major feature detection algorithms related to our problem in three categories:

1. The Hough Transform (HT) and its variations
2. Random Sample Concensus (RANSAC) Based Algorithms
3. Regularized Feature Detection

1.2.2 Hough Transform and Its Variations

The Hough Transform (HT) [56], its variants and their generalizations [7, 35, 3, 61] are the most commonly used methods capable of detecting lines [35], circles [3], or any other parameterized curve [87]. A good reference for the HT and its generalizations is given by Illingworth and Kittler [61].

The HT uses a parameterized model of each feature (i.e., lines, curves or planes) to transform the feature in the original image space into a single mesh point in the parameter space. The better a feature corresponds to the model, the more values (also called votes) will be accumulated at a mesh point. Features having votes above a predetermined threshold are selected as a detection. One way of parameterizing a line is by selecting its slope m and intercept n values. Using these parameters a line can be defined as

$$y = mx + n. \tag{4}$$

Using the line parametrization in (4) the HT of an image $f(x, y)$ can be defined as follows:

$$\hat{f}(m, n)] = \int_{-\infty}^{\infty} f(x, mx + n)dx. \tag{5}$$

Each parameter pair (m, n) represents a line in the image. The HT does line integrals on the image for all possible parameter values. The problem of detecting a shape in the image domain is transformed into detecting a peak in the parameter domain by the Hough Transform, which is easy to implement.

Another widely used form of line parametrization was introduced in [35]. A straight line in a 2D image can be parameterized with (ρ, θ) as

$$\rho = x \cos\theta + y \sin\theta. \tag{6}$$

The HT with the line representation in (6) is written as

$$\hat{f}(\rho, \theta) = \int_{-\infty}^{\infty} \int_{-\infty}^{\infty} f(x, y)\delta(\rho - x\cos\theta + y\sin\theta)dxdy. \tag{7}$$

Another way of writing (8) is often used for implementation purposes.

$$\hat{f}(\rho,\theta) = \int_{-\infty}^{\infty} f(\rho\cos\theta - s\sin\theta, \rho\sin\theta + s\cos\theta)ds, \tag{8}$$

where the s-axis lies along the line.

As an example we consider the image in Fig. 4(a) which is formed by summing the energy values over all depths from backprojected seismic data for the tunnel detection experiment presented in Chapter 4. Applying the 2D Hough Transform gives the parameter domain image shown in Fig. 4(b). The two local maxima in the Hough domain image correspond to the two lines shown in the image space.

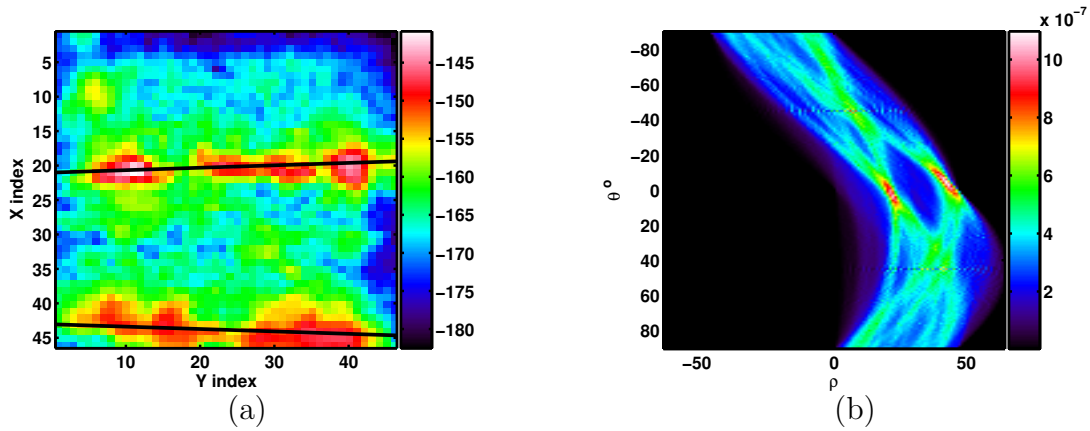

Figure 4: (a) Surface Energy Image and detected lines, (b) Hough Transform of the image in (a)

From the surface energy image (Fig. 4(a)), the depth information of the tunnel cannot be obtained. To determine how the tunnel is positioned in 3D world coordinates, a 3D HT should be used. In 3D (e.g., subsurface) images, a line can be represented by $r = r_0 + s\tau$, where s is a free parameter and r_0 is an offset vector, given as $r_0 = u\alpha + v\beta$ [87]. Here α, β and τ are

$$\tau = \begin{pmatrix} \cos\theta\cos\phi \\ \sin\theta\cos\phi \\ \sin\phi \end{pmatrix} \quad \alpha = \begin{pmatrix} -\sin\theta \\ -\cos\theta \\ 0 \end{pmatrix} \quad \beta = \begin{pmatrix} -\cos\theta\sin\phi \\ -\sin\theta\sin\phi \\ \cos\phi \end{pmatrix} \tag{9}$$

In other words, a line in 3D can be specified with the four parameters α, β, u, and v. A line in the original image corresponds to a point in HT space, where its intensity is determined by the sum of co-linear points in the image. The 3D Hough Transform can be formulated as the following line integral:

$$\hat{f}(\theta, \phi, u, v) = \int_{-\infty}^{\infty} f(s\tau + v\beta + u\alpha)ds. \tag{10}$$

Line detection is accomplished by finding local maxima in the HT parameter space. The 3D results from experimental seismic and GPR tunnel detection data are given in Chapter 4.

Although the HT is a basic algorithm effective even for very noisy images, it is not easily implementable because of its high computation time and large memory requirements. These problems are exacerbated as the dimension of the search space increases. The computational complexity for the HT for 2D images of size $N \times N$ is $O(N^3)$, and the complexity increases to $O(N^5)$ for 3D images.

Various methods have been proposed to decrease the computation requirements of the HT while computing a transform similar to the HT. The primary ones are the Probabilistic Hough Transform (PHT) [67], the Randomized Hough Transform (RHT) [91], and Line Detection using Random Sample Consensus (RANSAC) [38, 70, 21]. Although these methods provide faster solutions than the standard HT, they suffer in performance compared to the HT in noisy images, or can only be applied to binary images.

1.2.2.1 Randomized Hough Transform (RHT)

The RHT randomly selects n points from the image, corresponding to the number of points required to define a given feature, and then uses this subset to solve for the feature parameters. As an example, since a line can be defined by 2 points, $n = 2$ in line detection. The corresponding point in parameter space is then increased, and the process repeated for a predetermined number of iterations. Pseudo code for the

RHT is given in Table 1.

Table 1: Randomized Hough Transform Algorithm

Randomized Hough Transform (RHT)

While $k < k_{max}$

1. Select n-tuple of points from the image randomly
2. Solve for the parameters of the feature which is defined by the selected points
3. Accumulate the corresponding parameter space cell by the image pixel values of the points in 1.

The RHT in its original form [92, 91] is suitable only for binary images, but the idea can be expanded to all kinds of images. This can be done by increasing the parameter space cell by the pixel values of the randomly selected points instead of increasing by one for binary images. Although it has been shown that the RHT performs faster than the HT [92], for high noise or excessive outlier conditions the RHT is not robust.

1.2.2.2 Probabilistic Hough Transform (PHT)

The PHT [67] tries to decrease the computational requirements of the HT by randomly selecting a subset of the original data and applying the HT only to the selected part. This technique leads to erroneous results for a small subset, and selection of the optimum subset size requires knowledge of the image. Although the latter problem is solved by the Progressive PHT (PPHT) algorithm [74], performance is still worse than the HT. The RHT is suitable for low noise images [68]. For highly noisy images, the PHT outperforms the RHT; but neither algorithm works very well in detecting buried features in extremely noisy subsurface images.

1.2.2.3 Hierarchical Approaches to Hough Transform

In the literature there are also fast HT methods based on a hierarchical division of parameter space. The fast Hough Transform (FHT) in [69] recursively divides the parameter space into hypercubes and performs the HT only on the hypercubes with votes exceeding a selected threshold. The decision on whether a hypercube receives a vote from a hyperplane depends on whether the hyperplane intersects the hypercube. The method is applicable only to binary images and selection of the threshold to prune a hypercube in parameter space is a problem. The adaptive HT in [60] uses an idea similar to the FHT, but iteratively changes the size of the accumulation array to reduce memory requirements. The multiresolution HT [2] uses multiresolution images and accumulation arrays to compute the HT. Although the existing hierarchical HT methods succeed in decreasing the computational load of the HT, they can be applied to binary edge images and have problems associated with pruning a parameter space.

1.2.3 Random Sample Consensus Based Algorithms

Random Sample Consensus (RANSAC), introduced by Fishler and Bolles [38], is a hypothesis generation and verification algorithm for robust estimation of features. As with the RHT, RANSAC begins by randomly selecting n points from the image to generate a candidate model of the desired feature, where n corresponds to the number of points required to define a given feature. RANSAC then classifies all points either as "inliers" that fall within a certain distance of the candidate model, or as "outliers" which are discarded. If the number of inliers exceeds a preset threshold, the inliers are used to re-estimate the feature model. Pseudo code for RANSAC is given in Table 2.

As an example, consider the problem of finding the parameters of a line that approximates the points in Fig. 5(a). The threshold for the inlier set is selected as 10. At each trial 2 points that define a line are randomly selected and the number

Table 2: RANSAC Algorithm

RANSAC Algorithm

1. Set $k = 0$, while $k < k_{max}$ do the following
2. Randomly select p "white" points from the binary image and generate the candidate model which is defined by the selected points
3. Determine the number of inlier points n which are within σ distance of the candidate model
4. If number of inliers n is above a preset threshold T_n, re-estimate the model only using inlier points and terminate
5. $k = k + 1$

of inlier points, which are within a predetermined distance to the selected line, are counted. In the cases shown in Figs. 5(b) and (c) the inlier threshold is not exceeded. However, in Fig. 5(d) the threshold is met and the inlier point set is determined. A more accurate estimate of the line is obtained by estimating the line parameters using only the points in the inlier set, excluding the bad effects of outliers as shown in Fig. 5(e).

RANSAC has been shown to be effective for line detection in binary images [70, 21, 20]. It is a desirable method for its robust and faster estimation results. However, the distance calculations and the structure of the algorithm in its original form make it unusable for non-binary images as subsurface images.

1.2.4 Regularized Feature Detection

One of the latest advances in feature detection is to formalize the shape detection problem within a regularization framework and enhance the performance of a Hough based feature detector through the incorporation of prior information in the form of regularization. In [1] several types of regularization, including maximum entropy, ℓ_p with $p \leq 1$, and log regularization ,are discussed for the problem of line detection. The regularizers used actually favor sparsity in the parameter space. Although these

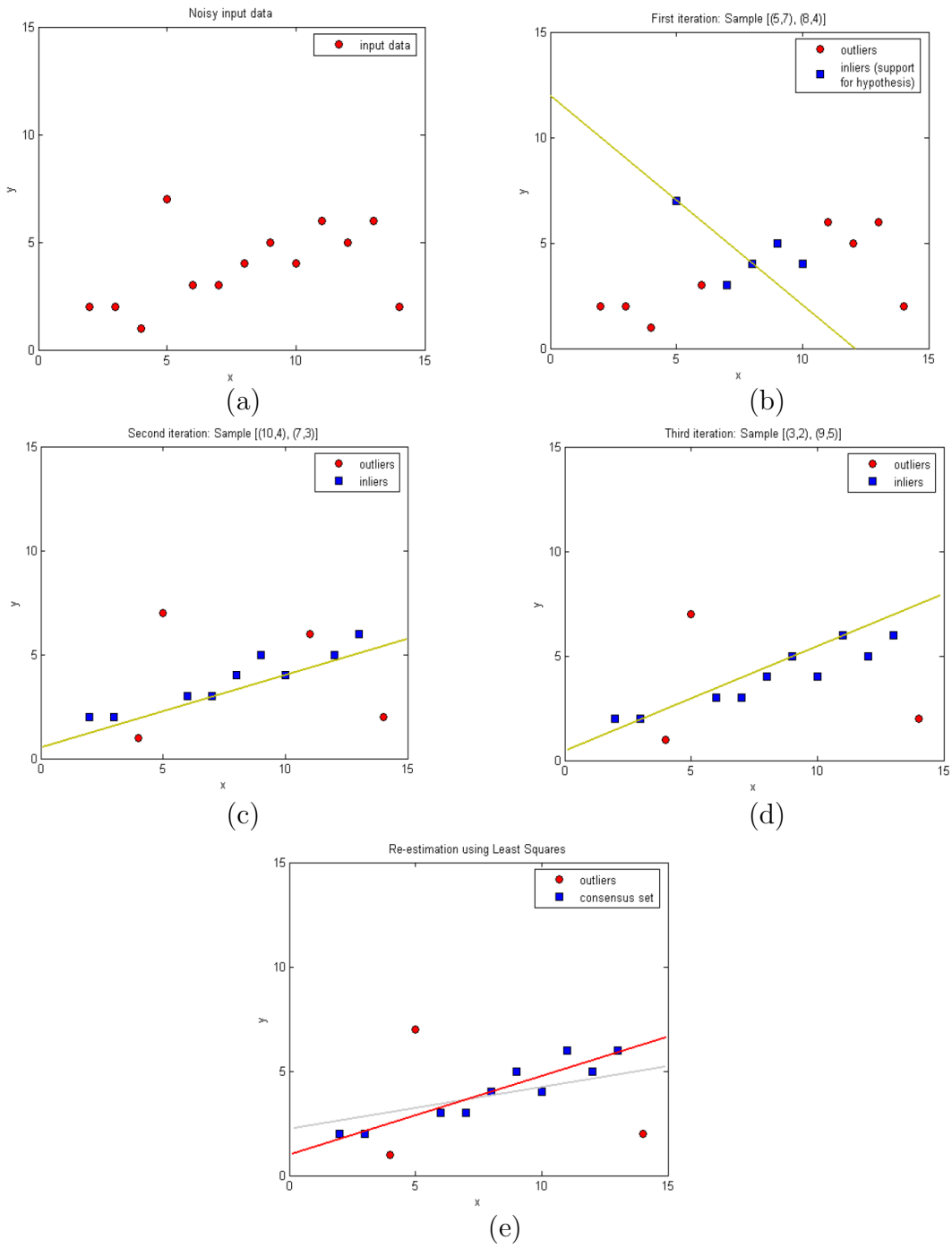

Figure 5: Finding line parameters using RANSAC.

methods increase the computational cost and for some cases don't guarantee a global optimum, they generate much cleaner or sparser parameter space results.

1.2.4.1 Beamlets and Multiscale Image Analysis

For analyzing images in a multiscale framework, beamlets were developed by Donoho and Huo [30, 32]. Beamlets are line segments and the beamlet dictionary is a dyadically organized collection of line segments, occupying a range of dyadic locations and scales, and occurring at a range of orientations. The beamlet transform of an image $f(x, y)$ is the collection of integrals of f over each segment in the beamlet dictionary; the resulting information is stored in a beamlet pyramid. Figure 6 shows four beamlets at various scales, locations and orientations.

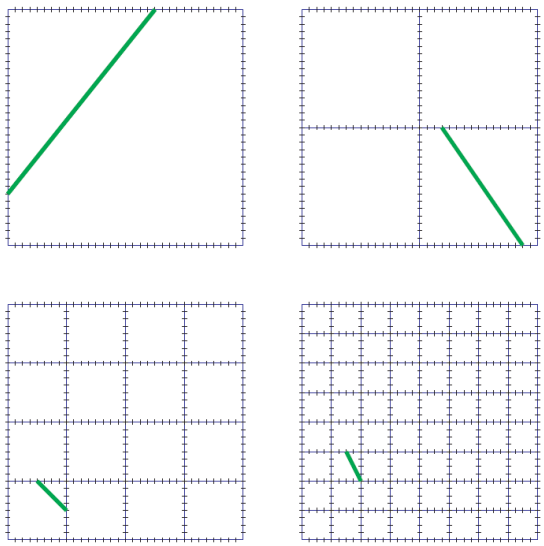

Figure 6: Four beamlets at various scales, locations and orientations

The beamlets offer an overcomplete representation of shapes since any beamlet in a stage can be written as a combination of other beamlets in another stage. One advantage of beamlets is that the chains of beamlets offer sparse approximate representations of curves in the image.

Several feature detection algorithms using beamlets have been developed. The first type of algorithm depends on simple thresholding of the beamlet coefficients without taking into account interconnections that might exist between the beamlets

at different scales and locations. The comparable statistic is

$$Y = \max T_y(b)/\sqrt{L(b)} \tag{11}$$

where $T_y(b)$ is the beamlet transform of the data y and $L(b)$ is the Euclidean length of the beamlet b. A beamlet is detected whenever Y exceeds a certain threshold.

A second type of algorithm [30] exploits the tree-structure of the recursive dyadic partitioning (RDP) underlying the beamlet pyramid. Figure 7 gives an example beamlet RDP and its associated tree structure. To extract multiple line fragments

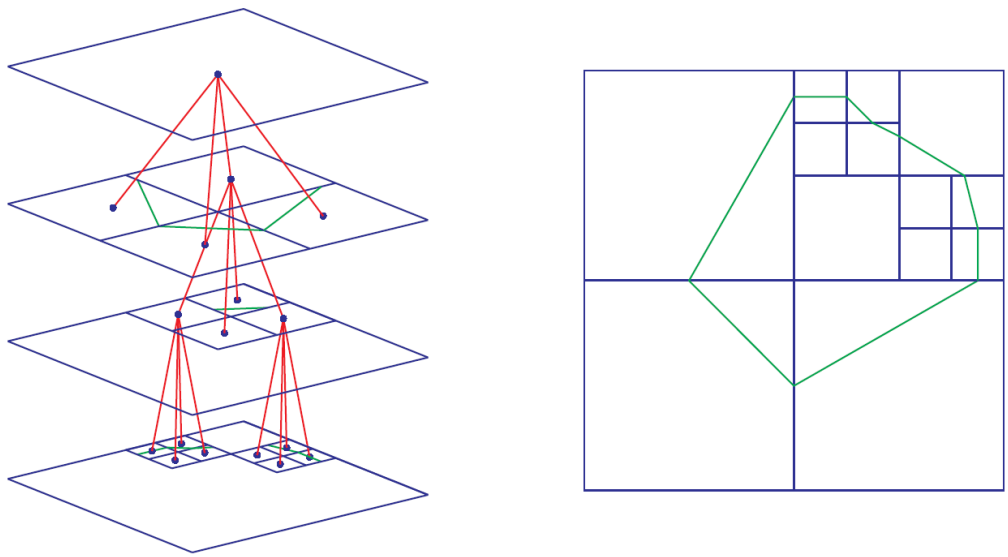

Figure 7: A beamlet decorated recursive dyadic partition (BD-RDP) (right) and its associated tree structure (left).

a search for a beamlet RDP solving an optimization problem is done. Each dyadic square S is associated with a quantity C_S defined as

$$C_S = \max_{b \sim S} T(b)/\ell(b)^{1/2} \tag{12}$$

where $T(b)$ is the beamlet coefficient associated to beamlet b, $\ell(b)$ is the length of b, and $b \sim S$ means that the beamlet b is associated to S. Then the partition over all recursive dyadic partitions P, that maximizes the complexity-penalized energy

$$J(P) = \sum_{S \sim P} C_S^2 - \lambda \# P \tag{13}$$

is obtained as the resultant feature where $\#P$ gives the number of partitions. Using this type of optimization or other algorithms that take into account neighboring beamlets, connectedness and directional continuation, beamlets can find lines, curves or regions in the images [32, 30].

In this thesis we develop methods to connect regularized feature detection to the problem of sparse signal representation and adaptive representation of signals in terms of the elements from an over-complete dictionary of possible features in a compressive sensing framework. Thus linear or curving features in subsurface images could be detected using a small number of measurements from the sensors.

1.3 Contributions and Organization of The Thesis

This thesis focuses on algorithms to create images of sensed media and to detect important features in the created images. In Fig. 8, a graphical outline of the thesis is given in which the major contributions are highlighted. These are discussed in this section. The figure should give the reader an overall picture of the results presented in the later chapters of the thesis.

Chapter 2 develops a new subsurface imaging method based on spatial sparsity of target space, i.e., a small number of point like targets. It is shown that the target space image can be constructed using a much smaller number of non-adaptive linear measurements by solving an ℓ_1 minimization problem, if the target space is sparse. This new imaging method creates less cluttered images and uses many fewer measurements which should lead to lower data acquisition times. The algorithm is developed for both time-domain and stepped-frequency GPRs.

Chapter 3 introduces solutions to two problems associated with the HT. The first one is that the HT can detect only known parameterized shapes. To detect curving structures, the partial Hough transform (PHT) is developed. Secondly, problems like detecting very weak features hidden by high clutter or noise which cannot be directly

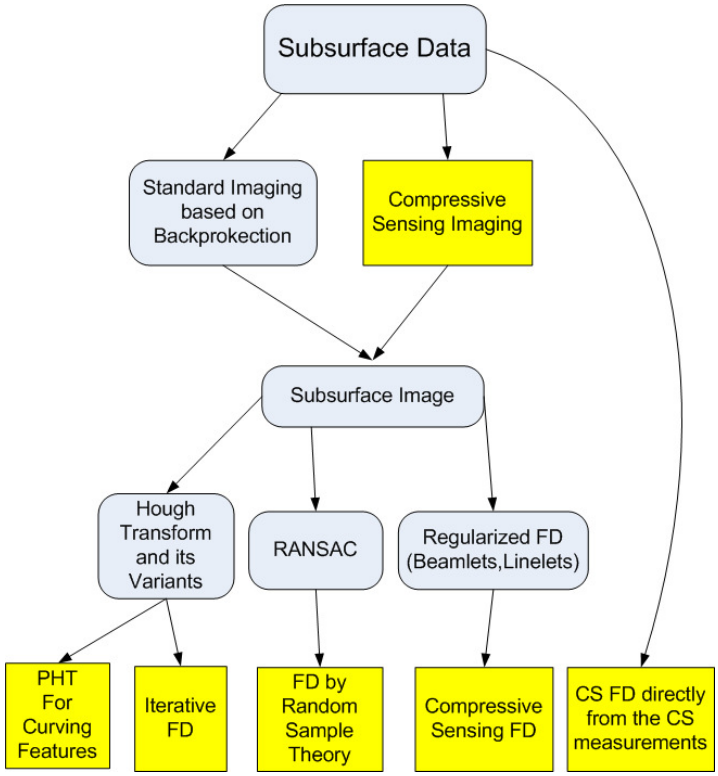

Figure 8: Thesis outline. New contributions are shown in the rectangular boxes.

detected by the HT are solved through iterative detection and removal of objects.

Chapter 4 introduces a new feature detection algorithm suitable for gray-scale images (i.e., computed subsurface images) using adaptive random sample theory. The developed method creates random hypothesis features by an adaptive sampling scheme and tests them to select candidate features in the image. The selected candidate features are then re-estimated within a smaller search space. Results show that the proposed algorithm can detect features accurately and much faster than the HT without the degradation of existing faster HT variants.

Chapter 5 introduces a new method based on compressive sensing for finding parameterized shapes in images. The method exploits the sparseness of parameterized shapes in the HT domain and uses a very small number of linear measurements of the image. Joint detection of different features can be done by using an extended

dictionary of possible shapes. This method requires the measurement of linear projections of the image. In the second part of the chapter, ideas from the subsurface imaging presented in Chapters 2 are combined with the developed compressive feature detection method using the compressive sensing framework to directly find the shape parameters from the minimal number of raw sensor measurements without forming an image of the subsurface area. Finally, Chapter 6 summarizes the main contributions of this thesis and discusses future directions for this research.

CHAPTER II

COMPRESSIVE SENSING FOR SUBSURFACE IMAGING USING GPR

Ground Penetrating Radars (GPR) image subsurface structures by transmitting electromagnetic waves into the ground and processing the reflections [26]. The traditional impulse GPR is a commonly used type of GPR due to its simple design and low cost [27]. It radiates a sequence of short pulses and processes the reflections. Another type of GPR that is becoming increasingly popular is the stepped-frequency continuous-wave (SFCW) GPR [59, 75]. A stepped-frequency signal probes the environment with a discrete set of frequencies. The main advantage of a SFCW GPR is the greater measurement accuracy inherent in a frequency domain system and the flexibility to adjust the operating frequency range to suit the specific ground conditions.

For both types of GPR the total subsurface response, formed from a combination of the responses from all reflectors within the medium, can be inverted using various imaging algorithms; e.g., time-domain Standard Backprojection (SBP) [37], and Fourier domain Synthetic Aperture Radar (SAR) image formation techniques [86, 42]. All of these algorithms require fine spatial sampling and Nyquist-rate time sampling of the received signals, or a high number of frequency measurements. Then they perform matched filtering with the impulse response of the data acquisition process to form an image. Most of the existing imaging algorithms don't use any prior knowledge about the image such as the spatial sparsity of targets.

The theory of compressive sensing (CS) enables the reconstruction of sparse signals from a small set of non-adaptive linear measurements by solving a convex ℓ_1

minimization problem. In this chapter we present a data acquisition and imaging algorithm for Ground Penetrating Radars (GPR) based on CS by exploiting sparseness in the target space, i.e., a small number of point-like targets. First we give a brief summary of CS theory that will form the basics of the imaging and feature detection algorithms in this chapter, as well as Chapters 6 and 7. Then we present the impulse and stepped-frequency versions of the compressive subsurface imaging.

2.1 Compressive Sensing

Conventional sampling for 2D imaging problems acquires vast amounts of data which requires high acquisition rate and needs to be compressed for compact storage, rapid transmission or easier processing. Signals can be compressed if they can be approximated using a linear combination of a small set of some transform basis vectors (wavelets, DCT, Fourier, etc.). In conventional compression algorithms signals are sampled above the Nyquist rate, their transforms are computed and the large coefficients with their locations are retained to represent the signal. Even though only a small set of transform coefficients are used, the whole signal is sampled and its transform is computed. This is a potential time and energy waste. Compressive Sensing (CS) answers the question of whether we can measure the most informative part of the signal directly. CS takes non-traditional samples using randomized projections and shows that a signal having a sparse representation in some basis can be reconstructed from a small set of non-adaptive linear measurements.

Let's consider a signal x of length N. The signal x is called K-sparse if it can be written as

$$x = \sum_{i=1}^{K} w_i \psi_i, \tag{14}$$

where the w_i are weighting coefficients and ψ_i the basis vectors. We can write the

sparse signal x in matrix notation

$$x = \Psi \boldsymbol{w}. \tag{15}$$

where Ψ is the sparsity basis whose columns are filled by ψ_i and $\boldsymbol{w}$ is the weighting vector.

In compressive sensing, rather than sampling a signal at its Shannon-Nyquist rate, linear projections $y(m) =< x, \phi_m^T >$ of the signal onto a second set of basis vectors, $\phi_m, \quad m = 1, 2, ...M$, are measured. Here fewer measurements, $M < N$, are used compared to the dimension of the signal x. In matrix notation we measure

$$y = \Phi x. \tag{16}$$

In the case of $M < N$, the recovery of x from the measurements y is ill-posed. However, compressive sampling theory tells us that if the matrix $\Phi\Psi$ has the Restricted Isometry Property (RIP) [16, 5] then it is possible to recover x exactly from $O(K \log(N))$ measurements by solving the following ℓ_1 minimization problem [15, 31]

$$\min ||\hat{x}||_1 \quad s.t. \quad y = \Phi\Psi\hat{x}. \tag{17}$$

The optimization problem in (17) can be solved via linear programming techniques.

The basic issue is to design a stable measurement matrix Φ such that the information in any K-sparse signal is not corrupted by the dimensionality reduction of Φ from N to M dimensions. Let $A = \Phi\Psi$ and A_T, $T \subset \{1, ..., N\}$ be the $M \times |T|$ sub-matrix obtained by extracting the columns of A corresponding to the indices T. The K-restricted isometry constant δ_K of A is the smallest quantity such that

$$1 - \delta_K \leq \frac{\|Av\|_2}{\|v\|_2} \leq 1 + \delta_K \tag{18}$$

for all subsets T with $|T| \leq K$ and coefficient sequences v_j where $j \in T$ [17]. This property essentially requires that every set of columns with cardinality less than K

approximately behaves like an orthonormal system. In [16] it is proved that when x is K-sparse and $\delta_{2K} + \delta_{3K} < 1$, then the solution of (17) is exactly equal to x.

A surprising but powerful choice for the measurement matrix Φ is a random matrix. For example, sampling N vectors on the unit sphere of $\mathcal{R}^M$ independently and uniformly at random. The property in (18) will hold for $K = O(M/\log(N/M))$ with probability $1-O(\exp^{-\gamma N})$ for some $\gamma > 0$ [17]. It has been shown that a random measurement matrix Φ whose entries are i.i.d. Bernoulli or Gaussian random variables will satisfy the RIP with any fixed basis Ψ like spikes, sinusoids, wavelets, Gabor functions, curvelets, etc. [5]

The theory of CS is not limited just to the recovery of sparse signals. In general, signals can be compressible, which means the sorted magnitudes of the transform coefficients decay rapidly to zero. Compressible signals can be well approximated as sparse. For an arbitrary signal $x \in \mathcal{R}^N$ let x_K be its best K-sparse approximation. It is shown in [12] that if the RIP holds, the recovery error is not much worse than $\|x - x_K\|_{\ell_1}$. Moreover, the recovery procedure is robust with respect to measurement errors. Adding a perturbation ϵ_n to the measurements will not induce a recovery error of more than a small constant times ϵ_n [13]. For the case of noisy measurements, new reconstruction programs that relax the data fidelity term are available [34, 55, 12, 14]. One form comes from constraining the energy of the reconstruction error as

$$\min \|x\|_1 \qquad s.t. \quad \|y - Ax\|_2 < \epsilon. \tag{19}$$

For the program in (19) it is shown in [12] that the reconstruction error is finite and the reconstruction is stable. This is a second-order cone program (SOCP). A much easier linear program for noisy reconstruction is the so-called Dantzig selector [14], which requires that each element of the residual vector be within the noise level and that the residual vector not correlate well with the columns of A. It is formulated as

$$\min \|x\|_1 \qquad \text{s.t.} \quad \|A^T(y - Ax)\|_\infty < \epsilon. \tag{20}$$

The CS theory has found a variety of very interesting applications including image reconstruction[36], medical imaging [72], radar imaging [6], source localization [19, 46], and coding[18]. This chapter explains the application of CS theory to subsurface imaging using GPR measurements.

2.2 Compressive Subsurface Imaging Using Impulse GPRs

As the impulse GPR antenna scans a region, the radar transmits and receives a series of pulses. Although the response of targets can be quite complex, we assume that the received signal reflected from a point target at p is a time delayed and scaled version of the transmitted signal $s(t)$, i.e.,

$$\zeta_i(t) = As(t - \tau_i(p)) \tag{21}$$

where $\tau_i(p)$ is the total round-trip delay between the transmitter and the target at position p for the ith aperture point, and A is a scaling factor used to account for any attenuation and spreading losses. Calculation of $\tau_i(p)$ and its use in existing imaging methods are explained in Chapter 1. We approach the subsurface imaging as a dictionary selection problem where we can compute the image within a regularization framework and take into account any possible prior information.

2.2.1 Creating a dictionary for GPR data

A discrete inverse operator can be created by discretizing the spatial domain target space and synthesizing the GPR model data for each discrete spatial position. The target space $\boldsymbol{\pi}_T$ is a subset of the product space $[x_i, x_f] \times [y_i, y_f] \times [z_i, z_f]$, which must be discretized to generate the target space dictionary. Here (x_i, y_i, z_i) and (x_f, y_f, z_f) denote the initial and final positions of the target space to be imaged along each axis. Discretization generates a finite set of target points $\mathcal{B} = \{\boldsymbol{\pi}_1, \boldsymbol{\pi}_2, \ldots, \boldsymbol{\pi}_N\}$, where N determines the resolution and each $\boldsymbol{\pi}_j$ is a 3D vector $[x_j; y_j; z_j]$. Finally, we define the vector $\boldsymbol{b}$ to be a weighted indicator function of the targets, i.e., a nonzero positive

value at index j if $\boldsymbol{b}$ selects a target at $\boldsymbol{\pi}_j$.

Using (21) and (2) the signal at the GPR receiver can be calculated for a given element of $\mathcal{B}$. For the ith aperture point, received data can be written as

$$\boldsymbol{\zeta}_i = \left[\zeta_i\left(t_0\right),\ \zeta_i\left(t_0 + \frac{1}{F_s}\right), \ldots,\ \zeta_i\left(t_0 + \frac{N_t - 1}{F_s}\right)\right]^T, \tag{22}$$

where F_s is the sampling frequency, t_0 is an appropriate initial time, and N_t is the number of temporal samples. This allows us to write a linear relation between the target space indicator $\boldsymbol{b}$ and the model data at aperture i as

$$\boldsymbol{\zeta}_i = \boldsymbol{\Psi}_i \boldsymbol{b} \tag{23}$$

where $\boldsymbol{\Psi}_i$ is of size $N_t \times N$.

The matrix $\boldsymbol{\Psi}_i$ is the dictionary (or, sparsity basis) corresponding to all possible target points $\mathcal{B}$, when the GPR is at the ith aperture point. The jth column of $\boldsymbol{\Psi}_i$ in (23) corresponds to $(\boldsymbol{\pi}_j)$ being selected in $\boldsymbol{b}$, and can be written as

$$[\boldsymbol{\Psi}_i]_j = \frac{s(t - \tau_i(\boldsymbol{\pi}_j))}{\|s(t - \tau_i(\boldsymbol{\pi}_j))\|_2}. \tag{24}$$

Thus each column has unit norm and is independent of A in (21); only the time delay is needed. The dictionary formation is illustrated in Fig. 9.

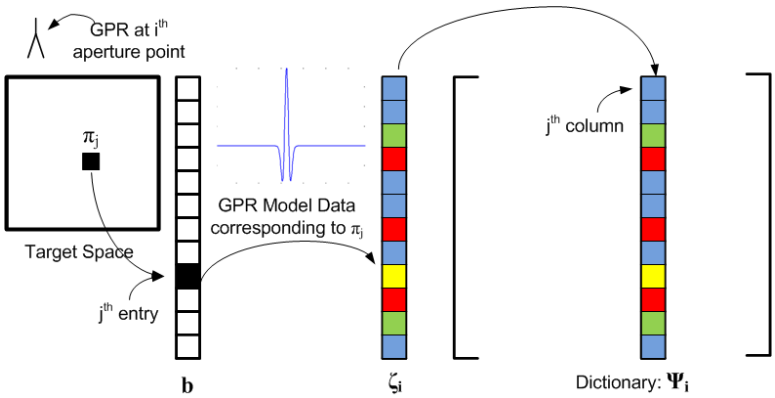

Figure 9: Creating the GPR data dictionary. The antenna is at the ith aperture point. Vectors next to the target space and the GPR model data represent the vectorized forms of the target space and the model data, respectively.

2.2.2 Compressive Sensing Data Acquisition

Standard GPR receivers sample the received signal (22) at a very high rate F_s. Here we present a new data acquisition model based on compressive sensing (CS) which would require many fewer samples to construct the target space image when the target space is sparse. In the spirit of CS a very small number of "random" measurements carry enough information to completely represent the signal. We define a measurement as a linear projection of the signal onto another vector. In the general case, measurements of a signal $\boldsymbol{x}$ can be written as $\boldsymbol{y} = \boldsymbol{M}\boldsymbol{x}$ where $\boldsymbol{M}$ is the measurement matrix. When $\boldsymbol{M}$ is the identity matrix, standard time samples of the signal are obtained. Figure 10 illustrates the standard and compressive sensing data acquisition models. In compressive sensing (CS), we measure linear projections of $\boldsymbol{\zeta}_i$

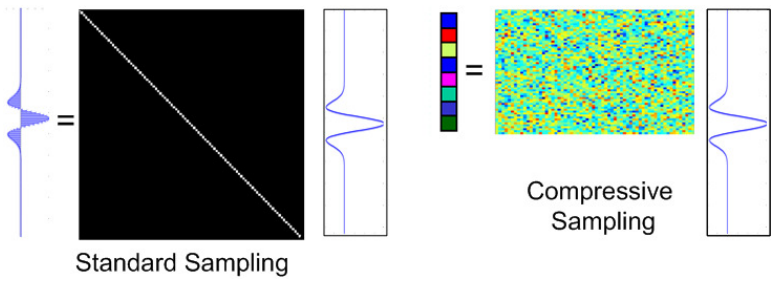

Figure 10: Standard time samples vs. compressive samples of the a signal.

onto a second set of basis vectors $\boldsymbol{\phi}_{im}$, $m = 1, 2, ...M$ which can be written in matrix form for the ith aperture point as

$$\beta_i = \boldsymbol{\Phi}_i \boldsymbol{\zeta}_i = \boldsymbol{\Phi}_i \boldsymbol{\Psi}_i \boldsymbol{b}. \tag{25}$$

where $\boldsymbol{\Phi}_i$ is an $M \times N_t$ measurement matrix and $M \ll N_t$.

We will study several types of measurement matrices. Entries of the Type I random matrix are drawn from $\mathcal{N}(0, 1)$. Type II random matrices have random ± 1 entries with probability of $\frac{1}{2}$, and a Type III random matrix is constructed by randomly selecting some rows of an identity matrix of size N which amounts to measuring

random space-time domain points. Selecting different types of measurement matrices impacts the imaging performance, but it will also result in different hardware implementations. For example, the system described in Fig. 11 could be used to implement the Type I and II measurement matrices. Microwave mixers can be used for the multipliers and low-pass filters can be used for the integrators. The system requires real-time generation of the signals $\boldsymbol{\phi}_{im}$, $m = 1, 2, ...M$. The switching rate of the signals will be near the Nyquist rate. A GPR intended to find small shallow targets like anti-personnel landmines would have a maximum frequency in the 2 to 6 GHz range, while a GPR intended to find larger and deeper targets such as tunnels would have a much lower maximum frequency in the 10 to 100 MHz range. It is difficult with current technology to generate the signals for the Type I measurement matrix at these rates, but it is relatively straight forward to generate the signals for the Type II measurement matrix; particularly if pseudo-random binary sequences are used since they can be generated by a state machine at the required rates. In fact, a more traditional GPR that uses pseudo-random binary sequences has been built [79].

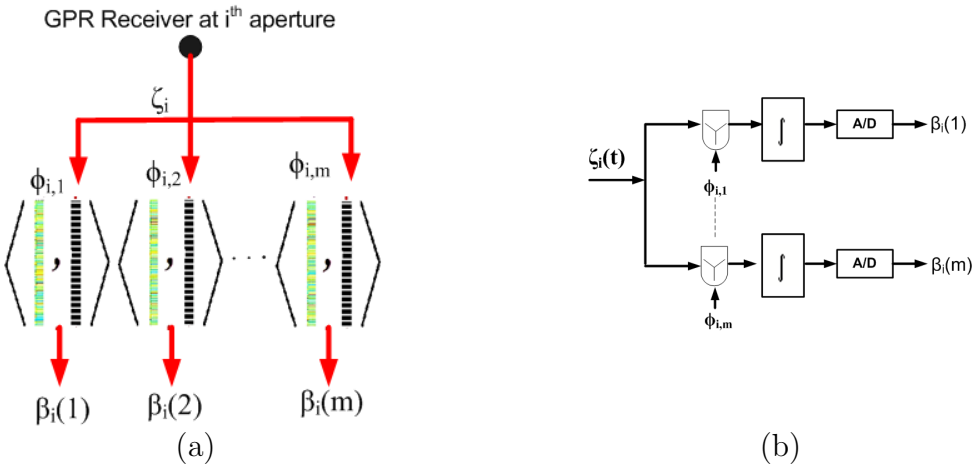

Figure 11: (a) Data Acquisition for GPR at one single aperture point, (b) One possible compressive sensing implementation at the GPR receiver.

A sensor based on the Type III measurement matrix would be very easy to implement since it would only require relatively minor changes to the sequential-sampling

systems used in most commercial GPRs [26, 63]. If the sampling system were changed from sequential to random, the system would directly measure the compressive measurements β_i. Random sampling is well understood and has some timing advantages over sequential sampling[39, 63]. Depending on the structure of $\mathbf{\Phi}_i$, other analog implementations could also be used [6, 90]. The effects of using different types of $\mathbf{\Phi}_i$ is analyzed in Section 2.2.8.

2.2.3 GPR Imaging with Compressive Sensing

For imaging, we use L aperture points and form a "super problem" with the matrices $\mathbf{\Psi} = [\mathbf{\Psi}_1^T, \ldots, \mathbf{\Psi}_L^T]^T$, and $\mathbf{\Phi} = \text{diag}\{\mathbf{\Phi}_1, \ldots, \mathbf{\Phi}_L\}$, and the selection vector $\boldsymbol{\beta} = [\boldsymbol{\beta}_1^T, \ldots, \boldsymbol{\beta}_L^T]^T$. The result of the CS theory is that the target space indicator vector $\boldsymbol{b}$ can be recovered exactly from $M = C\left(\mu^2(\mathbf{\Phi}, \mathbf{\Psi}) \log N\right) K$ measurements $\boldsymbol{\beta}$ with overwhelming probability [15], by solving an ℓ_1 minimization problem

$$\hat{\boldsymbol{b}} = \text{argmin}\, \|\boldsymbol{b}\|_1 \qquad s.t. \quad \boldsymbol{\beta} = \mathbf{\Phi}\mathbf{\Psi}\boldsymbol{b}. \tag{26}$$

The quantity $\mu(\mathbf{\Phi}, \mathbf{\Psi})$ is the coherence between $\mathbf{\Phi}$ and $\mathbf{\Psi}$ defined as in [15].

The optimization problem in (26) is valid for the noiseless case because it uses an equality constraint. If the GPR signal is noisy, i.e., $\zeta_i^N(t) = \zeta_i + n_i(t)$, then the compressive measurements $\boldsymbol{\beta}_i$ at the ith aperture position have the following form:

$$\boldsymbol{\beta}_i = \mathbf{\Phi}_i \boldsymbol{\zeta}_i = \mathbf{\Phi}_i \mathbf{\Psi}_i \boldsymbol{b} + \boldsymbol{u}_i \tag{27}$$

where $\boldsymbol{u}_i = \mathbf{\Phi}_i \boldsymbol{n}_i \sim \mathcal{N}(0, \sigma^2)$ and $\boldsymbol{n}_i$ is the concatenation of the noise samples at aperture point i which is assumed to be $\mathcal{N}(0, \sigma_n^2)$. Since $\mathbf{\Phi}_i$ is deterministic, we have $\sigma^2 = (\sum_{n=1}^{N_t} \boldsymbol{\phi}_{imn}^2)\sigma_n^2$. Hence, if we constrain the norm of the $\boldsymbol{\phi}_{im}$ vectors to be one, then $\sigma^2 = \sigma_n^2$.

It is shown in [12, 14, 55, 34] that stable recovery of the sparsity pattern vector $\boldsymbol{b}$ is possible by solving a modified convex optimization problem,

$$\hat{\boldsymbol{b}} = \arg\min \|\boldsymbol{b}\|_1 \qquad \text{s.t.} \quad \|\boldsymbol{A}^T(\boldsymbol{\beta} - \boldsymbol{A}\boldsymbol{b})\|_\infty < \epsilon_1 \tag{28}$$

where $\boldsymbol{A} = \boldsymbol{\Phi\Psi}$. Another possible solution comes from constraining the ℓ_2-norm of the error in the measurements to be less than some ϵ.

$$\min \|\boldsymbol{b}\|_1 \qquad s.t. \quad \|\boldsymbol{\beta} - \boldsymbol{A}\boldsymbol{b}\|_2 < \epsilon_2 \tag{29}$$

Although the target space images can be created using (28) or (29), the ℓ_1 minimization in (28) is a linear program and easier to implement while (29) is a second-order cone program (SOCP) [9]. The optimization problems in (26), (28) and (29) all minimize convex functionals, so a global optimum is guaranteed.

For the numerical solution of (28) or (29) a convex optimization package called ℓ_1-magic [78] is used. The convex optimization programs use interior point methods that depend on iterations of Newton's method. For optimizing (28) or (29), the cost[1] is $O(N^3)$ with the observation that the number of iterations typically stays quite low, almost independent of the size of the problem [71, 9]. A theoretical worst case bound on the number of iterations is given as $O(\sqrt{N})$ [71]. The computational complexity is higher than that of backprojection which has a complexity of $O(NL)$ where L is the total aperture number. However, the benefit is generality, sparser images as well as a low number of measurements in both time and spatial domains.

2.2.4 Selection of Algorithm Parameters

An important part of the proposed subsurface imaging system is the selection of two algorithm parameters: the spatial grid density, N, and the regularization parameter, ϵ in (28) or (29), which controls the tradeoff between the sparsity of the solution and how well the solution fits the data.

Since discrete spatial positions are used to create the sparsity dictionary, the estimates of the target locations are confined to the selected grid. Increasing N makes the grid uniformly very fine, but it also increases the complexity of the algorithm. Our method is suitable for multiresolution grid refinement. Initially a coarse grid might

[1] We assume $ML \leq N$

be used to obtain an approximate knowledge of possible target locations. Later the grid can be made finer around regions of interest where better precision is required. Making the initial grid too coarse might introduce substantial bias in the estimates. Our results indicate that using a $0.5 - 1\,\text{cm}$ depth resolution usually suffices.

Selecting a proper regularization parameter ϵ is also very important. If ϵ is not set properly, then (28) either will not fully reconstruct the sparsity pattern vector and will lose some targets (underfitting), or it tries to explain a significant portion of the noise by introducing spurious peaks. When the noise statistics of the data are known, a "good" choice of ϵ can be made, e.g., for additive white Gaussian noise (WGN) with variance σ^2 selecting $\epsilon = \sqrt{2 \log N}\sigma$ makes the true $\boldsymbol{b}$ feasible with high probability [14].

In most cases the noise statistics are unknown and need to be estimated. We use an automatic method for selecting the regularization parameter ϵ based on cross-validation (CV) [8] that doesn't require any knowledge or estimate of the noise statistics. The method depends on separating the measurements into estimation and CV sets. The compressive imaging method is applied to the estimation data set with an initial selection of ϵ and then the method's result is tested on the CV data set. As the algorithm iterates the prediction performance in the CV set increases with decreasing ϵ. When the method starts to overfit the estimation data set which means estimating part of the noise, performance in the CV set decreases. Further decrease in ϵ is not beneficial and the algorithm should be terminated.

The CV based algorithm consists of the following steps:

(i) Initialization: Set $\epsilon = \alpha \|\boldsymbol{A}_E^T \boldsymbol{\beta}_E\|_\infty$, $\hat{\boldsymbol{b}} = 0$ and $i = 1$. An initial ϵ that allows the method not to overfit the data can be selected by setting $\alpha = 0.99$. Note that for $\alpha > 1$, automatically $\hat{\boldsymbol{b}} = 0$ is the minimum ℓ_1 norm solution.

(ii) Estimation: Apply (28) to get an estimate of target locations $\hat{\boldsymbol{b}}^{(i)}$ using $\boldsymbol{A}_E$.

(iii) Cross-Validation: if $\|\boldsymbol{A}_{CV}^T(\boldsymbol{\beta}_{CV} - \boldsymbol{A}_{CV}\hat{\boldsymbol{b}}^{(i)})\|_\infty < \epsilon$ then set $\epsilon = \|\boldsymbol{A}_{CV}^T(\boldsymbol{\beta}_{CV} -$

$\boldsymbol{A}_{CV}\hat{\boldsymbol{b}}^{(i)})\|_\infty$, else terminate the algorithm.

(iv) Iteration: Increase i by 1 and iterate from Step (ii).

2.2.5 Discussion

The theory of compressive subsurface imaging outlined in Section 2.2 is based on two important assumptions; namely, that the speed of propagation in the medium is known and that potential targets are positioned at discrete spatial points. However, in most subsurface imaging problems these assumptions are not always valid. The propagation velocity may only be known approximately, and targets will generally not fall on the grid. These problems also affect current subsurface imaging algorithms. The presented algorithm can handle these kinds of non-ideal situations.

When the true velocity of the medium is not known, it is not possible to locate the target at its true location. The CS method can generate focused target space images when the propagation velocity is unknown. To test the CS method's performance a simulated GPR data set from a single point target at $(x, z) = (0, -8)$ cm is generated using a true propagation velocity of $v = 2 \times 10^{10}$ cm/s. The test data is used to image the target space with assumed velocities varying from 1×10^{10} cm/s to 3×10^{10} cm/s. For each assumed velocity 100 independent images are computed with different noise realizations (SNR = 10 dB) and with different random measurement matrices at each time.

It can be observed in Fig. 12 that although the estimated depth of the target is changing as the velocity changes, the CS method could still generate focused images. The average distance of the estimated target point from the true target position is shown in Fig. 13 as a function of the assumed velocity. When the assumed velocity is the same as the true velocity for the medium the target is imaged as a single point at its correct position as shown in Fig. 12(c). The distance of the estimated target position from the correct target position increases as the assumed velocity is

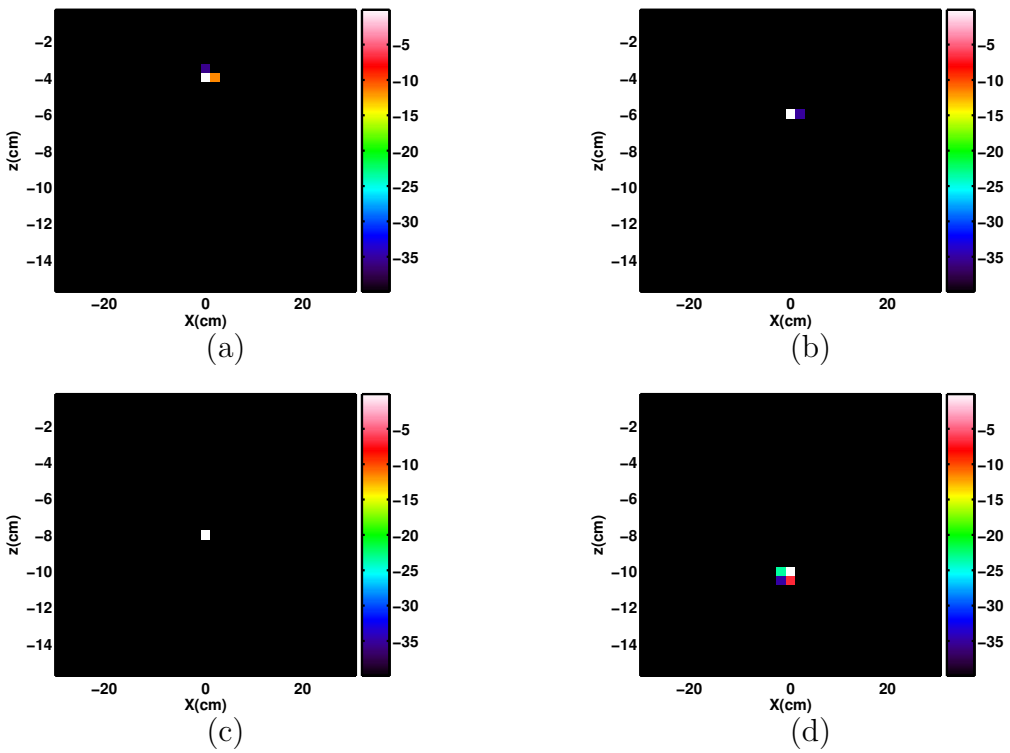

Figure 12: Average of the 100 independent imaging assuming the propagation velocity is (a) 1×10^{10} cm/s, (b) 1.5×10^{10} cm/s, (c) 2×10^{10} cm/s, (d) 2.5×10^{10} cm/s.

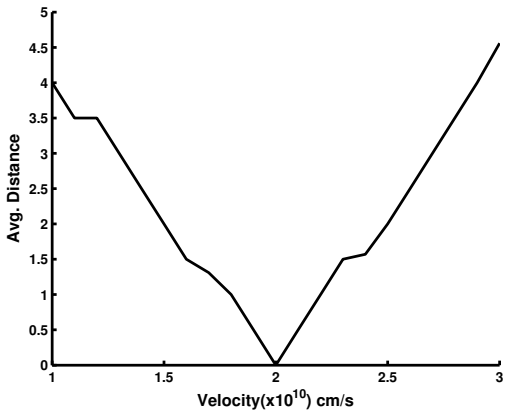

Figure 13: Distance of the estimated target point from the true target location as a function of the assumed velocity.

further from the true velocity of the medium. It is important to note that the CS method locates the x axis of the target correctly while the unknown velocity affects the depth estimate only. The reason for the depth shift is that the optimization in

(28) matches the measured data "best" with the given constraint using a dictionary element corresponding to a target at another depth. Figure 14(a) shows the model GPR data from a target at $(x, z) = (0, -8)$ using $v = 2 \times 10^{10}$ cm/s, while Fig. 14(b) shows the model GPR data from a target at $(x, z) = (0, -4)$ using $v = 1 \times 10^{10}$ cm/s. The similarity of these dictionary elements in two different dictionaries explains the results in Fig.12

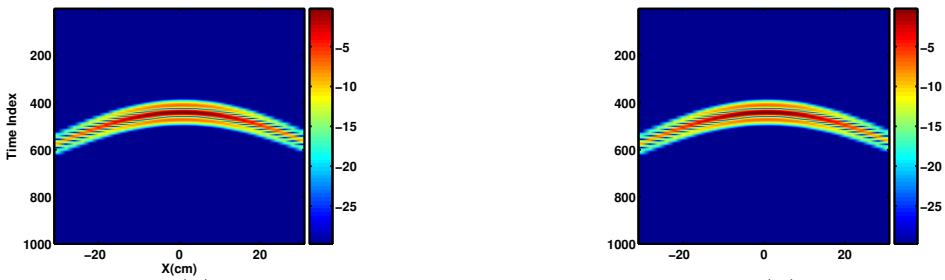

(a) (b)

Figure 14: Model GPR data (a) for a target at $(x, z) = (0, -8)$ using $v = 2 \times 10^{10}$ cm/s and (b) for a target at $(x, z) = (0, -4)$ using $v = 1 \times 10^{10}$ cm/s.

To determine the amount of depth shift consider a single homogeneous medium where targets and antenna are both in the same medium. The total time delay for two points targets p_1 and p_2 shown in Fig. 15 are $\tau_1 = \frac{2\sqrt{(x_A-x_1)^2+(z_A-z_1)^2}}{v_1}$ and $\tau_2 = \frac{2\sqrt{(x_A-x_2)^2+(z_A-z_2)^2}}{v_2}$, respectively. It can be noted that if $x_1 = x_2$ then it is possible to

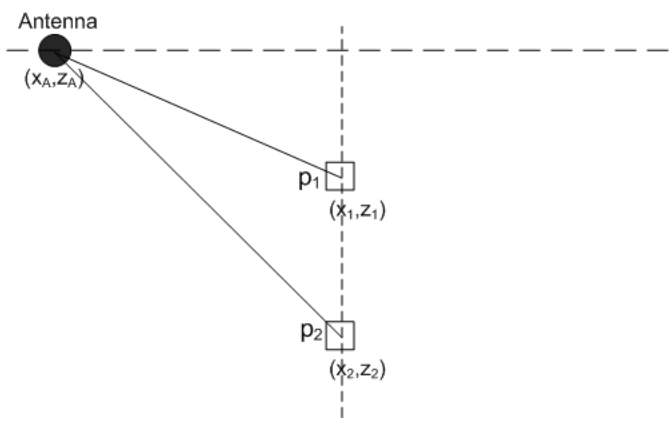

Figure 15: Two point targets in a homogeneous medium.

get $\tau_1 = \tau_2$ for all antenna positions (throughout the full scan) if $|z_A - z_2| = \frac{v_2}{v_1}|z_A - z_1|$.

This means that if the target space was homogeneous, applying our method with an unknown velocity v_2 that is different from the true velocity v_1 will result a target space image with only p_2 instead of the correct target position p_1, since the measured data can be exactly matched using the element of the data dictionary corresponding to p_2. Since the results in Fig. 12 are from a 2-layer medium (air and soil), we don't observe this exact representation ; but similarly we observe focused images with sparsely selected target points.

The effect of the unknown velocity mismatch on the created images is also analyzed. Three different double differentiated Gaussian pulses with center frequencies of 1.5 GHz, 4.5 GHz, and 7.5 GHz are tested. Note that the pulse with center frequency 1.5 GHz is the widest pulse. Then normalized variability of the generated images as a function of the assumed velocity is shown in Fig. 16. It is observed interestingly

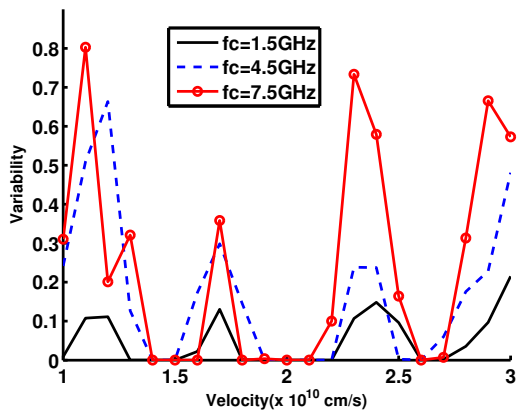

Figure 16: Normalized variability of the created images as a function of assumed velocity for three different transmitted pulses. The true velocity is taken as $v = 2 \times 10^{10}$ cm/s.

that variability doesn't increase monotonically as the velocity mismatch increases, but it has ups and downs. We believe this is because some dictionary elements at certain velocities have very close representations to the data for the true velocity. It is also observed that using shorter pulses (i.e., higher center frequency)increases the variability of the images.

The "target off the grid" problem can be addressed with the constraints in (28) and (29) since they allow nonidealities. The terms in the Dantzig Selector constraint (28), $\boldsymbol{A}^T\boldsymbol{\beta}$ and $\boldsymbol{A}^T\boldsymbol{A}$ are actually auto-correlations of the transmitted signal $s(t)$. For $\boldsymbol{A}^T\boldsymbol{\beta}$ we get a column vector whose n-th element is $R(\tau_i(\boldsymbol{\pi}_n), \tau(\boldsymbol{\pi}_T))$, where R is the autocorrelation of the signal $s(t)$ at two time delays corresponding to targets at $\boldsymbol{\pi}_n$ and $\boldsymbol{\pi}_T$. Here $\boldsymbol{\pi}_n$ is the nth discrete position and $\boldsymbol{\pi}_T$ is the true target position. For the matrix $\boldsymbol{A}^T\boldsymbol{A}$, the element in the n-th row and r-th column is $R(\tau_i(\boldsymbol{\pi}_n), \tau(\boldsymbol{\pi}_r))$. The autocorrelation of $s(t)$ affects the resolvability of two targets and the handling of nonidealities. If $s(t)$ doesn't decorrelate quickly two close targets might not be resolved while nonidealities would be handled easily since the correlation $\boldsymbol{A}^T\boldsymbol{\beta}$ will still be high even in the presence of velocity perturbations, or when the target is off the grid. In the other extreme case where the autocorrelation of $s(t)$ only peaks at zero lag, i.e. $s(t)$ is an impulse, resolvability of targets will increase while the ability to handle nonidealities will decrease. The tradeoff between the resolution and ability to handle nonideal conditions is actually an open waveform design problem.

The bottom line of this analysis is that the Dantzig Selector constraint, with a well-chosen ϵ and $s(t)$, will allow the matching of targets at their closest grid positions. Then the ℓ_1 minimization of the selector vector $\boldsymbol{b}$ will tend to pick the signals whose autocorrelation is large. Equation (28) does this selection to minimize the ℓ_1 norm of $\boldsymbol{b}$, giving a sparse solution satisfying the constraint.

2.2.6 A Simulated Imaging Example

A test example will illustrate the ideas presented in the previous section. A 2D slice of the target space of size 30 cm $\times$ 30 cm dimensions containing three randomly placed point targets is used. The true target space distribution is shown in Fig. 17(a). Targets are simulated as point targets and the space-time response is generated in MATLAB [52]. For this example a bistatic antenna pair with antenna height of 10 cm,

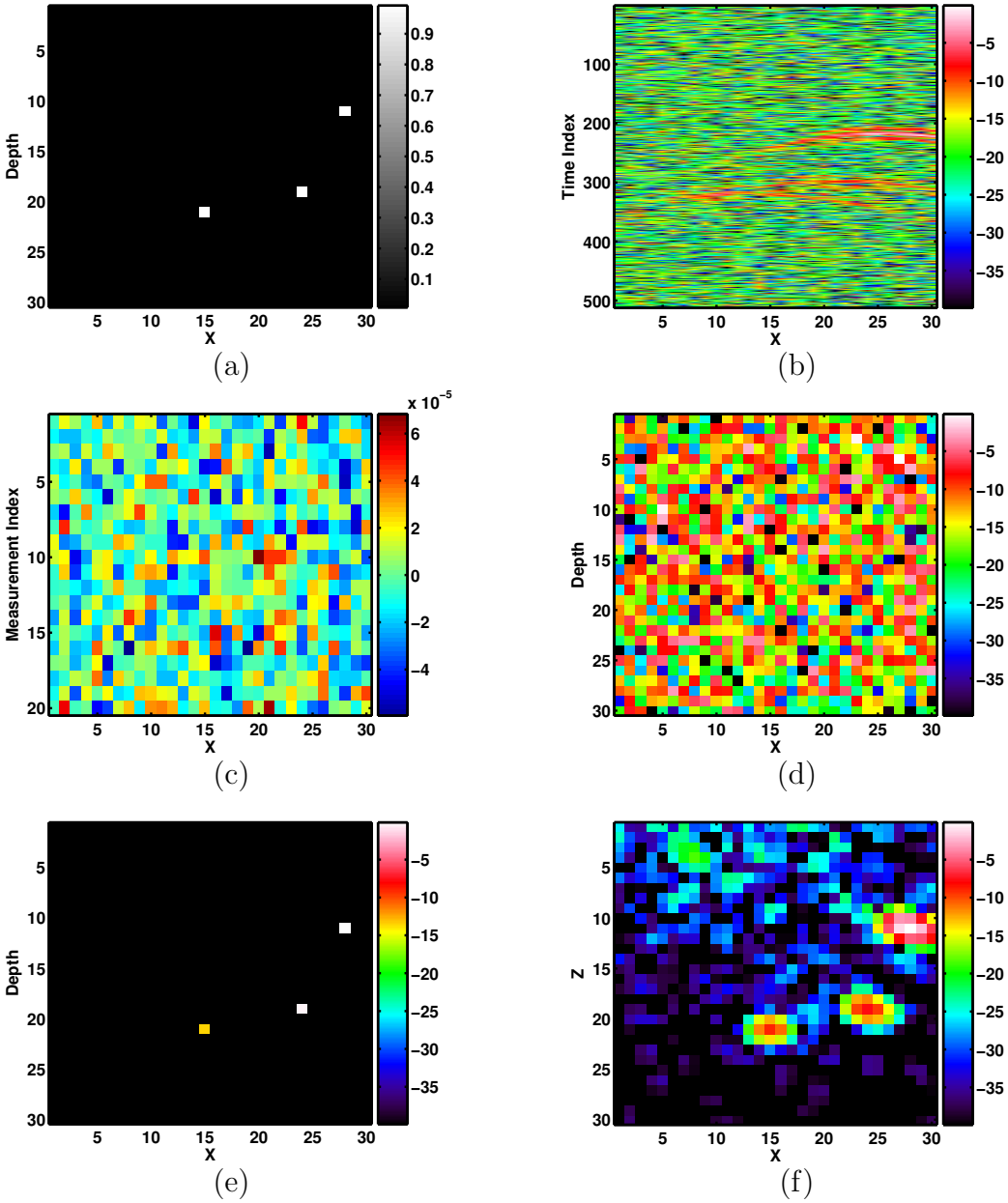

Figure 17: (a) Target space, (b) Space-time domain GPR response, (c) Compressive measurements at each aperture point, (d) The least-squares solution, (e) Solution obtained with the proposed method using (28), (f) Solution obtained with standard time-domain backprojection algorithm.

transmitter-receiver distance of 5 cm, and dry soil with permittivity $\varepsilon = 4$ is used.

The noisy space-time domain response of the target space is shown in Fig. 17(b). The signal-to-noise ratio (SNR) for this example is -5 dB. Instead of measuring the

space-time domain response at each aperture position, twenty inner product measurements are formed at each aperture point making 600 measurements in total for 30 aperture points. This is much less than the 512×30 raw space-time domain measurements (Fig. 17(c)). The inner products can be written as the product of the time-domain response with rows of a random matrix $\boldsymbol{\Phi}_i$ of size 20×512 whose entries are drawn independently from $\mathcal{N}(0, 1/\sqrt{512})$. These 600 measurements are the only information used to sense the target space area. The number of targets is not assumed to be known.

The sparsity pattern vector for the 30×30 target space has length 900 and we have 600 measurements which results in an underdetermined system of equations, $\boldsymbol{\beta} = \boldsymbol{A}\boldsymbol{b}$. One possible feasible result is the least squares solution, $\hat{\boldsymbol{b}} = \boldsymbol{A}^T(\boldsymbol{A}\boldsymbol{A}^T)^{-1}\boldsymbol{\beta}$. The target space image for this is shown in Fig. 17(d). Although the solution is feasible in the sense that it satisfies the compressive measurements, it gives no sensible information about possible target positions.

For target space imaging, the Dantzig selector (28) is used with cross validation to select a proper ϵ and a stopping condition. While 500 measurements are used for imaging in (28) 100 measurements are used for CV. Figure 17(e) is obtained as the target space image. The result from Fig. 17(d) is used as a feasible starting solution for convex optimization.

It can be seen that the actual target positions are found correctly, and the obtained image is much sparser compared to the standard backprojection (SBP) result in Fig. 17(f), even though the backprojection result is obtained using all of the space-time data. Both of the images in Fig. 17(e,f) are normalized to their own maxima and are shown on the same 40-dB scale. The convex optimization result has less clutter in the image since the problem forces a sparse solution through the ℓ_1 norm minimization.

As a further test, the target space image was formed 100 times by selecting an

independent random measurement matrix at each time and applying the proposed algorithm. It is observed that the algorithm introduces no bias to the target position estimates and any random measurement matrix works equally well satisfying the minimal measurement number.

2.2.7 Performance in Noise

To analyze performance versus noise level, the algorithm is applied to GPR data with SNRs from $-25\,\mathrm{dB}$ to $15\,\mathrm{dB}$. At each SNR level, the space-time domain GPR data of a single target is corrupted by zero-mean WGN with an appropriate variance. The Dantzig selector (28) is used to construct the target space image. This procedure is repeated 50 times with random initialization of the noise each time. For each SNR level the variance of the target locations is calculated and plotted in Fig. 18(a) for SBP and the proposed method with a varying number of measurements[2]. SBP requires all the space-time domain data which consists of 220 measurements for each aperture. It has lower variance values for low SNRs since it uses many more measurements, but for moderate and high SNRs the proposed method results in much lower variances. The variance of SBP is nearly flat for moderate to high SNRs where it reaches its resolution limit. Our method provides much lower variances indicating a super-resolution property, which has also been observed in similar sparse signal reconstruction applications [33, 73].

The normalized variance on the constructed images for the tested methods is plotted on Fig. 18(b). Smaller image variance is an indication of a correctly reconstructed and sparse image. The proposed method has lower variance than SBP for SNRs greater than $-20\,\mathrm{dB}$ and with increasing measurements variance decreases faster. The fact that the proposed method favors sparse solutions explains the smaller image variance.

[2]To obtain the plot in Fig. 18(a) we used a grid size of 0.01 cm to get estimates not limited to a coarse grid.

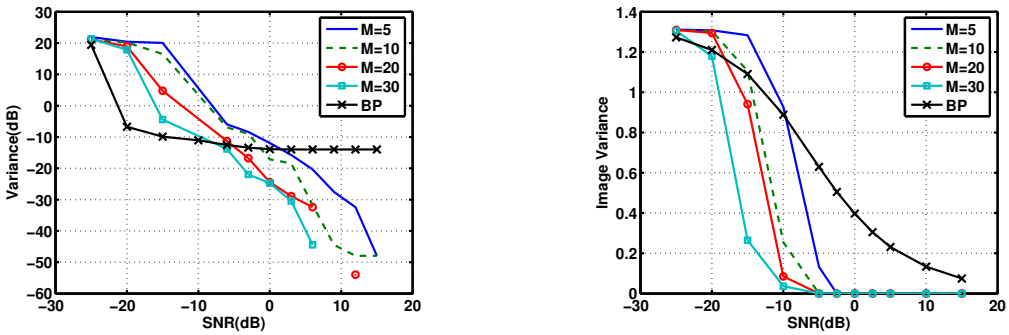

(a) (b)

Figure 18: (a) Variance on target positions vs. SNR. (b) Variance on the created images vs. SNR. Comparison with variance of SBP and the proposed method. M is the number of measurements at each aperture for the proposed algorithm. SBP measures the full space-time domain data which has 220 measurements for each aperture.

2.2.8 Effect of the Measurement Matrix $\mathbf{\Phi}$

The results shown in Fig. 17 use a measurement matrix whose entries are drawn from a normal distribution. Here the effects of using six different types of measurement matrices are analyzed. Type I-III are as defined in Section 2.2.2.

Types IV, V and VI are random matrices that lie between Types II and III. At each aperture a random subset of the data is selected and projected onto vectors having random ± 1 entries with probability of $\frac{1}{2}$. Type IV uses 50% of the data, type V 10%, and Type VI 2%. Each matrix is normalized to have unit norm columns.

An average mutual coherence $\mu(\mathbf{\Phi}, \mathbf{\Psi})$ is found for each type of measurement matrices $\mathbf{\Phi}$ and the GPR sparsity dictionary $\mathbf{\Psi}$ over 100 randomly selected measurement matrices. The mutual coherence values tabulated in Table 3 show that the required number of compressive measurements will be similar if Type I or II matrices are used, although Type II is slightly better than Type I. Using a Type III matrix will require approximately $(9.82/3.15)^2 \approx 9$ times more compressive measurements for the same imaging performance. Although Type III requires many more measurements, it has a simpler data acquisition implementation (See Section 2.2.2). Types IV–VI show the tradeoff between the required number of samples and the simplicity of the data

Table 3: Mutual Coherence for Different Types of Measurement Matrices

Type	I	II	III	IV	V	VI
μ	3.76	3.15	9.82	3.62	4.56	7.54

acquisition process.

A Monte-Carlo simulation is done to test the performance of the proposed method as a function of the number of compressive measurements for each random matrix type. Each random matrix is tested with noisy GPR data having 3 targets at $SNR =$ 10 dB. The Monte-Carlo simulation uses 100 trials and each trial uses a different random measurement matrix to generate the compressive measurements. Then the target space image is constructed using (28).

Figure 19 shows the variance from 100 trials versus the number of measurements for the six different measurement types defined above.

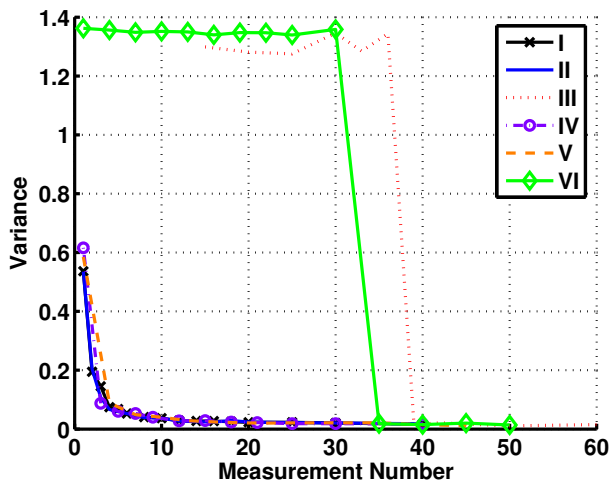

Figure 19: Variance vs. Measurement number for different types of random matrices. Legend indicates the measurement matrix type.

While Types I, II, IV and V require a similar number of measurements, Type III and VI random matrices require many more measurements to obtain a similar level of performance which is expected from the mutual coherence given in Table 3.

2.2.9 Random Spatial Sampling

The convex optimization problem in (28) solves for the target space using measurements from different aperture positions jointly. As long as the total number of measurements is greater than the minimum required for correct reconstruction, the number of spatial aperture positions can be reduced. Figure 20 shows the reconstruction results from randomly sampled spatial positions. In Fig. 17, 20 compressive measurements at 30 spatial positions were used. This example uses 15 randomly selected aperture points out of a total of 30 and at each aperture point also 20 compressive measurements are taken. The actual target space is the same as Fig. 17(a). The space-time domain response is shown in Fig. 20(a). The skipped aperture positions are shown with black stripes. The compressive measurements at the selected aperture positions are shown in Fig. 20(b). Convex optimization and standard backprojection results are shown in Figs. 20(c) and (d). The CS result is a slightly degraded compared to using the full aperture; however, the backprojection result is severely degraded compared to the full aperture result.

To test how much further the random spatial sampling can be reduced a Monte-Carlo simulation was performed. Noisy GPR data for three point targets are generated for 30 aperture points with SNR = 10 dB. The target space is constructed using the compressive measurements with a varying number of aperture points from 1 to 30. A subset of aperture points are randomly selected and the target space is reconstructed with (28) using only the measurements from the selected aperture points. This procedure is repeated 100 times with random aperture selections at each time. Two cases are tested. In Case 1 $M = 10$ measurements are taken at each used aperture which makes 300 total measurements when the full aperture is used. In Case 2 the number of total measurements is kept at 300, i.e., when 15 aperture points are used $M = 20$ in Case 2 while Case 1 still takes $M = 10$ measurements. Table 4 shows the variance for a varying number of aperture points comparing two cases of

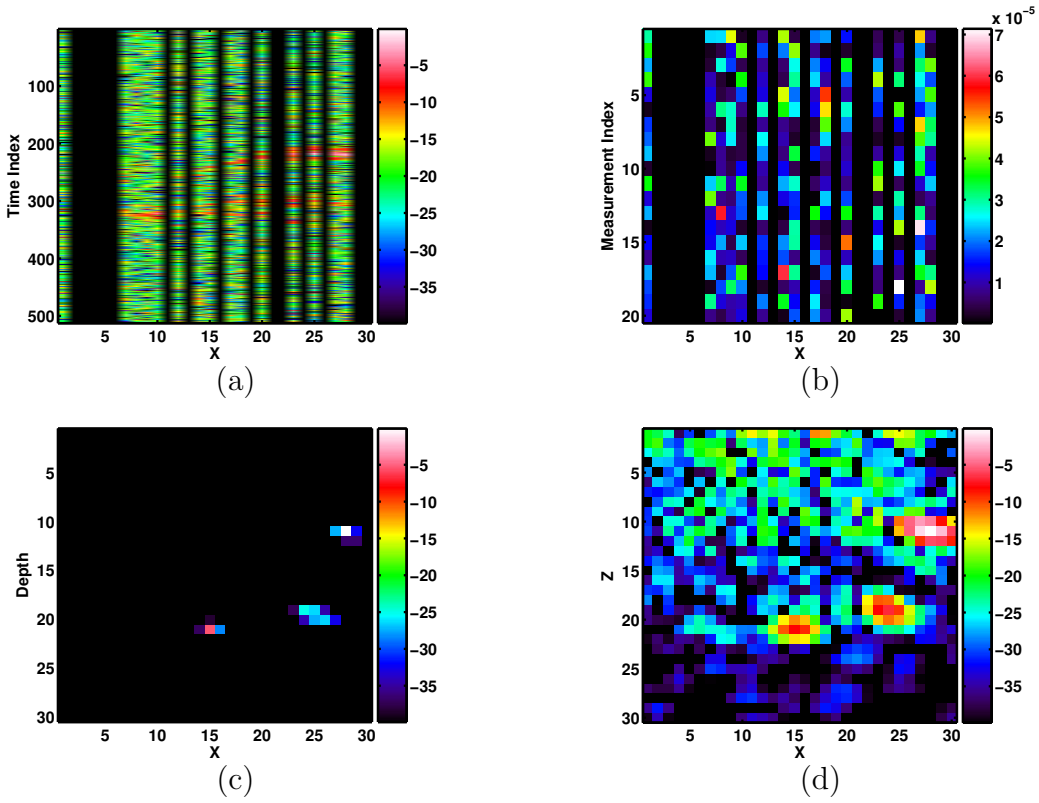

Figure 20: (a) Space-time domain response of the target space to the GPR data acquisition process at randomly sampled spatial aperture positions, (b) Compressive measurements at the sampled aperture positions, (c) Target space image obtained with the proposed method, (d) Target space image obtained with time domain back-projection.

Table 4: Image variance with varying number of spatial samples for time domain GPRs

Reduced Spatial Sampling Test						
No of Apertures	30	20	10	5	3	1
Case 1	0.07	0.14	0.40	0.91	1.07	1.26
Case 2	0.07	0.12	0.22	0.48	0.66	1.38
Backprojection	0.13	0.43	0.71	0.91	1.03	1.19

the proposed method with the backprojection.

Table 4 shows that the proposed method is less effected by the reduced number of spatial samples compared to backprojection. While decreasing the number of apertures from 30 to 20 increases the variance of the proposed method doubles from

0.07 to 0.14, the variance of backprojection results increase by more than 3 times from 0.13 to 0.43. Using one third of the spatial points is still enough for the proposed method to generate correct target space images. Further decrease in the number of spatial points increases the variance of the results substantially. In Case 2 where the number of compressive measurements taken at each used spatial point are higher than Case 1, similar performances can be obtained with lower number of aperture points. Here the tradeoff is between the number of aperture points used and the complexity of data acquisition process at each aperture point.

2.2.10 Experimental Results

The proposed algorithm is tested on the experimental GPR data collected from a model mine field at the Georgia Institute of Technology [24]. The GPR antenna has a multistatic configuration as shown in Fig .21(a) consists of a linear array of resistive-vee antennas. The resistive-vee is chosen because it can radiate short pulses and has a low radar cross section [66, 65]. There are two transmitters (T1, T2) and four (R1, R2, R3, and R4) receivers in the array; they combine to form eight bi-static separations ranging from 12 cm to 96 cm in 12 cm increments. A microwave absorber is strategically placed on the array to reduce coupling between antennas and reflections between the array and the ground. The array is scanned over a 1.8 m $\times$ 1.8 m region by an automated positioner in 2 cm increments. At each position, a vector network analyzer measures the 401-point frequency response of each pair over the frequency range from 60 MHz to 8.06 GHz. Microwave switches make it possible for one analyzer to obtain data from all eight pairs. A test PC controls this entire process. A diagram of the multistatic GPR is shown in Fig. 21(b).

Laboratory testing has been conducted in a wedge-shaped tank, filled with damped compacted sand, which was chosen as a soil substitute because it can be dug up, refilled and repacked to obtain the same soil conditions with fairly good repeatability.

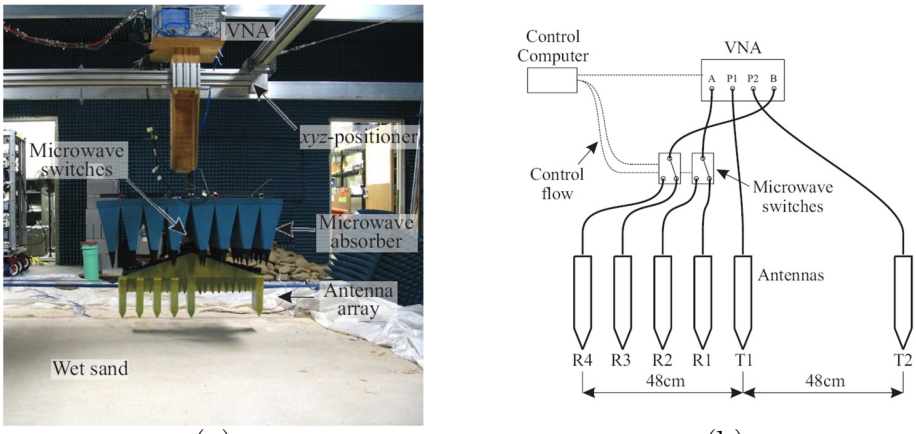

(a) (b)

Figure 21: (a) Phtograph of the experimental GPR system, (b) A diagram of the multistatic GPR system with the switching network.

Various targets like inert anti-tank and anti-personnel mines, or clutter like rocks, coke cans, sticks etc. can be buried at different depths in 1.8 m $\times$ 1.8 m scan region. Here we give results for two scenarios.

GPR Air Results: This section presents CS imaging of a 1″ diameter metal sphere held in the air at a height of 36.5 cm on a styrofoam support. The experimental setup is shown in Fig. 22(a). Since the GPR antenna and the target are in air, the wave speed is known to be $c = 3 \times 10^8$ m/s. The raw data measured by the T1-R1 pair over the target for a 2D slice is shown in Fig. 22(b). Since the CS measurement system is not yet built in hardware, standard space-time domain samples are obtained and the compressive measurements are created offline. Ten measurements are taken at each of the 70 aperture points for a total of 700 CS measurements. Random Type I measurement matrices are used. Two different case of $\mathbf{\Phi}_i$ are tested. Fig. 22(c) shows the actual compressive measurements when a different random $\mathbf{\Phi}_i$ is used at each aperture i, where Fig. 22(d) uses the same $\mathbf{\Phi}_i$ for all i. Using the same measurement matrix at each aperture will reduce the memory requirements and will be much easier to implement.

For CS target space reconstruction, the Dantzig Selector (28) is used with $\epsilon =$

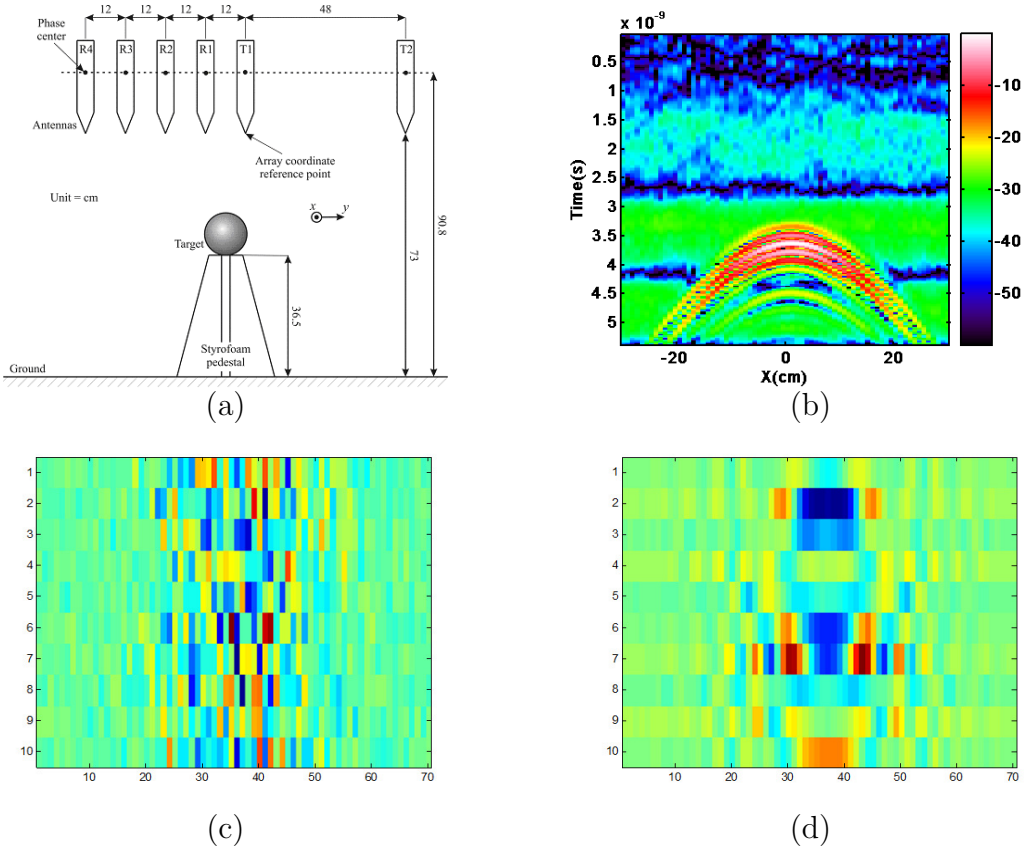

Figure 22: (a) Experimental setup for GPR Imaging,(b) Space-time domain measured GPR Response of a 1″ metal sphere in air. (c) Compressive measurements of the space-time domain data shown in (b) when different $\mathbf{\Phi}_i$ is used at each aperture i and (d) when same $\mathbf{\Phi}_i$ is used at each aperture i.

$0.5\|\boldsymbol{A}^T\boldsymbol{\beta}\|_\infty = 1.34 \times 10^{-4}$ for the measurement sets shown in Fig. 22. The result of the Dantzig Selector for Figs. 22 (c) and (d) are shown in Figs. 23(a) and (b), respectively. The target is 1″ sphere and its bottom is positioned at a height of 36.5 cm. While both measurement sets can construct a sparse representation of the target space successfully, it is seen that using different $\mathbf{\Phi}_i$ at each aperture has the potential of extracting more information about the target space for the same ϵ level. The results of the proposed algorithm are compared with the standard backprojection algorithm which uses the whole space-time domain data (Fig. 22(b)). Figure 23 shows that proposed method does a much better job at creating a less cluttered and sparser target space image than the backprojection result shown in Fig. 23(c). Note that

while backprojection uses a total of 15,400 standard time domain samples, CS uses only 700 compressive measurements. All images are shown on a 30-dB scale and are normalized to their own maxima.

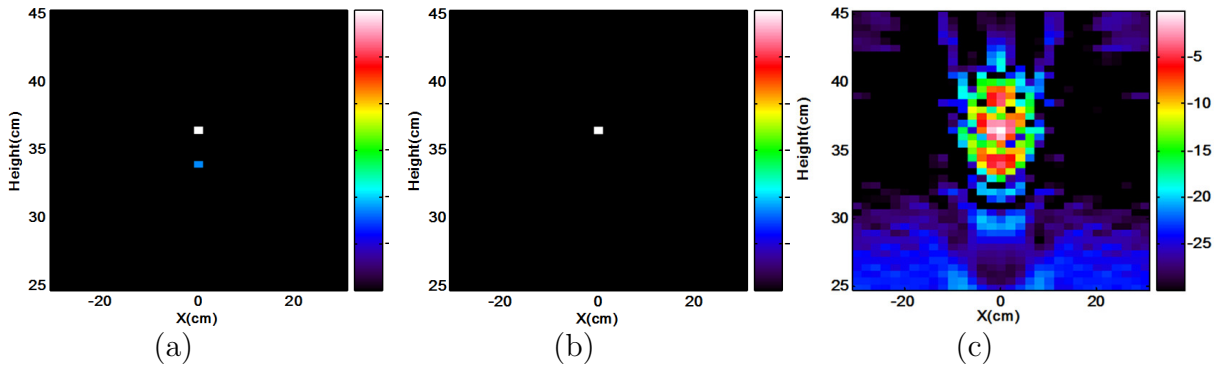

Figure 23: (a) Target space image found with CS imaging method using the measurement set in Fig. 22(c), (b) Target space image found using the measurement set in Fig. 22(d), and (c) Target space image found with standard time domain backprojection.

Buried Target Results: This part presents CS imaging of buried multiple targets such as antipersonnel and antitank mines, metal spheres, nylon cylinders and mine simulants. A picture of the buried targets is shown in Fig. 24(a) [49]. Figure 24(b) shows the burial locations, types and depths of the targets. The phase centers of the antennas are elevated 27.8 cm. The T1-R1 pair data which has a transmitter receiver distance of 12 cm is used. Figure 25 shows a line scan at $x = 0$ over four buried targets. The hyperbolic responses of the targets can be seen on the space-time domain data. Ground reflections are removed by time-gating. The speed of the wave in the soil is taken as $v = 3 \times 10^8$ m/s for both the proposed method and the SBP. When SBP is applied to the space-time domain data target space, the image shown in Fig. 25(b) is obtained. The image is normalized to its maximum and shown in a 30-dB scale. Although the 4 targets are clearly seen, the image is highly cluttered. Applying the proposed method using (28) with 15 compressive measurements at each aperture point results the target space image in Fig. 25(c). Type I measurement matrices

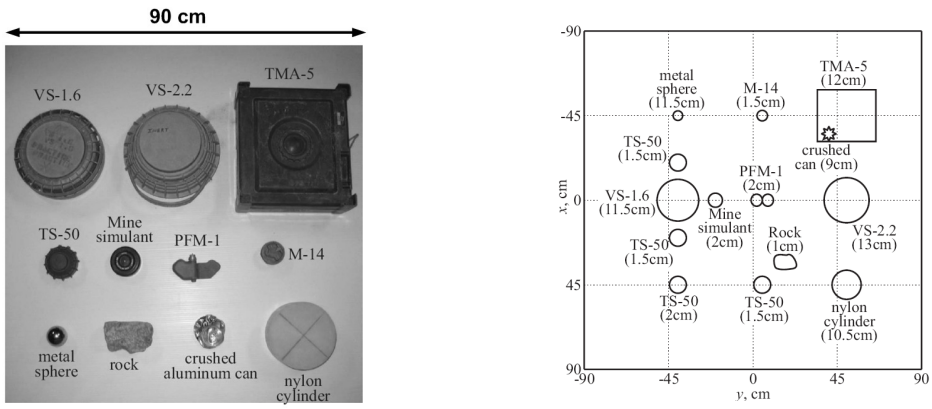

(a) (b)

Figure 24: (a) Picture of the buried targets, (b) Burial map of targets in sand. The numbers in parentheses are the buried depths of the targets.

were used to create the compressive measurements. Figure 25(c) is also normalized to its own maximum and shown in the same scale as the backprojection image. The proposed method can generate a much sparser and less cluttered target space image while finding the targets correctly. This shows that the proposed method has good performance even in the cases where the algorithm assumptions are not exactly valid, e.g., when the wave velocity is known approximately or the targets are not exactly point targets at discrete grid positions.

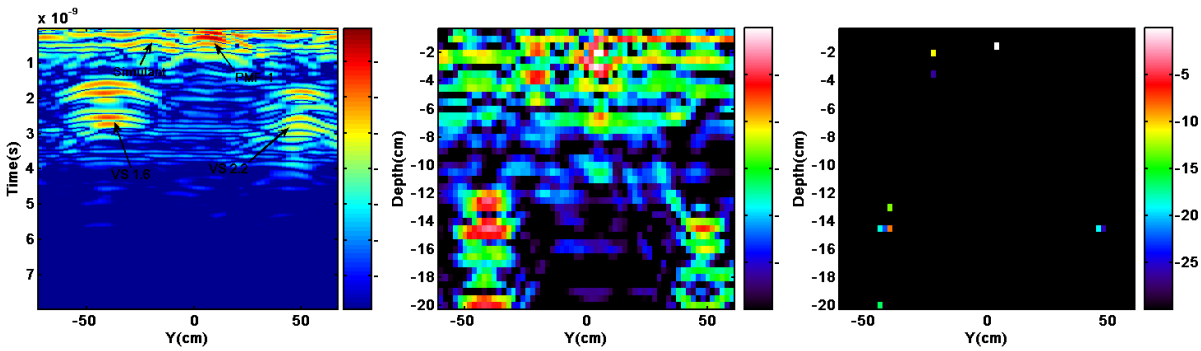

(a) (b) (c)

Figure 25: (a) Space-time domain GPR data for the $x = 0\,\text{cm}$ line scan of the burial scenario shown in Fig. 24. Image of the target space slice obtained by (b) backprojection and (c) compressive sensing.

Each line scan of the experimental data is imaged with both the proposed method and backprojection. The resultant images are put together to create a 3D image of the

subsurface. Figure 26 shows the topview of the scan area when the energy along the depth axis is summed to the surface created (a) with the backprojection and (b) with the compressive sensing. The proposed method uses 15 compressive measurements at each aperture point. Both results are shown on a 30-dB scale image. Actual target locations with corresponding sizes are also drawn on the images. It can be seen that both methods have similar imaging performance but the proposed method creates a much sparser image than the backprojection method. Although most of the targets are imaged correctly, the deep metal sphere and M-14 mine are missed in both methods.

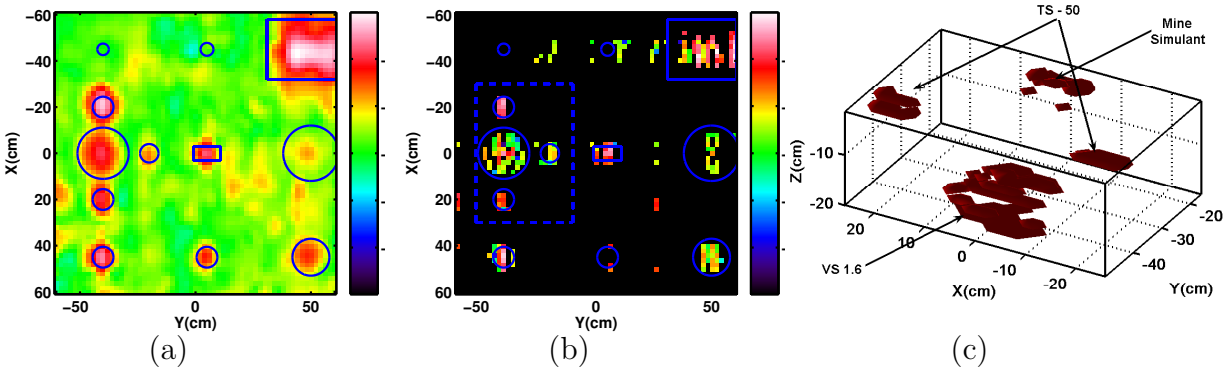

Figure 26: The surface energy image created by (a) Backprojection,(b) Compressive sensing. (c) 3D isosurface (-30dB) image of the selected region in (b) by dashed lines.

To show the spread of the targets in depth a 3D isosuface image is shown in Fig. 26(c). The isosurface image shows the selected region from Fig. 26(b) which includes two shallow TS-50 mines, one shallow mine simulant and one deep VS-1.6 mine. All targets are clearly seen at their corresponding depths.

2.3 Random Sampling for Stepped Frequency GPRs

Another type of GPR that is becoming increasingly popular is the stepped frequency continuous waveform (SFCW) GPR.[59, 75]. A stepped frequency signal probes the world at a discrete set of frequencies. A stepped frequency GPR has several advantages over an impulse GPR. The main advantage is the greater measurement

accuracy inherent in a frequency domain system. For example, since it is much easier to synthesize a pure tone at a given frequency than it is to measure a time delay, the accuracy with which the frequencies are set in the SFCW GPR is much greater than the measurement times used in an impulse GPR. This results in the SFCW GPR having much greater phase stability than an impulse GPR. The SFCW GPR also has a greater dynamic range and lower noise due to the higher mean power and narrow IF bandwidth of the SFCW system. The filtering used can greatly reduce the interference from nearby transmitters such as RF communication links. A SFCW GPR can also be programmed to skip over a defined frequency band so that it will not interfere with instruments on sensitive frequency bands. The operating frequency range can be adjusted to suit the specific ground conditions. For example, for the low frequency range can be used for relatively deep targets while higher frequencies are used for shallow objects [75].

Although SFCW GPRs have very good properties, they are not used as widely in commercial systems [57, 85, 10]. One important reason for this is its high data acquisition time. The time allowed at each aperture point and for each frequency before the GPR steps up the next frequency depends on several issues. These include the switching time for the sources, time to allow the transmitted signal to reach the receiver from a chosen maximum range, and time for the receiver to build up sufficient signal to noise ratio. For example in [85] it is reported that the built SFCW GPR can take measurements as a rate of 25/sec. The system uses the frequency band 1-3 GHz and takes 400 measurements at each aperture point. With this measurement rate, the system can be scanned at a speed of 1.8 kph with a 2 cm spatial increment which is too slow for some applications. For such applications, it is important to increase the speed of the system without degrading its performance.

The total subsurface frequency response formed from a combination of responses

from all reflectors within the medium can be inverted using various imaging algorithms. One type transforms the measured frequency data to time domain signals by applying the IFFT to each A-Scan measurement and then applying the time domain backprojection (SBP) method [37, 76] (See Ch.1.1.1) to create an image of the target space. Frequency domain imaging algorithms [42, 86, 80] directly uses the SFCW data to create the target space image. The current imaging algorithms basically perform a matched filtering operation with the impulse response of the data acquisition process to form the images.

This section a novel data acquisition and imaging algorithm for SFCW GPRs based on random selection of measured frequencies that significantly reduces the data acquisition time and creates less cluttered target space images compared to standard imaging methods [42, 86, 80]. In addition to random sampling in the frequency domain also the spatial aperture can be sampled randomly without degrading the created image significantly. Additional random spatial sampling introduces more savings in data acquisition times. Another important property of the proposed method is its ability to resolve closely spaced targets that can not be resolved by the standard migration methods. The increased resolution is because the proposed method doesn't perform a match filtering operation which itself results the resolution limit, rather it tries to explain the measurements using several elements from a dictionary of measurements. Next we develop the theoretical basis and show simulated and experimental data results.

2.3.1 Theory of Compressive Imaging for SFCW GPRs

As the SFCW GPR scans a region, at each scan point it transmits a continuous sinusoidal signal sequentially changing frequency. The transmitted signal for the l-th frequency, $f_l = f_0 + l\Delta f$ can be written as

$$E_T = A \exp^{-j2\pi(f_0+l\Delta f)t} = A \exp^{-jw_l t} \tag{30}$$

where $l = 0, 2, ...L - 1$ with L being the total number of frequency steps, Δf the frequency step interval and f_0 is the initial frequency. A is the strength of the transmitted signal.

In the case of a mono-static GPR antenna in a homogeneous medium with a single target at distance R, the received signal can be written as

$$E_R = \frac{A}{R^4}\sigma \exp^{j(2kR - w_l t)} \tag{31}$$

when the signal in (30) is transmitted. In (31) σ is the scattering cross section and k is the propagation constant.

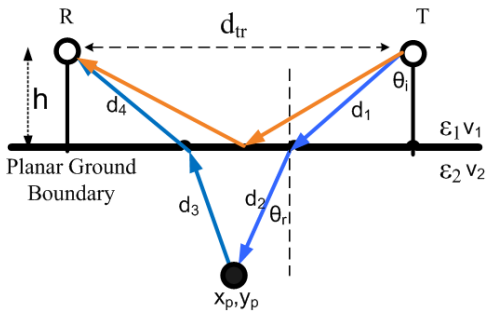

Figure 27: GPR measurement setup showing a bistatic scenario.

However, a two-layer scenario as shown in Fig. 27, where a bistatic GPR sensor is situated at a known height from the ground/air interface with buried targets is a more general and realistic one. According to the ray theory view of wave propagation, the transmitted signal follows the path in Fig. 27. The received signal for a single target at position p when the GPR is at aperture i can be written as

$$E_R = A'\sigma \exp^{j(k_1(d_1+d_4)+k_2*(d_2+d_3)-w_l t)} = A'\sigma \exp^{jw_l(t-\tau_i(p))} \tag{32}$$

where k_1 and k_2 are the propagation constants in air and soil, respectively. The same received signal is also written in (32) in terms of the total time delay $\tau_i(p) = (d_1 + d_4)/v_1 + (d_2 + d_3)/v_2$, where v_1 and v_2 are the propagation velocities in air and soil.

To incorporate any prior information about the target space into the estimation of unknown spatial image, we would like to relate the measurements linearly to the spatial domain as

$$d(u_x, u_y, f) = \mathbf{\Psi} g(x, y, z) \tag{33}$$

where $g(x, y, z)$ is the target space, $d(u_x, u_y, f)$ is the space-frequency measurements and $\mathbf{\Psi}$ is the operator defining the transform between the two spaces. In practice we have a discrete version of (33) in which a sampled g is related to the observed discrete (noisy) frequency data through a linear discrete operator (i.e. a matrix $\mathbf{\Psi}$).

2.3.1.1 Creating a dictionary for frequency domain GPR data

To create the forward model $\mathbf{\Psi}$, the target space $\boldsymbol{\pi}_T$ which lies in the product space $[x_i, x_f] \times [y_i, y_f] \times [z_i, z_f]$ must be discretized. Here (x_i, y_i, z_i) and (x_f, y_f, z_f) denote the initial and final positions of the target space to be imaged along each axis. Discretization generates a finite set of target points $\mathcal{B} = \{\boldsymbol{\pi}_1, \boldsymbol{\pi}_2, \ldots, \boldsymbol{\pi}_N\}$, where N determines the resolution and each $\boldsymbol{\pi}_j$ is a 3D vector $[x_j; y_j; z_j]$. For any discrete target position the model frequency data for each frequency step and each aperture point can be calculated using (32) with $\sigma = 1$. For example, when the GPR is at the ith aperture point, the jth column of $\mathbf{\Psi}_i$ which corresponds to a target at $\boldsymbol{\pi}_j$ can be written as

$$[\mathbf{\Psi}_i]_j = A' \exp^{-jw(t-\tau_i(\boldsymbol{\pi}_j))} \tag{34}$$

Repeating (34) for each discrete possible target position creates the dictionary $\mathbf{\Psi}_i$ of size $L \times N$ when the GPR is at the ith aperture point.

The received signal at the ith aperture point for multiple targets can be written as

$$\boldsymbol{\zeta}_i = \sum_{k=1}^{P} A'(\boldsymbol{\pi}_k)\sigma_k \exp^{-jw(t-\tau_i(\boldsymbol{\pi}_k))} \tag{35}$$

assuming that the targets do not interact so superposition is valid. The received

signal from multiple targets can be written in terms of the dictionary as

$$\boldsymbol{\zeta}_i(f) = \boldsymbol{\Psi}_i \boldsymbol{b} \tag{36}$$

where $\boldsymbol{b}$ is a weighted indicator vector, i.e. if there is a target at $\boldsymbol{\pi}_j$, the jth index of $\boldsymbol{b}$ should be nonzero. Our goal is to find $\boldsymbol{b}$ which is actually an image of the medium.

2.3.1.2 Random Frequency Sampling

Standard SFCW GPRS measures all L frequencies at each aperture point, hence the dimension of $\boldsymbol{\zeta}_i$ is $L \times 1$. We present a new data acquisition model based on compressive sampling (CS)[31, 15, 4] which would require many fewer samples to construct the target space image $\boldsymbol{b}$, if the target space is sparse. We measure a random subset of M frequencies, where $M < L$ at each aperture point. In matrix form the new measurements $\boldsymbol{\beta}_i$ can be written as

$$\beta_i = \boldsymbol{\Phi}_i \boldsymbol{\zeta}_i = \boldsymbol{\Phi}_i \boldsymbol{\Psi}_i \boldsymbol{b}. \tag{37}$$

where $\boldsymbol{\Phi}_i$ is an $M \times L$ measurement matrix constructed by randomly selecting some rows of an $l \times L$ identity matrix, which amounts to measuring random frequency points at aperture i. This has a direct implication of reducing the data acquisition time by a factor of L/M for SFCW GPRs. Note that $\boldsymbol{\Phi}_i$ which defines the measurements might be different for each aperture point. The effects of selecting same or changing $\boldsymbol{\Phi}_i$ for each aperture will be discussed in Section 2.3.4

2.3.1.3 Compressive GPR Imaging

For imaging we use K aperture points and form a "super problem" with the combined matrices $\boldsymbol{\Psi} = [\boldsymbol{\Psi}_1^T, \ldots, \boldsymbol{\Psi}_K^T]^T$, and $\boldsymbol{\Phi} = \text{diag}\{\boldsymbol{\Phi}_1, \ldots, \boldsymbol{\Phi}_K\}$, and the measurements $\boldsymbol{\beta} = [\boldsymbol{\beta}_1^T, \ldots, \boldsymbol{\beta}_K^T]^T$. The result of the CS theory is that the target space indicator vector $\boldsymbol{b}$ can be recovered exactly from $M = C\left(\mu^2(\boldsymbol{\Phi}, \boldsymbol{\Psi}) \log N\right) K$ measurements $\boldsymbol{\beta}$ with overwhelming probability [15], by solving the ℓ_1 minimization problem

$$\hat{\boldsymbol{b}} = \text{argmin} \, \|\boldsymbol{b}\|_1 \qquad s.t. \quad \boldsymbol{\beta} = \boldsymbol{\Phi}\boldsymbol{\Psi}\boldsymbol{b} \tag{38}$$

where $\mu(\boldsymbol{\Phi}, \boldsymbol{\Psi})$ is the coherence between $\boldsymbol{\Phi}$ and $\boldsymbol{\Psi}$ defined as in [15].

The optimization problem in (38) is valid for the noiseless case because it uses an equality constraint. If the GPR signal is noisy, i.e., $\zeta_i^N(t) = \zeta_i + n_i(t)$, then the compressive measurements $\boldsymbol{\beta}_i$ at the ith aperture position have the following form:

$$\boldsymbol{\beta}_i = \boldsymbol{\Phi}_i \boldsymbol{\zeta}_i = \boldsymbol{\Phi}_i \boldsymbol{\Psi}_i \boldsymbol{b} + \boldsymbol{u}_i \tag{39}$$

where $\boldsymbol{u}_i = \boldsymbol{\Phi}_i \boldsymbol{n}_i \sim \mathcal{CN}(0, \sigma^2)$ and $\boldsymbol{n}_i$ is the concatenation of the noise samples at aperture point i which is assumed to be $\mathcal{CN}(0, \sigma_n^2)$, i.e.,a complex normal distribution. Since $\boldsymbol{\Phi}_i$ is deterministic, we have $\sigma^2 = (\sum_{n=1}^{N_t} \boldsymbol{\phi}_{imn}^2)\sigma_n^2$. Hence, if we constrain the norm of the $\boldsymbol{\phi}_{im}$ vectors to be one, then $\sigma^2 = \sigma_n^2$.

It is shown in [12, 14, 55, 34] that a stable recovery of the sparsity pattern vector $\boldsymbol{b}$ is possible by solving a modified convex optimization problem,

$$\hat{\boldsymbol{b}} = \arg\min \|\boldsymbol{b}\|_1 \qquad \text{s.t.} \quad \|\boldsymbol{A}^T(\boldsymbol{\beta} - \boldsymbol{A}\boldsymbol{b})\|_\infty < \epsilon \tag{40}$$

where $\boldsymbol{A} = \boldsymbol{\Phi}\boldsymbol{\Psi}$. Solution by constraining the ℓ_2 norm of the reconstruction error as in (**??**) is also possible. The ϵ parameter can be selected by cross-validation similar to impulse GPR case (See Section 2.2.4).

2.3.2 Simulated Example for SFCW GPR Imaging

First, we give a test example to illustrate the random frequency sampling idea. Let's assume a 2D homogeneous target space of size 30 cm × 30 cm containing three randomly placed point targets. A bistatic antenna with a 5 cm transmitter-receiver distance at a height of 10 cm collects frequency domain measurements at frequencies 100 MHz to 10 GHz with 100 MHz frequency steps. Thus at each aperture point the GPR collects 100 frequency measurements. The true target space image and the noisy space-frequency domain measurements are shown in Figs. 28 (a,b). The signal-to-noise ratio (SNR) for this example is 0 dB.

Instead of measuring all 100 frequencies we only use a random subset of 20 frequencies at each aperture. The randomly measured frequencies are indicated by black

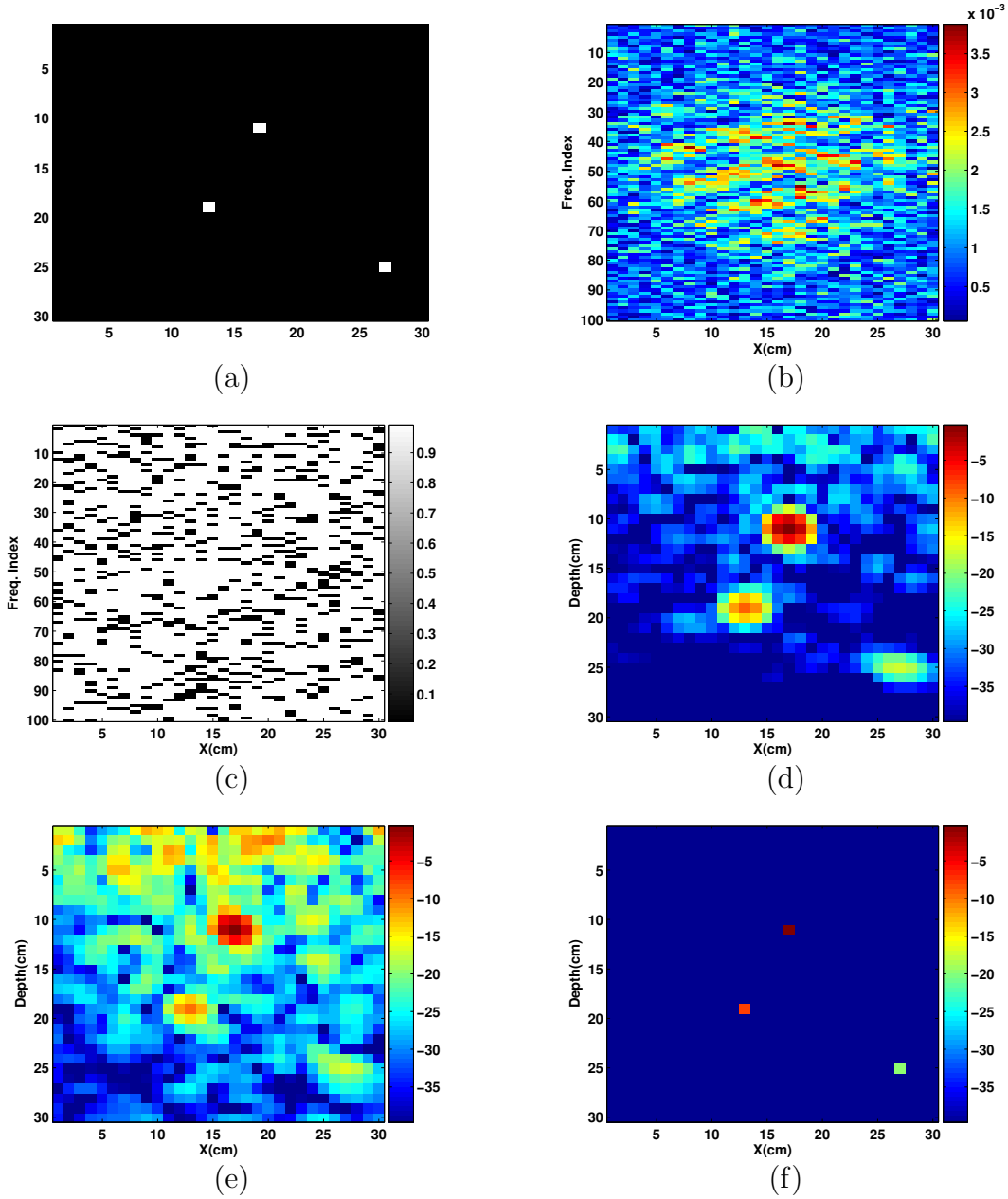

Figure 28: (a) Target space, (b) Noisy space-frequency domain target space response at $SNR = 10\,\text{dB}$ for 30 aperture points, (c) Black points indicate the randomly measured frequencies when 20% of the total frequencies are used, (d) Frequency domain backprojection image using all the space-frequency domain data from (b), (e) Frequency domain backprojection method using only the randomly selected 20%, (f) Solution obtained with the proposed method using (40).

points in Fig. 28(c). If we had measured all the space-frequency domain data and applied frequency domain backprojection we would obtain the image show in Fig. 28(d).

The three targets can be seen clearly with small 'blobs' around the correct target position. If we apply frequency domain backprojection to the randomly selected data, the created target space image is severely degraded as shown in Fig. 28(e). For the proposed method solving (40) using the randomly selected data generates the target space image shown in Fig. 28(f). For the numerical solution of (40) a convex optimization package called `CVX` [44] was used. The proposed method finds the correct target positions with less clutter since the convex optimization program forces sparse solutions. All the target space images in Fig. 28(d,e,f) are normalized to their own maxima and are shown on the same 30 dB scale. As seen from the results while using a small number of frequencies, the proposed method could generate a less cluttered image that is better than the backprojection method using all the frequency data.

As part of the testing, the target space image was formed 100 times by selecting an independent random measurement matrix at each time and applying the proposed algorithm. It is observed that the algorithm introduces no bias to the target position estimates. Likewise any random subset of frequencies works equally well as long as it contains more than the minimal number of measurements. The performance of the algorithm in varying noise levels and the effect of using a different number of frequencies are discussed next.

2.3.3 Performance in Noise

The noise level effects the estimated target positions and the created subsurface images. To analyze this effect two simulations are done. First, the frequency domain GPR data for a single point target is generated. SNRs from -25 dB to 15 dB are tested and at each SNR level, 50 different trials with using additive independent zero mean complex white gaussian noise (CWGN) with corresponding variance at each trial. The target space is constructed by CS algorithm using (40) and the BP with with varying number of frequency measurements at each aperture. For each SNR level

the variance of the estimated target locations is calculated and plotted in Fig. 29(a) for BP and the CS method[3]. It can be observed that the CS method using the same number of frequency measurements has smaller variances than the BP method. BP's variance for moderate to high SNRs doesn't change too much due to the resolution limit it can achieve. Our method provides much lower variances indicating increased resolution, which is also observed in similar sparse signal reconstruction applications [33, 73] and discussed for our method in Section 2.3.5.

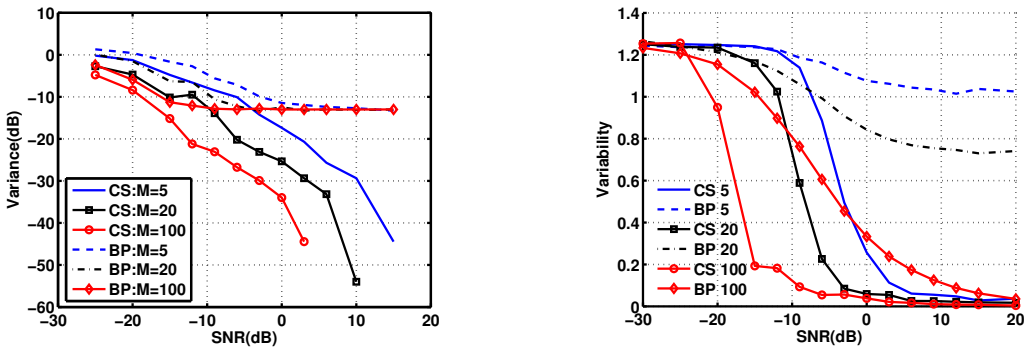

(a) (b)

Figure 29: (a) Target position variance vs. SNR. (b) Variance of the created images vs. SNR. Comparison between variances of BP and the CS method. M is the number of frequencies used.

Secondly, we looked into the effect of noise on the created images. For this, frequency GPR data is generated for three random point targets and corrupted with additive CWGN. After 50 trials, Fig. 29(b) shows the normalized variance of the constructed images changing with SNR level. Smaller image variance is an indication of both a correctly reconstructed and sparse image. The CS method has much lower image variance than BP using the same number of measurements. This is because our method favors sparse solutions. This also indicates that our method is more robust compared to BP when the frequency measurements are selected at random.

[3]To obtain the plot in Fig. 29(a) we used a grid size of 0.01 cm to get estimates not limited to a coarse grid.

2.3.4 Random Spatial Sampling

A joint convex optimization problem using frequency measurements from different aperture points is solved in (40) to create the target space image. The measured aperture points might be at random, and the selected spatial positions can be reduced to a minimal number required for correct target space reconstruction. In Fig. 28, 20 frequency measurements at 30 aperture points were used. In this example the same data set is used, but now 20 random frequencies are measured at only 10 of the 30 randomly selected aperture points. The measured space-frequency points are shown in Fig. 30(a). It can be observed that while reducing spatial samples highly degrades the backprojection image, the proposed method could still generate a comparable image to the full aperture case.

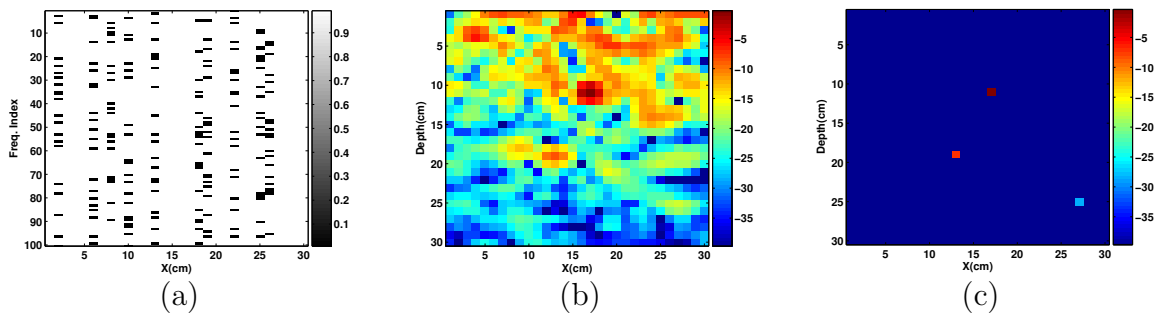

Figure 30: (a) Space-time domain response of the target space to the GPR data acquisition process at randomly sampled spatial aperture positions, (b) Compressive measurements at the sampled aperture positions, (c) Target space image obtained with the proposed method, (d) Target space image obtained with time domain backprojection.

To better compare the effect of reduced random spatial sampling on the proposed method and the frequency domain backprojection a Monte Carlo simulation is performed. Noisy GPR data of three point targets are generated for 30 aperture points with SNR = 10 dB. The target space is constructed using a subset of the random frequency measurements while varying the number of aperture points from 6 to 30. A subset of aperture points is randomly selected and the target space is reconstructed

Table 5: Image variance with varying number of spatial samples for stepped-frequency GPRs

Reduced Spatial Sampling Test					
No of Apertures		30	20	10	6
Case 1	CS	0.020	0.048	0.083	0.167
	BP	0.745	0.868	0.976	1.072
Case 2	CS	0.020	0.040	0.083	0.135
	BP	0.745	0.778	0.801	0.824

with (40) using only the measurements from the selected aperture points. This procedure is repeated 100 times with random aperture selections at each time. Two cases are tested. In Case 1, $M = 20$ out of 100 frequencies are measured at the selected aperture points, which makes 600 total measurements when all 30 aperture points are used. In Case 2 the number of total measurements is kept at 600, i.e., when 15 aperture points are used $M = 40$ in Case 2, while Case 1 still takes $M = 20$ measurements. Table 5 shows the normalized variance versus the number of aperture points, for two cases of the proposed method and backprojection.

It can be observed from Table 5 that decreasing number of aperture increases the variance of the target space image for both algorithms, even in the case where total number of frequency measurements are fixed (Case 2). But the new CS method (CS) has much lower variance than the backprojection (BP) method using the same measurements. This means that the CS method is more robust to the random selection of frequencies or aperture points. In comparing Case 1 & 2, increasing the number of measurements at each aperture point doesn't decrease the variance for CS significantly, but additional measurements reduces the variance for BP. This shows that additional measurements beyond a minimum required number is not significant for the CS method and can be skipped.

2.3.5 Increased Resolution Property

One of the important properties of the CS method is its ability to resolve closely spaced targets that cannot be resolved by the standard migration methods. The range resolution for an SFCW GPR can be given by $\Delta R = c/(2L\Delta f)$ where Δf is the frequency step, L is the number of frequency steps and c is the speed of the wave in the medium. To analyze the increased resolution property, a simulation is done. First, two point targets in air are assumed at positions (0,45) cm and (0,55) cm with a separation of 10 cm in height. The GPR antenna scans the region (−30,30) cm along the x axis in 2 cm steps and at each aperture point collects data from 3 GHz to 5 GHz in $\Delta f = 20$ MHz increments at $N = 100$ frequency steps. For this simulated case, the range resolution is 7.5 cm. Figures 31(a) and (b) show the target space

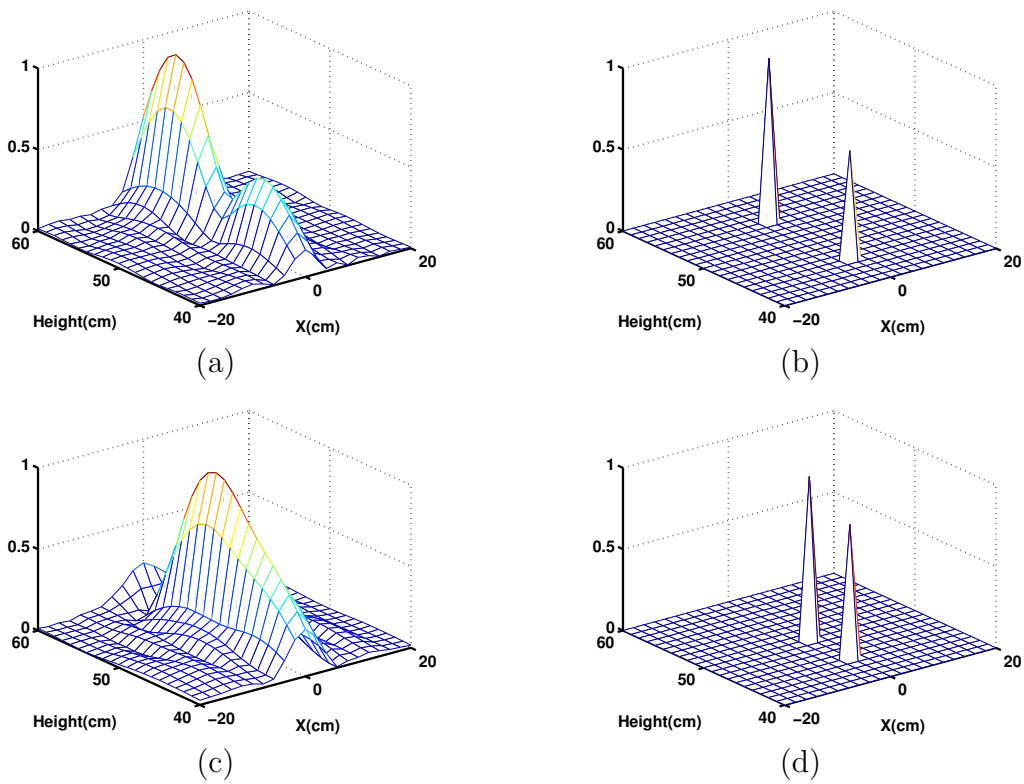

Figure 31: Increased resolution property results: (a) Backprojection (b) compressive sensing images when source separation is 10 cm. (c) Backprojection (d) compressive sensing images when source separation is 5 cm.

constructed using the BP and the CS method respectively. Although the CS method creates a much sparser target space, both methods could resolve the two targets. If the two targets are put closer at (0,45) cm and (0,50) cm with a separation of 5 cm which is smaller than the resolution limit at the used bandwidth, Figs. 31(c) and (d) are obtained as the target space images from BP and CS, respectively. While the BP cannot resolve the two targets because they merge into a single peak, both targets can be seen clearly resolved at their correct positions with the CS method. This is because the CS doesn't perform a matched filtering operation which itself results the resolution limit, rather CS tries to explain the measurements using several elements from a dictionary of measurements. The sparsity information about the image yields this increased resolution similar to observations done in other sparse signal reconstruction applications [33, 73].

2.3.6 Effect of Bandwidth

The bandwidth of the measured frequency spectrum is an important parameter in the SFCW GPRs. It is observed that the proposed method can generate sparse target space images even using small bandwidths where standard imaging methods fail to generate a focused image. To see the effect of bandwidth the following test is done. A sample target space containing two point targets at (10,37) and (−10,37) is imaged using bandwidths of 1, 3 and 7 GHz. One hundred trials are made and at each trial a random half of the frequency points for each bandwidth case is randomly measured with random WGN noise added to the measurements at an SNR of 10 dB. The mean of the generated target space images using backprojection and the proposed method are shown in Fig. 32. While increasing the bandwidth results in more focused images for BP, the CS method is more robust to change in bandwidth and could find the sparsest image even for low bandwidth case of 1 GHz.

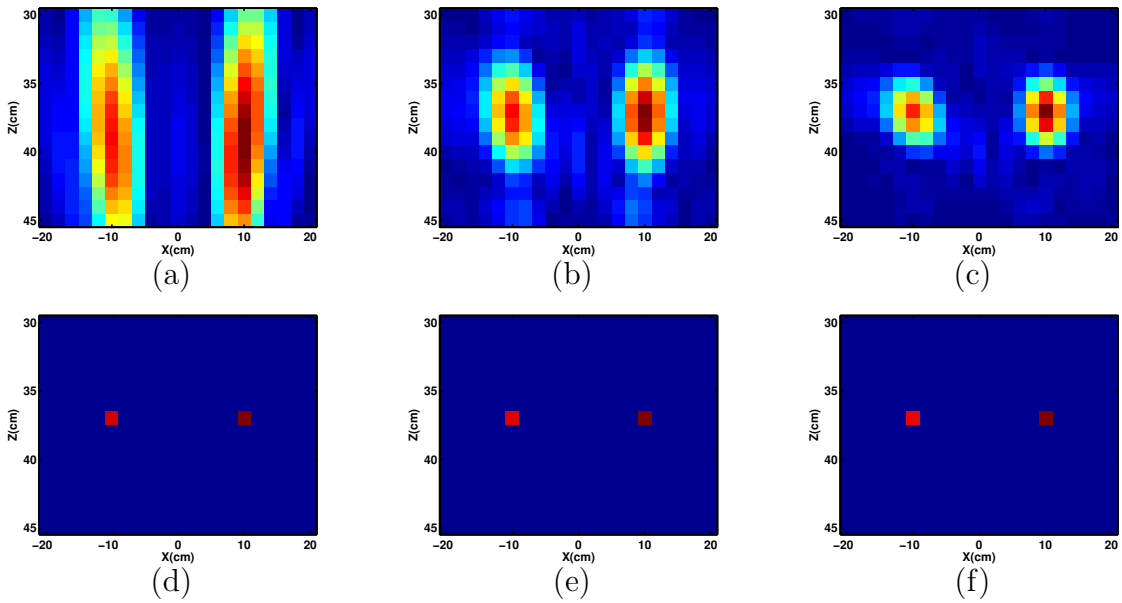

Figure 32: Comparison of effect of the used bandwidth on the target space image created by both backprojection and the proposed method. (a), (b) and (c) are target space images created by BP at bandwidths of 1[3.5-4.5], 3[2.5-5.5] and 7[0.5-7.5] GHz respectively. (d),(e) and (f) are target space images created by PM at bandwidths of 1, 3 and 7 GHz respectively.

2.3.7 Experimental Results

The proposed algorithm is tested on the experimental SFCW GPR data collected from a model mine field at the Georgia Institute of Technology [24, 47]. The GPR antenna [64] consists of 8 bistatic pairs having varying transmitter-receiver distances, but for the results shown in this section only the data from the closest bistatic pair is used. The GPR sweeps 401 equally-space frequency points from 60 MHz to 8.06 GHz. For comparison reasons the full space-frequency domain data is measured and the random frequency selection results are created by only using the selected measurements. We only used the data from 500 MHz to 8.06 GHz which corresponds to 379 frequency points since the low frequency information suffered from interference. The data is publicly available online at `http://users.ece.gatech.edu/wrscott/` in Matlab format files. Two scenarios are tested.

GPR Air Results: This section presents imaging of a 1″ diameter metal sphere

held in the air at a height of 36.5 cm on a styrofoam support. The experimental setup is shown in Fig. 33(a). Since the GPR antenna and the target are in air, the wave speed is known to be $c = 3 \times 10^8$ m/s. The GPR scans the region in 2 cm increments at a constant height of 90.8 cm above the ground level. The metal sphere is positioned at $x = 0$ cm. The magnitude of the raw frequency domain data measured over the target for a 2D slice is shown in Fig. 33(b). Note that this data contain the reflection from the sphere as well as the surface of the sand.

If we had measured the all the space-frequency data and imaged the target space using BP we would obtain the top figure in Fig. 33(c). Instead of using all the space-frequency data, only 30 out of 379 frequency points are randomly selected at each aperture to be used for imaging. This gives more than a factor of 10 savings in data acquisition time if we only measure these frequencies. Applying backprojection to this randomly sampled data results the middle image which is severely degraded compared to the top image. However the CS method using the same randomly selected data set generates the bottom image shown in Fig.33(c). It can be seen that a sparse image with much less clutter than BP, consisting of several point targets near to the top of the metal sphere which explains the measured data well enough with maximum sparsity is generated.

Another scheme for reducing the number of measurements would be uniform sampling over the bandwidth with a low number of frequency steps. Backprojection and the CS method are applied to the data which uses only 30 frequencies uniformly sampled over the full bandwidth at each aperture point. The BP image shown in top of Fig. 33(d) is a more focused image than the one created using randomly selected data, however still it is more cluttered than the full data BP or the CS-processed image shown in bottom of Fig. 33(d). While the BP image varies significantly with a change in the subset of frequencies, the CS method is more robust to the frequency selection.

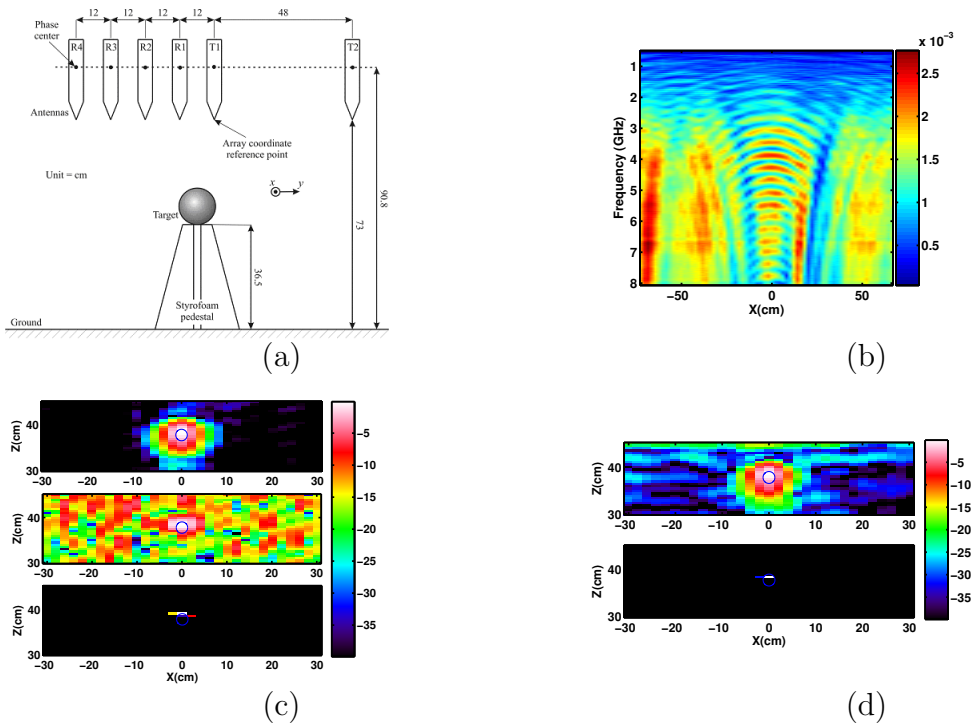

Figure 33: (a) Experimental setup for GPR Imaging,(b) Magnitude of the space-frequency domain measured GPR Response of a 1″ metal sphere in air. (c) Top image uses all space-frequency data and generated by backprojection. Middle and bottom images are random frequency selection results generated by backprojection and CS method. (d) Uniform frequency selection results. Circle on the images indicates the true location and size of the sphere.

Buried Target Results: As an experiment, two anti-personal TS-50 mines and a nylon cylinder is buried in a sandbox at varying depths. The targets are buried at different y locations, but share the same x coordinates. The SFCW GPR measures a line scan over the targets. The phase centers of the antennas are elevated 27.8 cm. The transmitter-receiver distance for the used pair is 12 cm. The spatial step size for GPR is 2 cm. Figure 34(a) shows the experimental setup and the actual target positions with corresponding estimate sizes. At each point 379 frequency points are measured. The magnitude of the measured raw frequency domain data is shown in Fig. 34(b).

The frequency domain BP result using all the space-frequency data is shown in Fig. 34(c). The three objects can be seen in the migrated BP image. The CS method

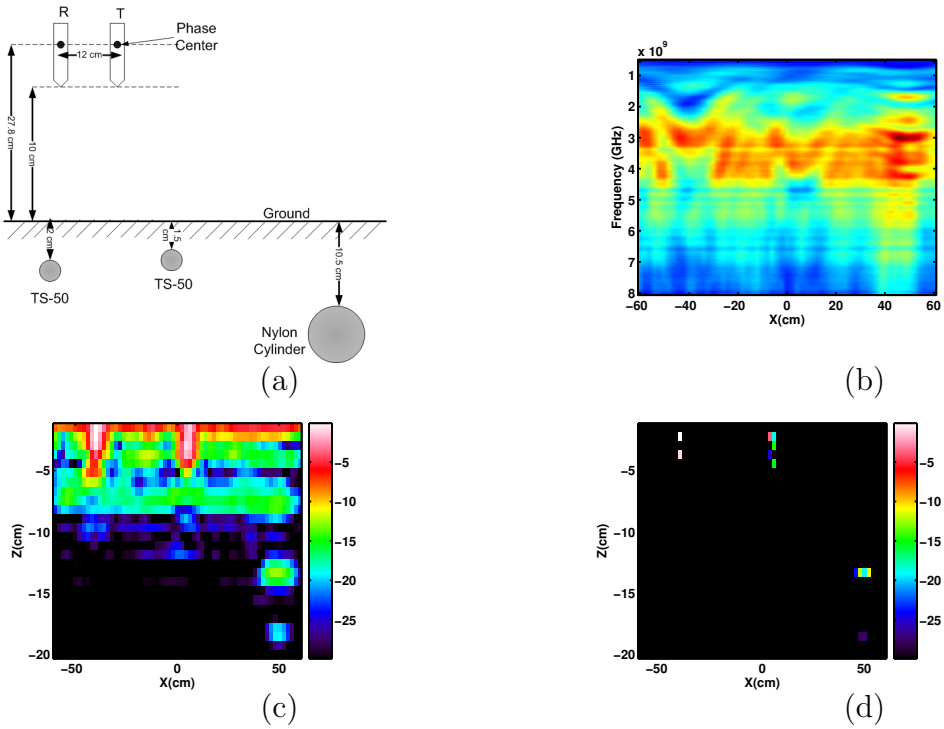

Figure 34: (a) Experimental setup for buried target imaging,(b) Magnitude of the space-frequency domain measured GPR Response of 3 buried targets Target space image obtained with (c) BP and (d) compressive sensing.

uses 100 random frequency points instead of 379 and yields the target space image in Fig. 34(d). Note that the refections in Fig. 34(b) are mostly due to the reflection off the surface with only a minor part due to the mines. Both methods are pulling these small mine reflections out of the larger surface reflection. In the CS result all the targets can be seen with less clutter in the image. Both Figs. 34(c) and (d) are normalized to their own maxima and are shown on a 30 dB scale.

2.4 Conclusions

In this chapter a novel data acquisition and imaging algorithm for both impulse and stepped frequency GPRs based on compressive sensing was demonstrated. The new method exploits prior knowledge of the sparseness in the target space. An ℓ_1 minimization convex optimization problem is solved with a small number of random compressive measurements taken at randomly chosen aperture points to reconstruct

the target space image. Results from simulated and experimental GPR data show that extremely sparse images can be obtained with the proposed method compared to standard backprojection imaging algorithms.

CHAPTER III

HOUGH TRANSFORM BASED FEATURE DETECTION

The Hough Transform (HT) [56], its variants and their generalizations [7, 35, 3, 61] are the most commonly used methods capable of detecting parameterized shapes in images. However, there are several challenges associated with applying the HT to subsurface images. One is that very weak objects like tunnels may be hidden by high clutter and noise which would not allow a simple thresholding algorithm to detect the features. This low SNR problem is very common in GPR or seismic subsurface images. Another challenge is that the subsurface features don't have known parameterized shapes, which decreases the effectiveness of the HT algorithm. Although this thesis doesn't provide a comprehensive solution for curving features, in this chapter we concentrate on detection and provide solutions to the above mentioned problems based on the HT. A detailed explanation of HT is given in Section 1.2.2.

3.1 Iterative Detection of Linear Objects in GPR and Seismic Images

Hough transform applications mostly involve taking the 2D and 3D Hough transforms of backprojected GPR and seismic images followed by a detection algorithm which uses simple thresholds. The main drawback of this type of detection technique is that very weak linear objects like tunnels may be hidden by high clutter and noise. For example, the presence of tunnels at shallower depths may mask the signature of a deeper tunnel (with a lower returned power level) or a small clutter object like a coke can with a high returned power can dominate the parameter space of the HT.

This section provides a HT based iterative method that finds and removes linear objects one by one at each iteration. In this way, even weaker linear objects are

revealed and detected. Contrary to the typical iterative algorithms for GPR imaging [29] that invert the detected point in Hough space and enlarge the area around this line to find an estimate area for the linear object, we use the signature of a rectangular object in Hough space to directly remove the corresponding rectangular area from the image.

The presented iterative linear object detection algorithm can be summarized with the following steps:

1. Apply HT as given by (5) to the backprojected image
2. Find the maximum point in parameter space
3. Estimate the width and length of the linear object area from the HT signature and the image space.
4. Remove the estimated linear object
5. If the termination criterion (Section 3.1.2) is not met, then go to 1, else terminate.

3.1.1 Estimating Linear Object Area

To find the area of the linear object we need to estimate both the length and width of a rectangular area that corresponds to the linear object for that iteration. The algorithm is developed using a slope and intercept formulization of the HT as in (4). The length of the object can be estimated by analyzing the pixel values along the main target line corresponding to the selected maximum point in parameter space. The intensity values of the pixels along the line can be represented as a 1D function (Fig. 35(d)) and the object length can be identified by setting a threshold (e.g., 50% of the peak value) along the line.

The HT of nearly rectangular shapes is a diamond-shaped area in parameter space [50]. The spread of this area on the n-axis is used to determine the upper and

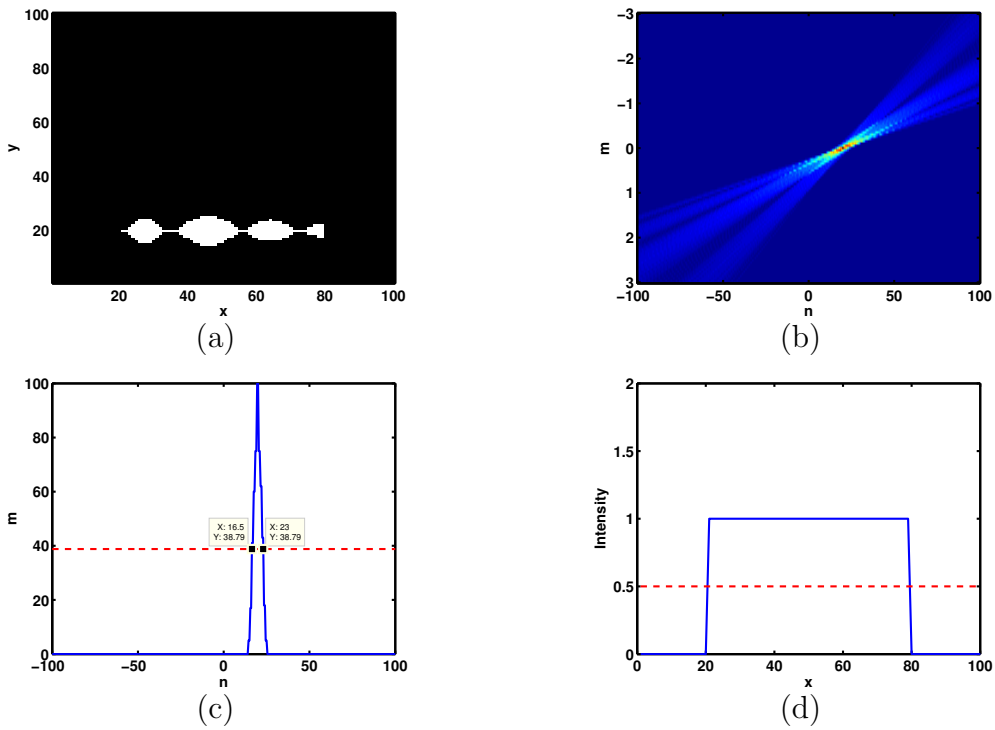

Figure 35: (a) Simulated linear object signature in seismic or GPR backprojected images, (b) Hough Transform of the image,(c) Estimation of y-crossing values for upper and lower bound lines, (d) Linear object length estimation

lower boundary lines for the area to be removed. Figure 35(c) shows the values of the HT of the image in Fig. 35(a) at $m = m_{\max}$ for all n values. Setting up a threshold determines the y-crossings for the upper and lower bound lines of the linear object area. We denote those values as n_l and n_u and $1/e$ of the maximum value is used as the threshold for the results shown in Section 3.1.3.

The lines that correspond to the slopes and intercepts $(m_{\max}, n_l)$ and $(m_{\max}, n_u)$, along with the length and starting point of the linear object will bound the area to be removed at that iteration. The estimated area is removed by zeroing out the corresponding data values and then the Hough transform of the new image is taken to find any remaining linear objects (unless the termination criterion is met).

3.1.2 Termination Criterion

An important aspect of the iterative detection process is defining the termination criterion. The algorithm should stop when there are no extended linear objects left in the image. In such a situation the image consists of only noise, so the HT of the image consists of many smaller local maxima, rather than a prominent maximum. Using this property, when there are more than a selected number of comparable local maxima (we used five), the iteration is terminated.

3.1.3 Simulation Results

Linear objects like tunnels and pipes appear as "blobs" in GPR and seismic images [29, 51, 48]. For simulated images these blobs are generated by selecting random blob lengths and amplitudes as well as random inter-blob distances. For illustration a simulated image with two tunnels is generated. The main target lines for the tunnels are $m_1 = -1$, $n_1 = 90$ and $m_2 = 2$ and $n_2 = -30$. The signal amplitudes for Tunnels 1 and 2 are 2 and 100, respectively; thus Tunnel 2 has a signal level 50 times higher than that of Tunnel 1. White Gaussian noise (WGN) with mean 0 and variance 1 is added. The resultant image is shown in Fig. 36(a).

The HT that corresponds to the image in Fig. 36(a) is shown in Fig. 36(b). Note that the signature of the lower power level tunnel cannot be seen in the HT image. It is very hard for non-iterative detection algorithms to find the lower power tunnels since they are masked by noise and other tunnels. When the first iteration of the algorithm is applied, Tunnel 2 is removed and the new image for the second iteration is obtained (Fig. 36(c)). Fig. 36 (d) shows the HT of the image in Iteration 2. Notice how the peak for Tunnel 1, masked in Fig. 36(b), can now be clearly seen in Fig. 36(d). When the new tunnel area is estimated and removed from the image, Fig. 36(e) is found as the Iteration 3 image. Now, a significant peak is not present. Rather, 68 comparable local maxima are found, and the algorithm is terminated.

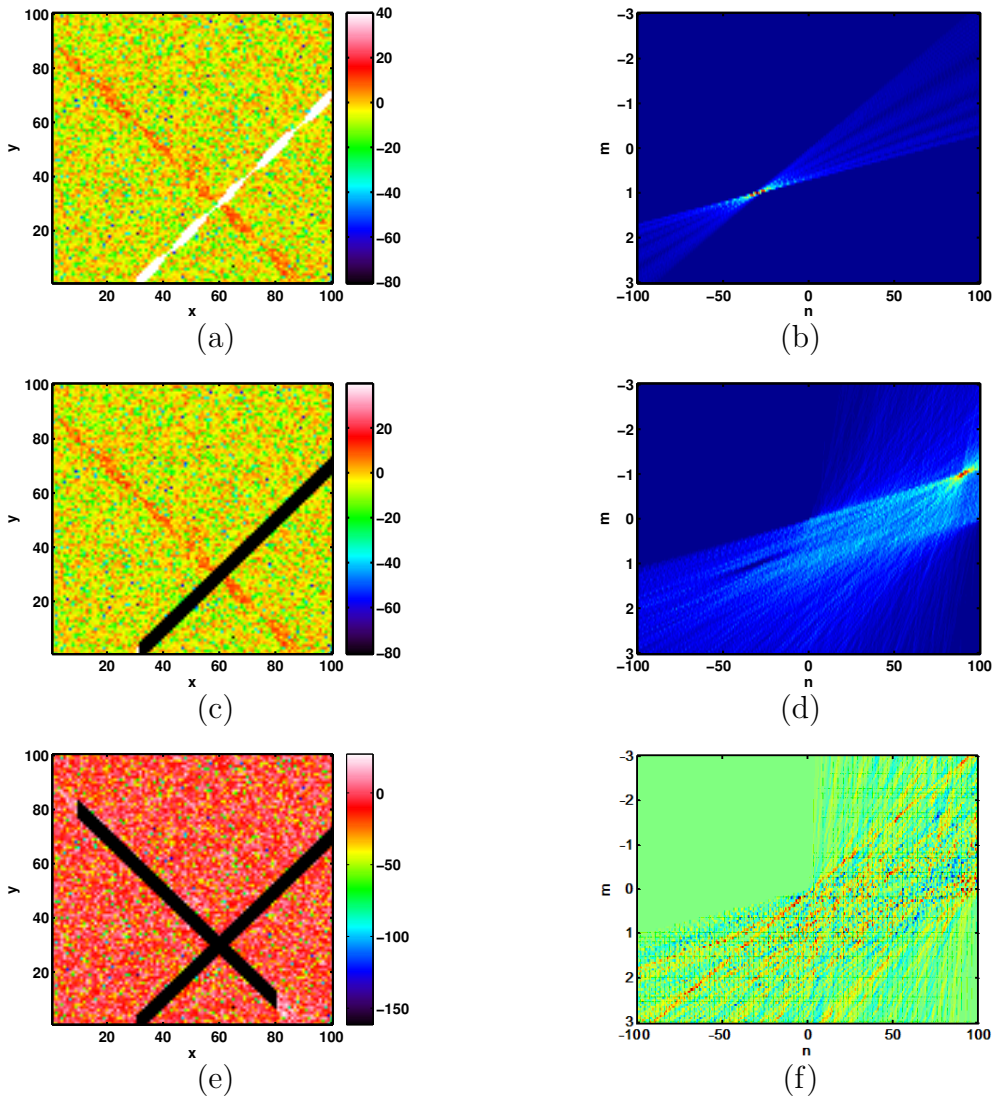

Figure 36: (a) Simulated image with two Tunnels, (b) Hough transform of image in (a), (c) Iteration 2 Image, (d) Hough transform of image in (c), (e) Iteration 3 image, (f) Hough transform of image in (e).

In the second simulation, 3 small clutter objects are introduced to the image which has two linear objects. Clutter could be any small object like coke cans, land mines etc. Simulated clutter is positioned at $(20:26, 60:66)$, $(85:91, 80:86)$ and $(80:86, 10:16)$ in x and y dimensions with highest signal value 100, 50 and 50, respectively. Main line for the two linear objects are positioned to be at $m_1 = 0$, $n_1 = 50$ and $m_2 = 1$, $n_2 = -10$ with signal values 4 and 10. Note that the clutter values are much higher than the linear objects. White Gaussian noise (WGN) with

mean 0 and variance 1 is added to the image. The resultant image is shown in Fig. 37(a) and the HT of this image is given in Fig. 37(b).

The HT domain image includes some lines and focused points. Note that a point like object in the image appears as a line in the HT and a line in the image domain appears as a focused point in the parameter space. The iterative object removal strategy is applied to the HT domain image shown in Fig. 37(b). The first detected and removed object is the linear object at $m_2 = 1$, $n_2 = -10$ with signal value 10. This object is detected first even though it has a much lower signal values compared to the clutter objects because the summation over the linear object actually results in a higher value for it in the parameter space. The linear object is removed and procedure is reapplied. The second iteration image and its HT are shown in Figs. 37(c)-(d). Note that the focused point due to the removed object is absent in the HT image. At this iteration stage the maximum point in the HT corresponds to the line that passes through two of the clutter objects and both of those objects are removed. In the third iteration one linear object and one clutter object are left. Accordingly, the HT image includes one line and one focused point. This iteration removes the linear object and only 1 clutter object is left for iteration 4. After iteration 4 all detected objects are removed and the image in Fig. 37(i) is obtained. Now the HT domain does not contain any dominant targets and the iteration is stopped. Tunnels which have much lower returned power compared to clutter objects could be successfully detected.

3.1.4 Experimental GPR and Seismic System for Detecting Tunnels

To investigate the potential for new feature detection algorithms an experimental setup using co-located GPR and seismic sensors have been built [82]. These sensors were chosen because they sense very different physical properties and are compatible with simultaneous operation. The seismic sensor is sensitive to the differences between

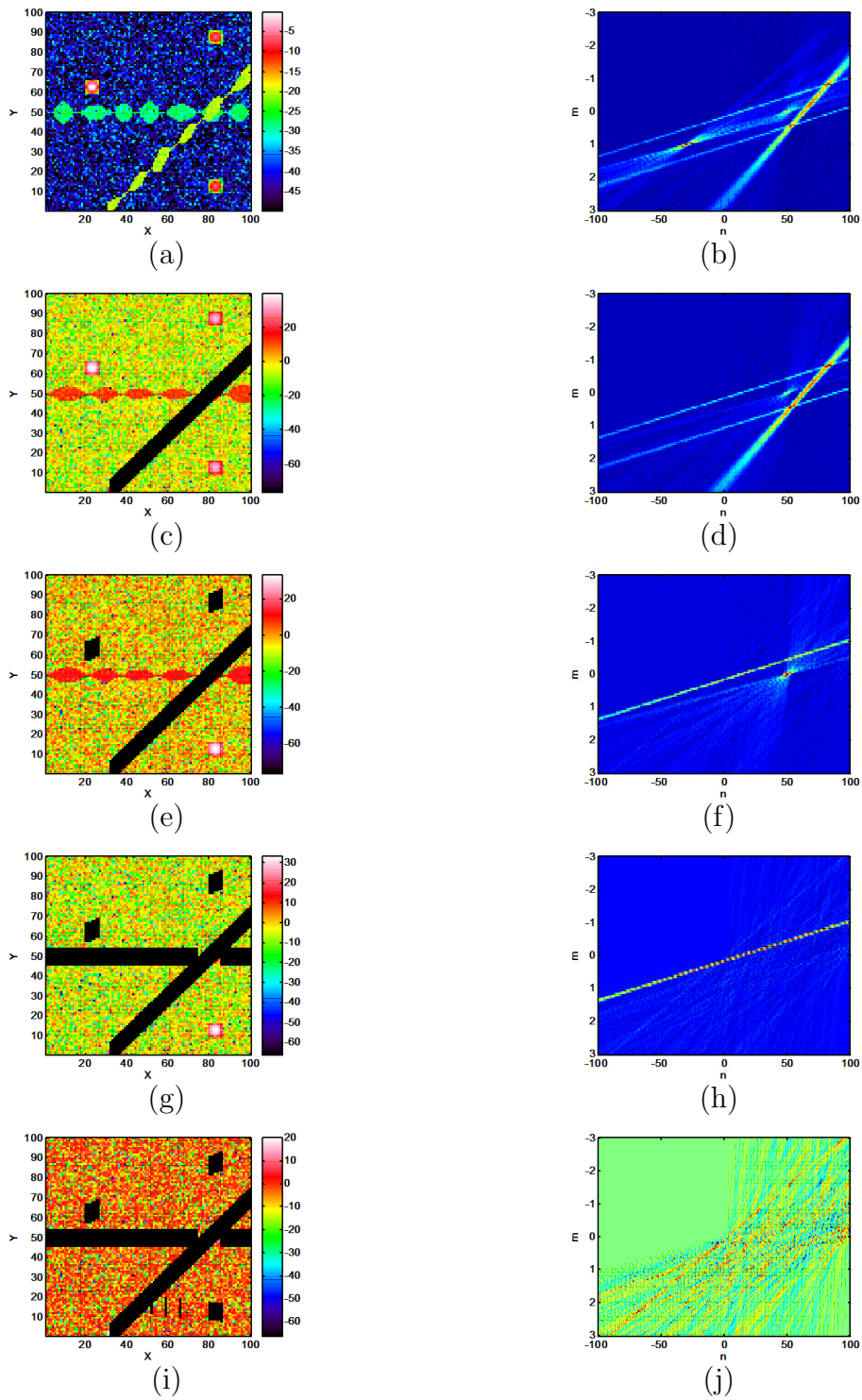

Figure 37: (a) Simulated image with two Tunnels and 3 clutter objects, (b) HT of image in (a), (c) Iteration 2 Image, (d) HT of image in (c), (e) Iteration 3 image, (f) HT of image in (e), (g) Iteration 4 image, (h) HT of image in (g), (i) Iteration 5 image, (j) HT of image in (i)

the mechanical properties of a tunnel and the soil while the GPR is sensitive to the dielectric properties. The loss mechanisms in the soil for the electromagnetic (EM) and the seismic waves are also very different, making it less likely to have prohibitive losses for both wave types in a given soil type.

The GPR sensor was described in Section 2.2.10. The seismic sensor shown in Fig. 1 consists of an aero-acoustic source and a ground contacting receiver. The acoustic source is a 13 cm speaker with a closed box, and the ground-contacting receiver is an accelerometer that is coupled to the ground with a biasing force provided by a tail mass through a spring. The speaker and accelerometer are scanned across the surface using the positioning system. The speaker is excited with a 4 s chirp with frequency content from 100 Hz to 8 kHz.

Two different experimental scenarios have been investigated with scale models of linear structures in an experimental model sandbox filled with nearly-homogeneous sand as shown in Fig. 48(a). A scale model for a tunnel is buried within a 1.8 m x 1.8 m region in the center of the tank. The tunnel is 10cm in diameter and is buried approximately 58 cm deep (the depth varies from 53 to 63 cm), making about a 20 to 1 scale model for a shallow tunnel just big enough for a man to slide through. The sensors are scanned over this region with a three degree-of-freedom positioner. To investigate a more difficult configuration, three PVC pipes with diameters of 1.27 cm, 2.54 cm, and 5.08 cm were buried with variable depths in the model as shown in Fig.48(b) for the second scenario.

The presented method is applied on the experimental data obtained from the scenario shown in Fig. 48(a). Figure 39(a) shows the surface energy image of the seismic sensor, where the energy of the 3D image is summed on depth axis up to the surface. The linear feature at $y = 22$ is the image of a drainage pipe. The other linear object is the reflection image of the sloped bottom of the sandbox in the laboratory. When the HT of the seismic surface energy is taken Fig. 39(b) is obtained. The two

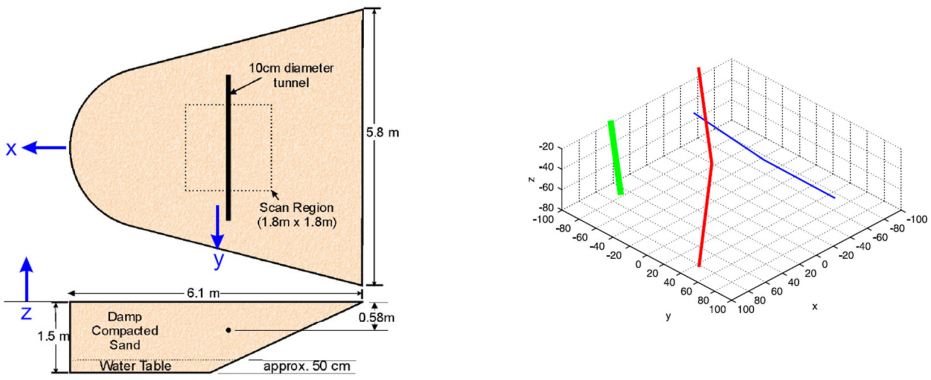

(a) (b)

Figure 38: (a) Model of the sand tank with one 4" tunnel buried approx 58 to 60 cm deep from the surface. (b) Layout of the three buried PCV pipes. The targets are a 2" pipe buried approx 30 cm deep, a 1" pipe buried diagonally from the surface down to 60 cm, and a 0.5" pipe buried approx 60 cm deep. The coordinates of the axes are the same as the coordinates in (a).

linear objects appear as two peaks in the parameter space.

The first iteration finds and removes the buried pipe. The image at Iteration 2 is shown in Fig. 39(c). The HT of Fig. 39(c) has only one significant peak, which corresponds to the sloped part of the sandbox (Fig. 39(d)). When the second linear object is also removed there are no more targets left in the image, therefore no significant peaks remain in parameter space and the iteration process is terminated.

The surface energy image for the GPR is shown in Fig. 40(a). Unlike the seismic case, the sloped part of the sandbox bottom is not clearly seen in the surface energy image of GPR. This is due to the fact that the mechanical contrast between the sandbox bottom and the sand is much higher than the dielectric differences between the two and this mechanical contrast appears in seismic image.

The tunnel is clearly seen in the GPR image but the strength of the response to the tunnel is seen to be much stronger for $1 < x < 50$. Although not verified, one explanation of this might be that water collected in that portion of the tunnel since it is the deepest part. Applying the HT for the first iteration Fig. 40(b) is obtained. There is only one dominant peak in the parameter space which corresponds to the

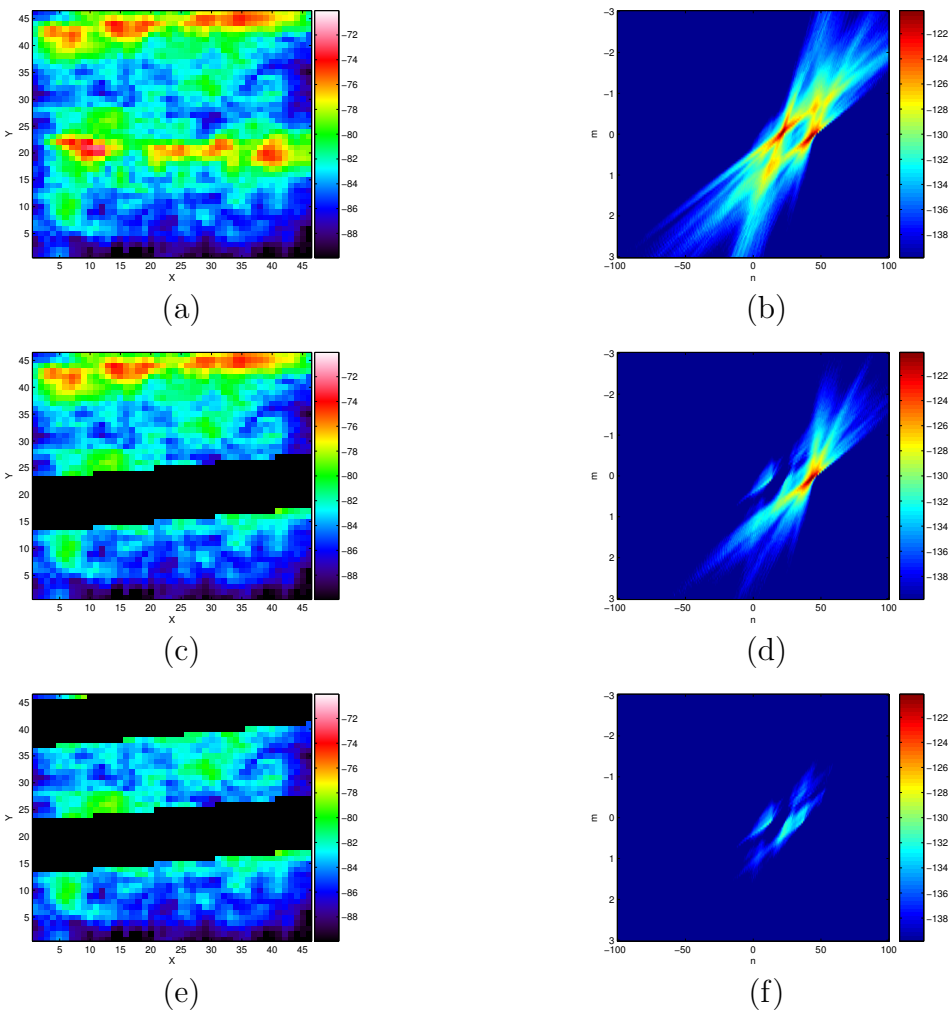

Figure 39: (a) Experimental seismic surface energy image, (b) HT of image in (a), (c) Iteration 2 Image, (d)HT of image in (c), (e) Iteration 3 image, (f) HT of image in (e).

dominant linear object in the GPR image. When the object area is found and removed from the energy image Fig. 40(c) is obtained. The HT of the Iteration 1 image doesn't have a dominant peak and the iteration is stopped.

3.2 Detecting Curved Buried Features Using Partial Hough Transforms

Line detection techniques can be extended to the detection of curves using the generalized Hough Transform (GHT) [35, 88, 54]. Previous work on curve estimation using Hough transforms has focused on the detection of parameterized curves, such

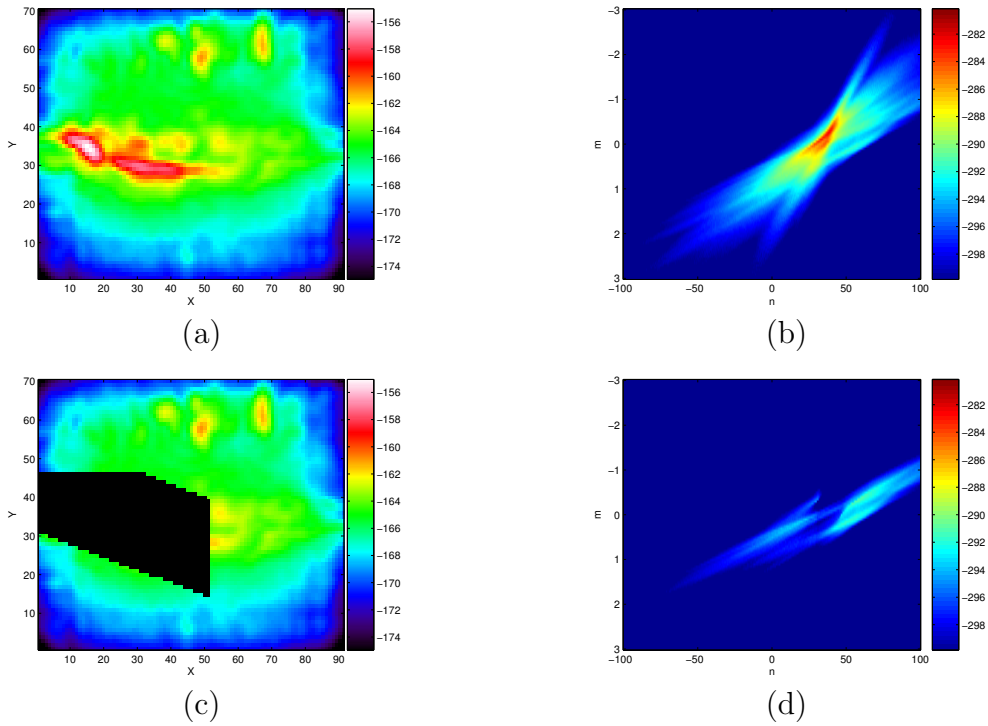

Figure 40: (a) Experimental GPR surface energy image, (b) HT of image in (a), (c) Iteration 2 Image, (d) HT of image in (c).

as circles in images [35], or hyperbolas and other parameterized curves [88, 54]. The HT has been successfully applied to detect buried linear features [51, 48], assuming that the buried object (e.g., a tunnel, or pipeline) is linear over the distance of interest. However, it is not reasonable to assume that buried objects are always linear over long distances, so the GHT fails to detect curving features when the actual curve parametrization is not known. The presented method in this section applies the HT with line parametrization, in (5), to smaller batches of an image and tries to estimate the curving structure from linear segments obtained from different batches.

Our problem can be stated as estimating a curving function $f(n)$ from partial linear approximations. An illustration of the problem and the approach taken are shown in Fig. 41. Assume we have an image of size $L \times L$ and the HT is applied on batches of size $M \times L$, where $M \ll L$. For batch i, if a line is detected in the

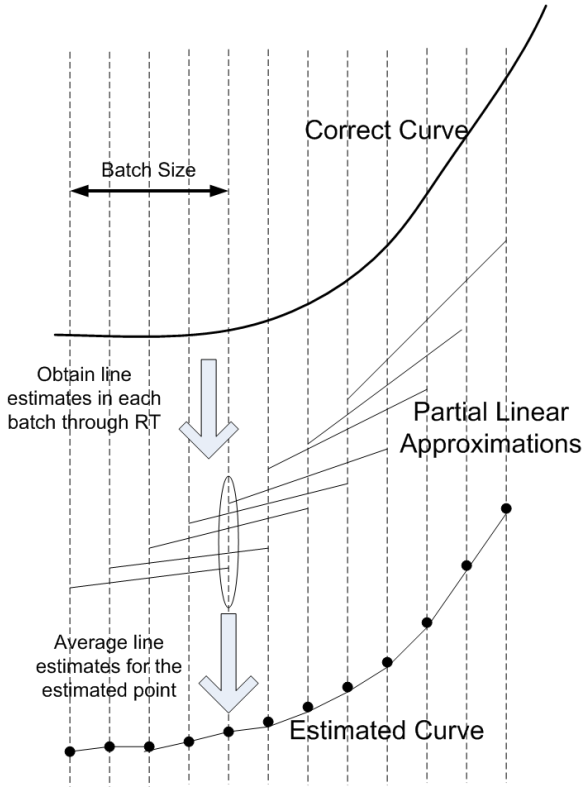

Figure 41: Estimating a curve from partial linear approximations

parameter domain a linear approximation is obtained as

$$\hat{f}_i(l) = m_i l + n_i, \tag{41}$$

where $i \leq l \leq i + M - 1$ for $i = 1, 2, 3, ...L - M + 1$ and (m_i, n_i) are the slope and intercept values of the detected line. In this way $L - M + 1$ linear approximations of the curving function $f(n)$ are obtained. These partial linear approximations can be seen in Fig. 41. For each point n the estimate can be found as the average of the linear approximations for that point:

$$\hat{f}(n) = \begin{cases} \frac{1}{n} \sum\limits_{k=1}^{n} \hat{f}_k(k) & n < M \\ \frac{1}{M} \sum\limits_{k=n-M+1}^{n} \hat{f}_k(k) & M \leq n \leq L - M \\ \frac{1}{L-n+1} \sum\limits_{k=n}^{L} \hat{f}_k(k) & n > L - M \end{cases} \tag{42}$$

There may be no line detections in some batches. This is not a problem since the estimator only uses the average of detected lines for estimating the position of curve at one point. For a curve to end, or not be detected, at least M consecutive batches should not have any line detections.

Selection of the batch size M is critical. On one hand, increasing M might decrease the advantage of coherent summation over lines if the tunnel is curving; on the other hand decreasing M might cause missed detections in Hough space because of the adding up of only a small number of signal values while not getting enough incoherent averaging of the noise. The optimal batch size should be selected to maximize the probability of detection (P_D) of a line in the batch [51]:

$$P_D = Q\left(Q^{-1}(P_{FA}) - \frac{\mu \min(M, R_S)}{\sqrt{M\sigma^2}}\right), \tag{43}$$

where μ is average signal value, σ^2 the noise variance and R_S the maximum Hough votes from the curving structure in the batch. The HT implementation finds the line with the most votes from the curve. Note that without discretization all lines are tangent to a curve at one point only. Most votes come from the lowest sloped part of the curve; in a second-order curve, $f(x) = ax^2+bx+c$, the number of Hough votes can be approximated as $R_S \approx \sqrt{(2/a)}$. The optimal batch size M should maximize (43). Since the Q-function gives the area in the tail of a Gaussian function and $Q^{-1}(P_{FA})$ is positive for all P_{FA}, an optimal M must satisfy

$$M^* = \arg\max_M \frac{\mu \min(M, R_S)}{\sqrt{M\sigma^2}} \quad \Rightarrow \quad M^* = R_S. \tag{44}$$

From (44) it can be seen that the optimal batch size should be equal to the maximum number of Hough votes, R_S. Since R_S depends on the curvature, a, this varies from curve to curve. However, an average value of the curvature can be selected for detecting the structure in images.

To test the proposed algorithm a tunnel described by the curve parametrization $y = 40 + 0.01(x - 100)^2$ at a depth of 20 cm is simulated. A two-layer model with

dry soil type is used. The system parameters are antenna height 10 cm, transmitter-receiver distance 10 cm, and antenna step size 2 cm (100 total steps are simulated). The tunnel is formed with point-like targets at each x position on the specified curve and depth. For the simulated tunnel response, a data cube is obtained. Clutter is assumed to be zero-mean additive white Gaussian noise (WGN). This clutter model is added to the raw tunnel data. The signal-to-noise ratio (SNR) is defined as the ratio of the maximum signal power in the image to the average noise variance. Figure 42 shows results from the HT (line parametrization) and the proposed partial Hough Transform (PHT) algorithm on a surface energy image.

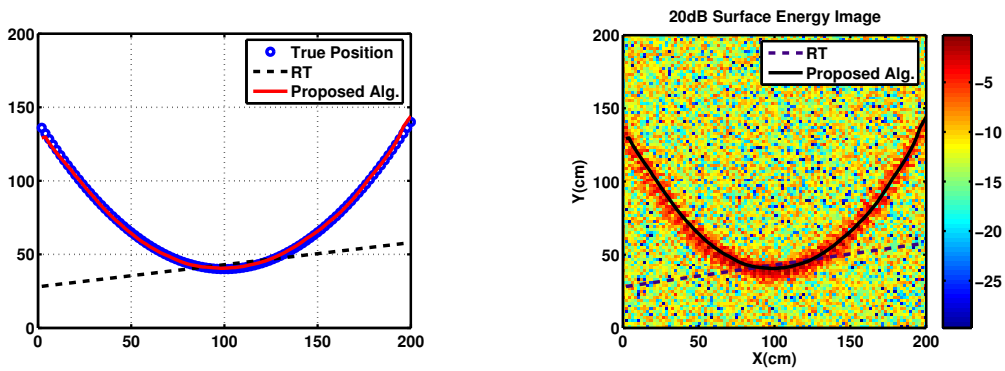

(a) (b)

Figure 42: (a) Processing results with HT and PHT detected for the noise-free case. (b) Detected structures for HT and PHT on a 20-dB surface energy image.

As seen in Fig. 42, the HT incorrectly finds a line nearly tangent to the curving structure, but the proposed algorithm finds the curve correctly. In the PHT algorithm, $M = 20$ is used as the batch size.

To compare the performance of the algorithm for varying parameters, a mean square error metric is defined as

$$\text{MSE} = \frac{1}{N}\sqrt{\sum_{n=1}^{N}(f(n) - \hat{f}(n))^2}, \tag{45}$$

where N is the total number of points. For the case in Fig. 42, the MSE for the HT and proposed algorithm are 31 cm and 0.88 cm, respectively.

Another simulation was performed to observe the effect of SNR and batch size. At each SNR and batch size, the algorithm is run and the MSE is computed. This procedure is repeated 100 times and the average MSE value is obtained for each SNR and M. The figure of merit 1/MSE is plotted in Fig. 43 for each SNR and M.

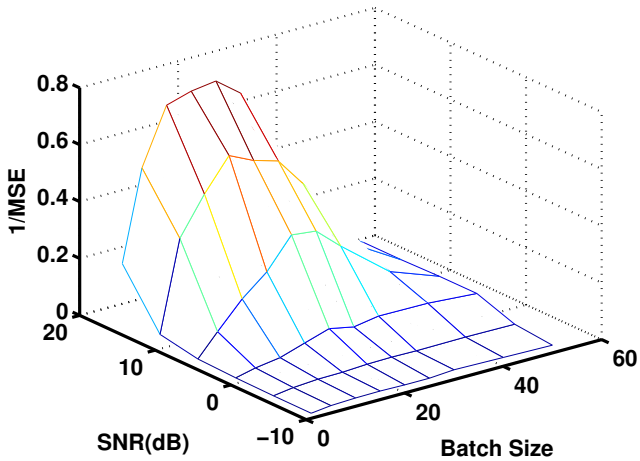

Figure 43: 1/MSE for varying SNR and batch size values.

From Fig. 43, it can be observed that there is an optimum batch size (i.e., 15–20) that gives better performance for nearly all SNR. This optimum batch size is also very close to the approximate Hough vote for the curvature, $R_S \approx \sqrt{(2/0.01)} \approx 14$. For low SNRs, the MSE increases for all batch sizes and the dependence on batch size is less important.

CHAPTER IV

DETECTING IMAGE FEATURES USING ADAPTIVE RANDOM SAMPLE THEORY

Feature detection is the extraction of necessary information about a feature from an image by means of signal processing tools. It is an important and broad topic extensively studied in areas like image processing [61, 28], computer vision [23, 61] and subsurface imaging [29, 89].

The Hough Transform (HT) [56], its variants and their generalizations [7, 35, 3, 61] are the most commonly used methods capable of detecting lines[35, 23], circles[3], or any other parameterized curve[88, 87]. The HT uses a parameterized model of each feature to transform the feature in the original image space into a single mesh point in the parameter space. The better a feature corresponds to the model, the more values (votes) will be accumulated at a mesh point. Features having votes above a predetermined threshold are selected as a detection.

Although the HT is effective even in very noisy images, it is not easily implementable because of its high computation time and large memory requirements. These problems are exacerbated as the dimension of the search space increases. For example, while the order of operations for detecting lines in 2D is $O(N^3)$, this increases to $O(N^5)$ for detecting lines in 3D images.

Various methods have been proposed to decrease the computation requirements of the HT, the primary ones being the Probabilistic Hough Transform (PHT) [67], the Randomized Hough Transform (RHT) [92, 91], and Line Detection using Random Sample Consensus(RANSAC) [38, 70, 21]. More detailed information about these methods are given in Chapter 1. Here we briefly review them.

The PHT uses only a randomly selected subset of edge points in the image as input for the HT; however, this technique leads to erroneous results for a small subset, and selection of the optimum subset size requires knowledge of the image. Although the latter problem is solved by the Progressive PHT (PPHT) algorithm, performance is still worse than the HT.

The RHT randomly selects n pixels, solves for the feature parameters and then increases the value of the parameter space cell by one. Using a many-to-one mapping and randomization saves on memory requirements as well as computation time. The RHT is suitable for low noise images [68]. For highly noisy images, the PHT outperforms the RHT, but neither algorithm works very well in detecting features in extremely noisy images.

The methods based on hierarchical division and pruning of the parameter space, like the fast HT (FHT) [69] or the Adaptive HT [60], recursively divide the parameter space into hypercubes and perform the HT only on the hypercubes with votes exceeding a selected threshold. More robust methods [77, 11] that propagate the error to the parameter space have also been developed. Although the existing hierarchical HT methods succeed in decreasing the computational load of the HT, they can only be applied to binary edge images.

To improve the robustness of feature detection, the RANSAC [38] algorithm was proposed. In RANSAC n edge points are randomly selected, and data lying within a defined distance from the line are classified as 'inliers' with the remaining data marked as 'outliers.' If the number of inliers is larger than a certain threshold, the feature parameters are re-estimated using only the inliers. In this way, the effect of misleading outliers is mitigated. Furthermore, the memory requirements are much less for the RANSAC algorithm since an accumulator array is not utilized. RANSAC has been shown to perform line detection faster than the HT [70]. Small improvements for increasing RANSAC's performance are proposed in [21, 20] for line detection problem.

Prior research has established an extensive basis for faster and robust feature detection. However, some of the existing methods can only be applied to binary images. The methods applicable to grayscale images have degraded performance compared to the HT. Our goal is to detect features in highly noisy grayscale images robustly and faster than the HT without the sacrificing performance. Our motivation is detection of buried linear structures, such as tunnels or pipes, in subsurface images generated from ground penetrating radar (GPR) or seismic sensor measurements. This is a problem of great interest in industrial/civil engineering and military applications and has been attacked by many researchers [89, 29, 82, 41]. Typically the presence of subsurface structures is visually masked in these images by noise and clutter, rendering their detection impossible without the implementation of feature detection algorithms. Adapting the subsurface images by binarization to existing methods using edge detection may seem like a viable solution, but in fact the loss of important data degrades the performance of the algorithm. Especially in high noise images it is even not possible to create edges since the features are completely hidden under severe noise.

The proposed adaptive ransom sample theory (ARST) method creates random hypothesis features and tests not only the selected feature, but also the region around it, to look for acceptable shapes. Contrary to choosing n random points to define a feature and solving for its parameters, the parameters are randomly selected from the parameter space distribution. The information obtained from each randomly selected feature is used to update this distribution, which reduces the total required number of random trials. The selected features are re-estimated within a smaller search space with a more accurate algorithm like the HT. Results show that this two-stage algorithm decreases the total computation time by limiting the search space over which the HT is performed to smaller spaces by randomly choosing probable areas without degrading the performance of the HT. The proposed algorithm is described

in Section 4.1. Simulated and experimental results from subsurface seismic and GPR images are given in Section 4.2.

4.1 Feature Detection by Adaptive Random Sample Theory

The basic idea of the adaptive random sample theory (ARST) algorithm is to first find rough areas or volumes in the image that possibly include features and then search only these rough regions with a more accurate algorithm like the HT. Reducing the search space of the HT decreases the computation time, while still maintaining detection performance at a level comparable to that of the full HT.

The feature to be detected is denoted by a set of parameters $P = (p_1, p_2, ..., p_n)$, where each parameter p_i has limits defined by R_i. For example, a line in 2D is denoted by two parameters, (ρ, θ), as $\rho = x\cos\theta + y\sin\theta$ and the ranges of these parameters are

$$\begin{aligned} R_\rho : &\quad -r_{max} < \rho < r_{max} \\ R_\theta : &\quad 0 < \theta < \pi \end{aligned} \tag{46}$$

where $r_{max} = \sqrt{s_x^2 + s_y^2}$ and s_x and s_y are the dimensions of the image. The line parametrization in 3D can be done by 4 parameters as described in Section 1.2.2 and [87]. A step by step description of the algorithm follows:

4.1.1 Algorithm Steps

The ARST method has two stages: the first stage searches for approximate candidate features, while the second stage refines the estimate of the features.

Stage I (Candidate Model Selection)

(i) Generate a candidate feature by randomly sampling the current parameter distribution F. Thus, $(p_1, p_2, ..., p_n) \sim F^k$ during iteration k. The parameter distribution F can be initialized as uniform over the parameter space. The randomly selected feature is denoted by $P = (p_1, p_2, ...p_n)$ and the parameters P make it possible to

instantiate the feature in the image.

In RANSAC and RHT, random features are selected by randomly choosing n edge points from the image and solving for the parameters $(p_1, p_2, ..., p_n)$. While this might be time efficient for binary images where edge points do not constitute a major part of the image, for gray-scale and higher dimensional images, this requires a significant amount of computation. Our method avoids these ineffiencies by directly sampling from the parameter space.

(ii) Calculate a feature indication metric C_S using the image data within a distance σ of the selected feature. For subsurface images the high reflected power from the subsurface targets is an indication of target presence, thus C_S is calculated by summing up the pixel values for the defined region. In this way, the algorithm is made robust against discretization errors or measurement errors within the region. For binary images C_S is the number of edge points within the distance σ, analogous to RANSAC's step in which the number of inliers within a distance of the selected line is counted. For road network extraction in SAR images, C_S can be calculated as in [22] where the road is darker than its neighbors and has smaller pixel values.

Figure 44(a) shows the strip summation region for the line with parameters (ρ, θ). All the lines with parameters $(\rho \pm \Delta\rho, \theta \pm \Delta\theta)$ as shown in Fig. 44(b) where

$$\Delta\theta = \arctan \frac{2(\sigma - \sigma^*)}{r_max} \quad \Delta\rho = \sigma^* \tag{47}$$

lies totally in the strip image region, where σ^* is shown in Fig. 44(b).

For small $\Delta\theta$, the shape in the parameter domain for the strip region becomes a diamond, where $\Delta\theta = \frac{2\sigma}{r_{max}}$ and $\Delta\rho = \sigma$. The small $\Delta\theta$ approximation also puts an upper bound on the σ parameter. For $\Delta\theta < \pi/6$, the $\sigma_{max} \cong r_{max}/4$. Selection of σ parameter effects the run time of the algorithm and optimally selecting it is discussed in Section 4.2.1.

(iii) If the feature indication metric C_S from Step (ii) is less than a threshold

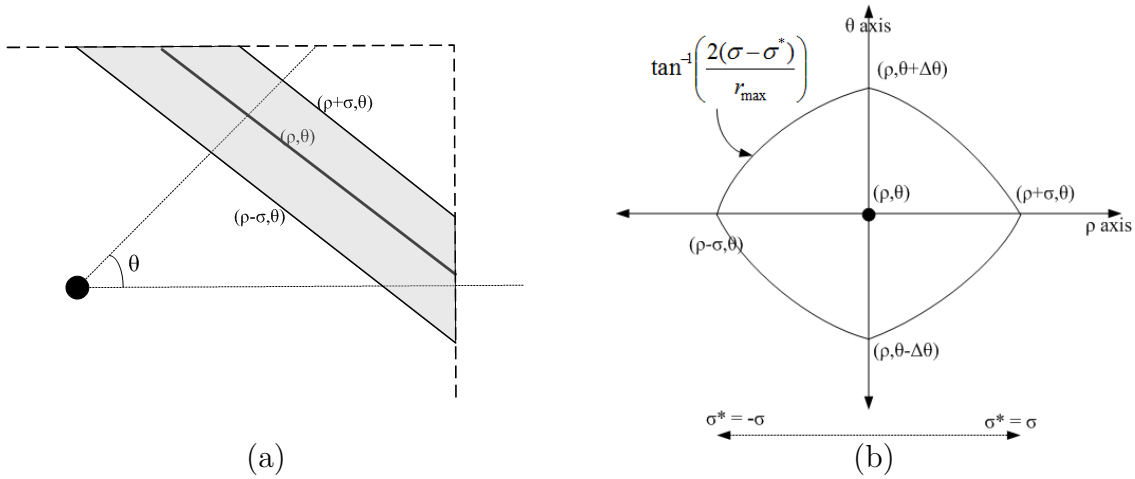

Figure 44: (a) Randomly selected strip region, (b) Parameter space corresponding to the strip region in (a).

T_s indicating that none of the features in the parameter space corresponding to the randomly selected strip region can be accepted as features; then the parameter space is updated as in Step (iv). If $C_S \geq T_s$ then the randomly selected (ρ, θ) is added to the candidate feature list (CFL) and the parameter space is again updated as in Step (iv). Increase iteration index k by 1.

(iv) Update the parameter distribution as follows

$$\begin{gathered} F^{k+1} = F^k \\ F^{k+1}(p_1 - \Delta p_1 : p_1 + \Delta p_1, ..., p_n - \Delta p_n : p_n + \Delta p_n) = 0 \\ F^{k+1} = \frac{F^{k+1}}{\sum F^{k+1}} \end{gathered} \tag{48}$$

In (48) F^k is the parameter distribution at the kth iteration. The initial distribution is selected as uniform over the parameter range if there is no *a priori* knowledge of the possible features. After updating the parameter distribution, increment k and go to Step (ii).

(iv) Stop after k_{max} trials.

Stage II (Refine The Estimate) For each candidate feature in the CFL, the search space for the ith candidate is defined as $S_i = (p_{i,1} - \Delta p_{i,1} : p_{i,1} + \Delta p_{i,1}, ..., p_{i,n} -$

$\Delta p_{i,n} : p_{i,n} + \Delta p_{i,n})$. Apply the HT only over S_i to find a better estimate of the features in that region. Note that this stage also enables multiple features within a region to be resolved and successfully detected. For example, if two lines are close to each other Stage I selects only one random feature in that region. To the extent that the HT can resolve multiple features, all can be detected.

4.1.2 Selection of Algorithm Parameters

Selection of the parameter σ is important because it determines the number of trials, k_{max}, and the search space, $\Delta(p_1, ..., p_n)$, in Stage II. The relative size of σ with respect to the size of the image, r_{max}, is a crucial parameter. Selecting a very small σ/r_{max} ratio will increase k_{max} and reduce $\Delta(p_1, ..., p_n)$. In the limit $\sigma \to 0$, the algorithm approaches the RHT. Conversely, when the ratio σ/r_{max} increases, $\Delta(p_1, ..., p_n)$ will increase, while the value of k_{max} will decrease. In the limit $\sigma \to r_{max}$, the number of trials in Stage I will be 1, making the candidate model selection stage useless and reducing the proposed method to the HT applied in Stage II to the whole image.

Once σ/r_{max} is selected, $\Delta(p_1, ..., p_n)$ can be computed as follows.

$$\begin{array}{cc} \text{2D Line Detection} & \text{3D Line Detection} \\ \\ \Delta\theta = \arctan\frac{2\sigma}{r_{max}} & \Delta\theta = \arctan\frac{2\sigma}{r_{max}} \\ \Delta\rho = \sigma & \Delta\phi = \arctan\frac{2\sigma}{r_{max}} \\ & \Delta u = \sigma \\ & \Delta v = \sigma \end{array} \tag{49}$$

Let k_{max} be the number of trials required to have at least one feature within the $\Delta(p_1, ..., p_n)$ vicinity of the true feature parameter with probability q. If the selected parameters fall beyond $\Delta(p_1, ..., p_n)$, the feature cannot be correctly detected since

Stage II only searches for features within $\Delta(p_1, ..., p_n)$ of the selected feature parameters. If a non-adaptive scheme is used and parameters are randomly chosen from a uniform distribution the probability that all selections are outside of the $\Delta(p_1, ..., p_n)$ vicinity after k_{max} trial is

$$1 - q = \left(\frac{\prod_{i=1}^{n} R(p_i) - 2^n \prod_{i=1}^{n} \Delta p_i}{\prod_{i=1}^{n} R(p_i)} \right)^{k_{max}} \tag{50}$$

In (50) n denotes the number of parameters representing the feature. Thus $n = 2$ for a line in 2D and $n = 4$ for a line in 3D. Also, $R(p_i)$ denotes the range of the parameter p_i. From (50) the number of trials for picking a random feature within $\Delta(p_1, ..., p_n)$ with probability q is

$$k_{max} = \frac{\log(1 - q)}{\log \left(\frac{\prod_{i=1}^{n} R(p_i) - 2^n \prod_{i=1}^{n} \Delta p_i}{\prod_{i=1}^{n} R(p_i)} \right)} \tag{51}$$

In the adaptive selection of parameters, at each trial part of the distribution of size $\Delta p_1 \times \Delta p_2 ... \Delta p_n$ is taken out. The probability $1-q$, which is equal to not getting any random selection in the $\Delta(p_1, ..., p_n)$ vicinity of the true feature parameter in k_{max} trials, can be given as

$$1 - q = \frac{\prod_{\ell=1}^{n} |\mathcal{R}_\ell| - k_{\max} 2^n \prod_{\ell=1}^{n} \Delta p_\ell}{\prod_{\ell=1}^{n} |\mathcal{R}_\ell|}. \tag{52}$$

As an example, consider a 2D image of size 100×100. Using a resolution of 1 in ρ and 1° in θ results in 50912 line summations for HT. If $\sigma = 10$ is selected, then from (49) $\Delta\rho = 10$ and $\Delta\theta = 8^\circ$. A detection probability of $q = 0.99$ requires a minimum of only 157 strip summations for Stage I, while Stage II requires to make 320 line summations for the selected $\mathcal{S}_i$. In total the computational load of HT is decreased and results indicating this are given in section 4.2.1 and 4.2.2.

Selection of the optimal threshold T_s is a hard problem. Depending on the image type, the accepted feature criteria and knowledge of the image statistics, a suboptimal

T_s can be selected. For the problem of feature detection in subsurface images, the noise statistics (μ_n, σ_n^2) of the image would have to be estimated from the image itself. The feature detection of an SNR level greater than m_{SNR} would use a threshold T_s that should be selected as

$$T_s = m_{\text{SNR}} \sigma_n^2 s_i + N_{\text{pix}} \mu_n \tag{53}$$

where N_{pix} is the number of pixel points added in the summation region of the selected feature.

4.2 Results

To illustrate how the proposed algorithm works, a 101×101 image with two linear structures having the parameter values $\rho_1 = 70$, $\theta_1 = 65°$ and $\rho_2 = 20$, $\theta_2 = 120°$ is created. The image is shown in Fig. 45(a). Zero-mean white Gaussian random noise (WGN) is added to the image with signal-to-noise ratio (SNR) of 0 dB . Figure 45(b) shows the synthetic linear structures with noise added. Note that the linear features cannot be visually seen and are masked by the noise.

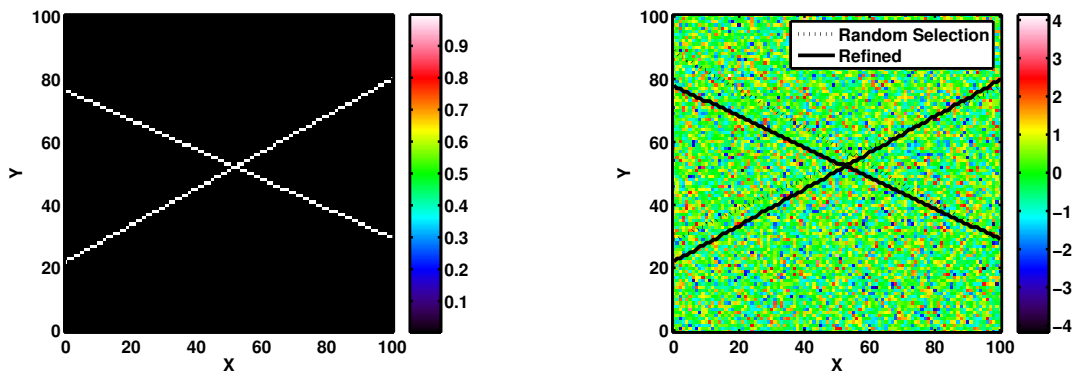

(a) Lines (b) Lines + noise

Figure 45: (a) Two Linear features, (b) Detected lines from Stage I (random selection) and Stage II (refined by the HT) of the proposed algorithm on the noisy image of SNR 0 dB.

The distance parameter σ is chosen as 10. Number of random trials, k_{max}, is calculated using (52). The candidate features obtained from Stage I of the algorithm

are shown in Fig. 45(b) with dashed lines. These candidate features are refined in Stage II by applying the HT within a vicinity $(\Delta\rho, \Delta\theta)$ of the parameters of the selected lines as pictured in Fig. 44(b). The refined lines are shown by solid lines in Fig. 45(b). The true parameters with the ones obtained from stage I and stage II of the algorithm are listed in Table 6.

Table 6: True and Detected Target Parameters

2D Line Detection Results				
Targets	Target 1		Target 2	
Parameters	ρ	$\theta(^o)$	ρ	$\theta(^o)$
True Parameters	70	65	20	120
Random Selection	76	59	27	116
Refined by HT	70	64	19	120

4.2.1 Performance of the algorithm for different σ values:

The parameter σ, as discussed in Section 4.1.2, determines the other algorithm parameters like k_{max} and $\Delta(p_1, ..., p_n)$. In this section we analyze the effect of σ on the run time of the algorithm using a Monte-Carlo simulation and select the σ that minimizes the total run time. A 2D image of size 100×100 containing a linear structure with parameters $(\rho, \theta) = (70, 65°)$ with SNR $= 10\,\text{dB}$ is generated.

For various σ values, the algorithm was run 100 times and the elapsed times for Stage I and II were recorded. Increasing σ will decrease the number of trials by (52). Although (52) is not a closed form expression it can be seen from number of trials for the nonadaptive case (51) that the time for Stage I of the algorithm decreases logarithmically with σ. This can also be observed in Fig. 46(a) where the average run time for Stage I of the algorithm obtained from the simulations is shown.

The parameter space defined in (49) searched by HT in Stage II of the algorithm increases quadratically with σ. This indicates a quadratically increasing run time as observed in Fig. 46(b). Note that this quadratic increase is for only line detection in

2D images. From (49) it can also be observed that for 3D images the search space increases with as σ^4.

The combination of these two effects yields the total average run time shown in Fig. 46(c). For the total run time of the algorithm a σ/s_i value that minimizes the average run time can be found, and $\sigma/s_i = 0.1$ is selected as the optimum parameter for line detection in 2D images.

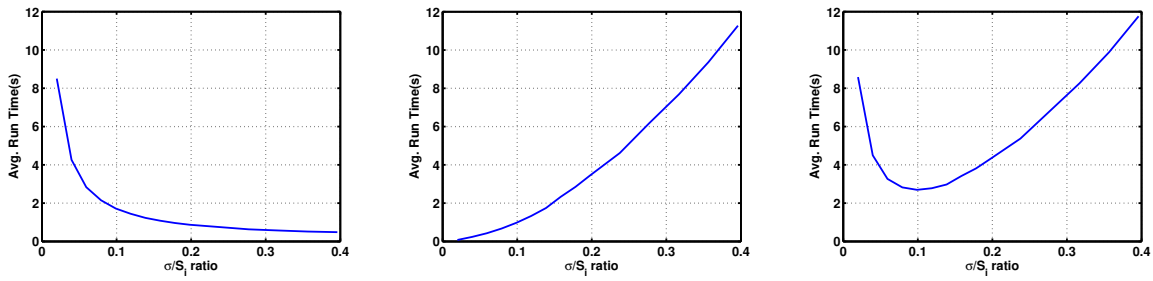

(a) (b) (c)

Figure 46: (a) Average run time of stage I of the algorithm versus σ/s_i where s_i is the size of the image and 100 for this simulation. (b) Average run time of stage II of the algorithm, (c) Total average run time of the algorithm.

4.2.2 Performance of the proposed method for varying SNR

The detection performance and average running time of the presented ARST algorithm for varying levels of SNR are now compared to the HT, RHT and PHT for 2D images. Two versions of the RHT and PHT algorithms with low (RHTL, PHTL) and high (RHTH, PHTH) number of trials and data percentage are used for comparison.

At each SNR value, all the algorithms are run 100 times with random noise added to the original signal each time. The detected target parameters and the run time of the algorithms are noted. To fairly compare the detection performance and the run times for all algorithms, the same parameter resolution is used. That is, $r_\rho = 1$ and $r_\theta = 2°$. The ARST algorithm uses a $\sigma/s_i = 0.1$ ratio. The PHT uses 50% and 5% of the data for the PHTH and PHTL results; RHT uses 10^5 and 10^4 random point selections for RHTH and RHTL, respectively.

Table 7: Average Run Times (secs) of the Algorithms in 2D

ARST	HT	RHTH	RHTL	PHTH	PHTL
1.72	16.13	4.47	0.44	7.75	0.77

The probability of detection (P_D) for all algorithms is shown in Fig. 47. Figure 47

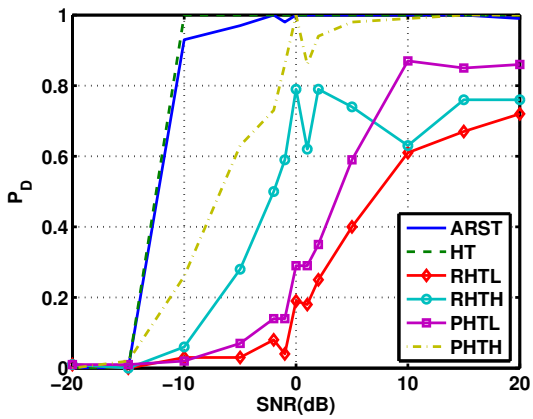

Figure 47: Probability of detection (P_D) vs. SNR for the compared feature detection algorithms.

shows that the ARST and the HT have nearly the same performance for all SNR values while the PHT and RHT algorithms have much lower P_D. Here the advantage of the ARST lies in the average run time. The average run times of the algorithms are given in Table 7. It can be seen that while the ARST has the same performance level as the HT, the average run time is nearly ten times less than the HT. The algorithms RHTL and PHTL can run faster than the proposed ARST method, but they have much worse detection performance. Even the PHTH and RHTH algorithms which have higher average run times than ARST have worse detection performance. So the proposed method combines the fast running time of a random selection method with the best possible detection performance of the HT.

4.2.3 Experimental Data Results in 3D

To investigate the potential for new feature detection algorithms an experimental setup using co-located GPR and seismic sensor was built [82, 83]. Two different

experimental scenarios have been investigated with scale models of linear structures as shown in Fig.48. More detail about the tunnel experiments is given in Chapter 3.1.4.

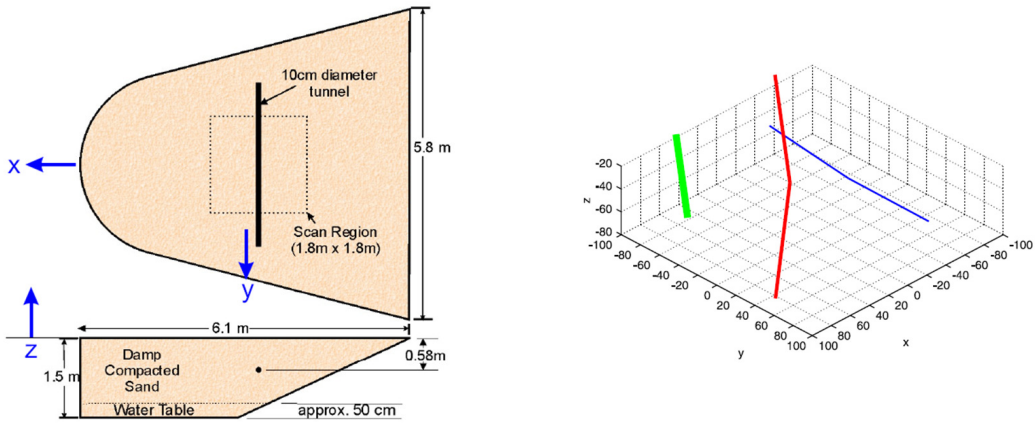

(a) (b)

Figure 48: (a) Model of the sand tank with one 4" tunnel buried approx 58 to 60 cm deep from the surface. (b) Layout of the three buried PCV pipes. The targets are a 2" pipe buried approx 30 cm deep, a 1" pipe buried diagonally from the surface down to 60 cm, and a 0.5" pipe buried approx 60 cm deep. The coordinates of the axes are the same as the coordinates in (a).

For both scenarios Fig. 49 shows the isosurface images for the backprojected subsurface GPR sensor data [25]. Both HT and the ARST algorithms are applied to the 3D subsurface images. A resolution of 2° for (θ, ϕ) and 0.02 m for u and v are used for both algorithms. The proposed method used $\sigma = 0.15$ m. The detected lines for both algorithms are shown in Fig. 49 . The detected line parameters and the total run times of the algorithms are listed in Table 8. It can be observed that the ARST method can find the buried features much faster but as accurately as HT.

Table 8: Experimental Results with 3-D Data Comparing the ARST to the HT

Sensors	Scenario 1		Scenario 2	
Algorithms	ARST	HT	ARST	HT
$\theta\,(^\circ)$	96.68	96	(40.1, 44.5 ,86.7)	(40, 45, 85)
$\phi\,(^\circ)$	0.08	0	(-4.4, 8.7, -1.3)	(-3,9,0)
u	0.162	0.15	(-85.2, -16.71, 55.99)	(-80, -16, 56)
v	0.620	0.62	(35.28, 35.79, 65.22)	(32, 36, 64)
Time (s)	1.44×10^3	5.74×10^4	1.78×10^3	5.79×10^4

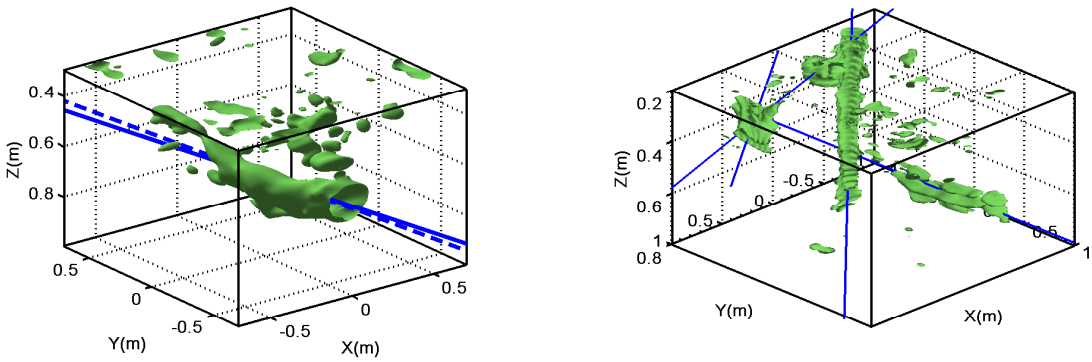

(a) (b)

Figure 49: (a) 3D iso-figures at -15 dB of the 4" tunnel using the GPR sensor measurements. Dashed and solid lines show the detected lines for HT and ARST method respectively.

CHAPTER V

COMPRESSIVE SENSING OF PARAMETERIZED SHAPES

The problem of detecting parameterized shapes, e.g., lines or circles, arises in many diverse areas of image processing, computer vision and pattern recognition. As explained in Chapter 1, the Hough Transform (HT) [56] and Generalized Hough Transform (GHT) [88] are well-known methods to detect lines and other parameterized shapes in an image. Both transforms convert the problem of finding spatially spread patterns in the image space into detecting (sparse) peaks in the parameter space. In other words, the GHT is a sparse representation of the shapes in an image.

We have shown in Chapter 2 that using the ideas from compressive sensing (CS) a sparse signal can be constructed from a small number of "random" projections. In this section, we show that the parameterized shapes in an image can be found from only a small number of random projections of a gray scale image. For example, a new camera architecture that directly acquires random projections of an image without collecting every pixel has been demonstrated [36]. In standard CS techniques [13] the compressive measurements of the image are used to create the image itself using an assumption of the image is sparse in the wavelet domain or some other domain [36]. We show in Section 5.1 that the random projections of an image,e.g., acquired by a camera [36] could be used to form the sparse GHT representation of an image. We also show that it is possible to detect a variety of shapes such as lines, circles etc. jointly using the same CS framework along with an overcomplete representation of the shapes.

Standard techniques for detecting parameterized underground structures like pipes

or tunnels usually involve two stages. First, the raw data collected by a sensor such as a Ground Penetrating Radar (GPR) is inverted to form an image of the subsurface area (See Chapters 1 and 2 for different imaging methods). Second, the image is searched for parameterized shapes like lines using an algorithm such as the GHT. The application of the CS idea to this problem is not immediately apparent since it would seem to require the formation of a 3D subsurface image using the data collected from the probing sensor, followed by random projections of the 3D image. In the second part of this chapter we exploit the sparsity of shapes in the parameter domain and combine the image formation and feature detection steps using the CS framework to find the shape parameters directly from the raw sensor measurements. In addition to skipping the image formation step, the CS processing can be done with a minimal number of raw sensor measurements. The utility of this CS-based method is demonstrated for finding buried linear structures in both simulated and experimental GPR data.

5.1 Shape Detection using Compressive Sensing

The GHT can be written as

$$\mathcal{R}(\boldsymbol{\pi})[f(x,y)] = \int f(\varphi_x(\xi,\boldsymbol{\pi}),\varphi_y(\xi,\boldsymbol{\pi}))d\xi \tag{54}$$

where $\boldsymbol{\pi}$ is an p-dimensional vector defining the curve parameters and $\varphi_x(\xi,\boldsymbol{\pi})$ and $\varphi_y(\xi,\boldsymbol{\pi})$ are functions that define the specific curve. The GHT transforms from the 2D (x,y) image space to the p-D parameter space defined by $\boldsymbol{\pi}$.

In order to express the image in terms of an overcomplete dictionary of possible shapes, we must discretize the parameter vector $\boldsymbol{\pi}$ along each of its p dimensions. Then we can enumerate a finite set of possible parameter vectors $\mathcal{P} = \{\boldsymbol{\pi}_1,\boldsymbol{\pi}_2,\ldots,\boldsymbol{\pi}_N\}$, where N depends on the discretization that we pick. Finally, we define the vector $\boldsymbol{p}$ to be an indicator and weight function, i.e., the kth element of $\boldsymbol{p}$ is nonzero if we want to select (and weight) parameter $\boldsymbol{\pi}_k$.

Now we are ready to create the overcomplete dictionary by using the inverse relation between the parameter space selector $\boldsymbol{p}$ and the image $\boldsymbol{f}$, which can be written as

$$\boldsymbol{f} = \boldsymbol{H}\boldsymbol{p} \tag{55}$$

where $\boldsymbol{H}$ is, in some sense, an inverse GHT operator. The $L \times L$ image must be concatenated into a length-L^2 vector $\boldsymbol{f}$. Each column of $\boldsymbol{H}$ is one possible parameterized shape in the image domain, i.e., the kth column of $\boldsymbol{H}$ corresponds to the shape with parameters $\boldsymbol{\pi}_k$. The matrix $\boldsymbol{H}$ is called the sparsity basis because we can represent the image using a small number of columns from $\boldsymbol{H}$. We say that the image is K-sparse if its GHT has no more than K nonzero peaks, or, equivalently, the vector $\boldsymbol{p}$ has no more than nonzero elements.

Consider our K-sparse signal $\boldsymbol{p}$ of length N as our parameter space signal where the image $\boldsymbol{f}$ is represented as in (55). In CS rather than sampling all the pixels in the image $\boldsymbol{f}$ we measure linear projections of $\boldsymbol{f}$ into a second set of basis vectors $\boldsymbol{\phi}_m,\ m = 1, 2, ...M$. Here many fewer samples than the size of $\boldsymbol{p}$ are taken, $M \ll N$. In matrix notation we measure

$$\boldsymbol{y} = \boldsymbol{\Phi}\boldsymbol{f} = \boldsymbol{\Phi}\boldsymbol{H}\boldsymbol{p} \tag{56}$$

Here $\boldsymbol{y}$ is the only information we have about the image. The result of CS theory is that the sparse parameter domain signal $\boldsymbol{p}$ can be recovered exactly from

$$M = C\left(\mu^2(\boldsymbol{\Phi}, \boldsymbol{H}) \log N\right) K \tag{57}$$

CS measurements $\boldsymbol{y}$ by solving an ℓ_1 minimization problem as

$$\hat{\boldsymbol{p}} = \operatorname{argmin} \|\boldsymbol{p}\|_1 \qquad s.t. \quad \boldsymbol{y} = \boldsymbol{\Phi}\boldsymbol{H}\boldsymbol{p} \tag{58}$$

with overwhelming probability [15], where $\mu(\boldsymbol{\Phi}, \boldsymbol{H})$ is the coherence between $\boldsymbol{\Phi}$ and $\boldsymbol{H}$ defined as in [15]

The optimization problem in (58) is valid for the noiseless case. For noisy images, the compressive measurements will be in the form

$$\boldsymbol{y} = \boldsymbol{A}\boldsymbol{p} + \boldsymbol{z} \qquad \boldsymbol{z}_k \sim \mathcal{N}(0, \sigma^2) \tag{59}$$

where $\boldsymbol{A} = \boldsymbol{\Phi}\boldsymbol{H}$. It is shown in [12, 14, 55, 34] that instead of (58) relaxed convex optimization problems as

$$\min \|\boldsymbol{p}\|_1 \qquad s.t. \quad \|\boldsymbol{A}^T(\boldsymbol{y} - \boldsymbol{A}\boldsymbol{p})\|_\infty < \epsilon_1 \tag{60}$$

or

$$\min \|\boldsymbol{p}\|_1 \qquad s.t. \quad \|\boldsymbol{y} - \boldsymbol{A}\boldsymbol{p}\|_2 < \epsilon_2 \tag{61}$$

will result in the sparsest parameter domain $\boldsymbol{p}$, allowing errors between the measurements and our model.

The optimization problems in (58) and (60) can be solved by linear programming techniques, while (61) is a second-order cone program. Since all of these minimize convex functionals, a global optimum is guaranteed.

5.1.1 Selection of Algorithm Parameters

Selection of the grid density N in the parameter space, as well as the regularization parameter $\epsilon_{1,2}$ used in (60) and (61), is very important. Our shape parameter estimates are confined to the selected grid. While increasing N makes the grid uniformly very fine, it also increases the complexity of the algorithm. Our method is suitable for multiresolution grid refinement. Initially a coarse grid might be used to obtain an approximate knowledge of possible target locations. Later the grid can be made finer around regions of interest where better precision is required. Using a very coarse grid that wouldn't represent the possible shapes in the image would introduce substantial bias to the parameter estimates.

The regularization parameter controls the tradeoff between the sparsity of the solution and how well the solution fits the data. When the noise statistics of the data

are known, a "good" choice of ϵ can be made, e.g., for additive white Gaussian noise (WGN) with variance σ^2, selecting $\epsilon = \sqrt{2 \log N}\sigma$ makes the true $\boldsymbol{b}$ feasible with high probability [14]. When the noise statistics are unknown ϵ can also be selected using cross-validation (CV) [8] as discussed in Chapter 2.

5.1.2 Detecting Linear Structures

An important application of shape detection is detecting linear structures in images. Figure 50(b) shows a noisy gray-scale image with 3 lines having the parameters $\rho = [-3, 21, -27]$ and $\theta = [33, 132, 153]$ degrees. The true lines are given in Fig. 50(a). The image is 50×50, i.e., 2500 pixel values. For detecting lines in the image only 400 projections (compressive samples) of the image with random Gaussian vectors are used. The compressive samples, $\boldsymbol{y}$, of the noisy image are shown in Fig. 50(c). We assume that these samples are the only information we have about the image and our goal is to find the linear structures in the image. One possible reconstruction is

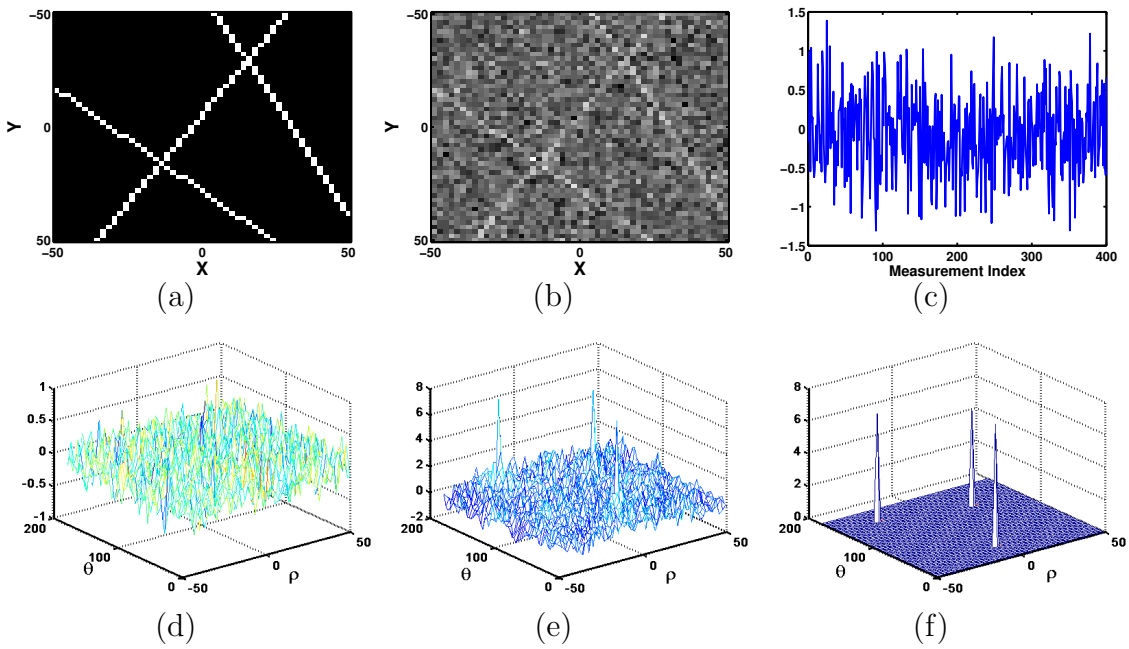

Figure 50: (a) Image showing true line locations, (b) Noisy image with additive white Gaussian noise ($\sigma = 0.5$), (c) Compressive measurements, (d) Parameter space image obtained with ℓ_2-norm minimization, (e) Hough Transform using all the image pixels, (f) ℓ_1-minimization using the Dantzig Selector.

to find the parameter space image which has minimum ℓ_2-norm and also satisfies the compressive measurements.

The result is the parameter space image shown in Fig. 50(d). This solution is a feasible solution because it satisfies the constraint $\boldsymbol{y} = \boldsymbol{A}\boldsymbol{p}$, but this parameter space image doesn't give any reliable information about possible line locations.

If the problem stated in (60) is solved, the parameter space image shown in Fig. 50(f) is obtained. It can be seen that the resultant image is sparse with 3 peaks corresponding to the true line parameters. If we had the entire image and had applied the standard Hough transform to the original image we would obtain the image in Fig. 50(e). Even though the Hough transform image shows 3 significant peaks, it is more noisy, and it requires L^2 measurements (i.e., all the pixels in the image).

5.1.3 Joint Detection of Circles and Lines

The standard Hough Transform calculates the votes for each parameter space value. To detect circles in an image, a HT with circle parametrization should be taken and the peaks in the parameter space should be searched. The same procedure should be repeated for the same image for detecting lines by creating a separate parameter space using line parametrization. Having different shapes in the image might be problematic since line pixels will contribute votes for circle parameters or vice versa.

The CS shape detection algorithm can also be applied as two separate problems; one for line and the other for circle detection. These two separate problems are shown in Fig. 51.

Instead of solving two separate problems, a joint problem combining the line and circle dictionaries can be solved. The joint problem is illustrated in Fig. 51. We can relate the image f to the parameter space of lines and circles by using an overcomplete

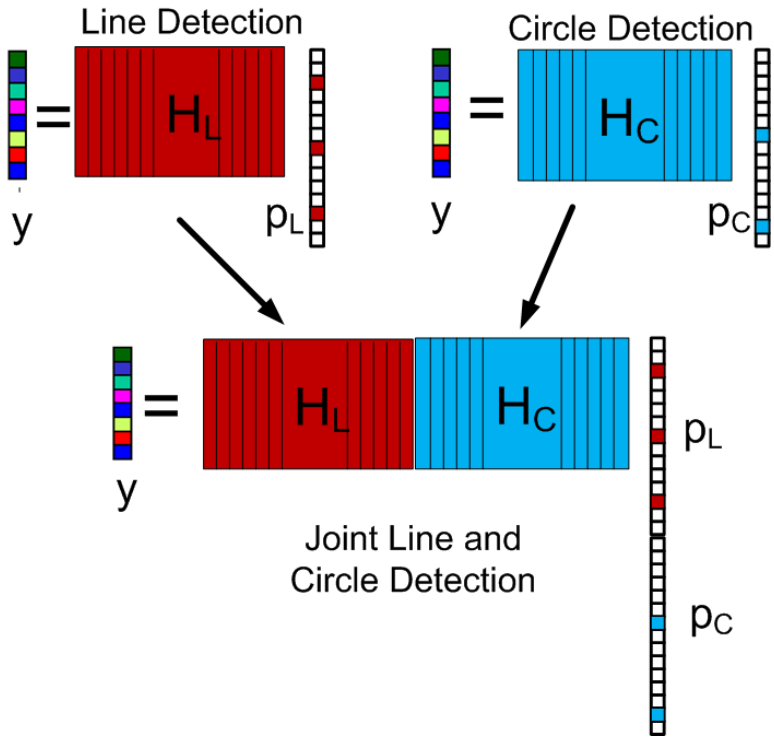

Figure 51: Joint Line and Circle Detection

dictionary of shapes.

$$\boldsymbol{f} = \begin{bmatrix} \boldsymbol{H}_l & \boldsymbol{H}_c \end{bmatrix} \begin{bmatrix} \boldsymbol{p}_l \\ \boldsymbol{p}_c \end{bmatrix} \quad \Rightarrow \boldsymbol{y} = \boldsymbol{\Phi} \boldsymbol{f} \tag{62}$$

where $\boldsymbol{H}_l$ and $\boldsymbol{H}_c$ are the sparsity bases and $\boldsymbol{p}_l$ and $\boldsymbol{p}_c$ are the parameter spaces for line and circle respectively. The sparse parameter space $(\boldsymbol{p}_l\, \boldsymbol{p}_c)$ can be reconstructed from compressive measurements $\boldsymbol{y}$ using one of the convex optimization problems presented in Section 5.1. Note that our measurements $\boldsymbol{y}$ don't change with the kind of problem we are solving. The same measurements can also be used to get different information about the image. Any better representation or dictionary can be used to get better feature detection results using the same measurements. In other words, they are future proof.

Figure 52 shows a noisy gray-scale image containing two circles with centers at $(10, -6)$ and $(-18, 4)$ and radii 22 and 28, respectively, and two lines with parameters

$\rho = [-3, 21]$ and $\theta = [33, 132]$. Only 500 compressive measurements are used. The joint optimization problem is solved using (67) and the resultant joint parameter space is shown in Fig. 52(d). The first two peaks in the resultant parameter space correspond to the two lines in the image, and the last two peaks are represents the two circles.

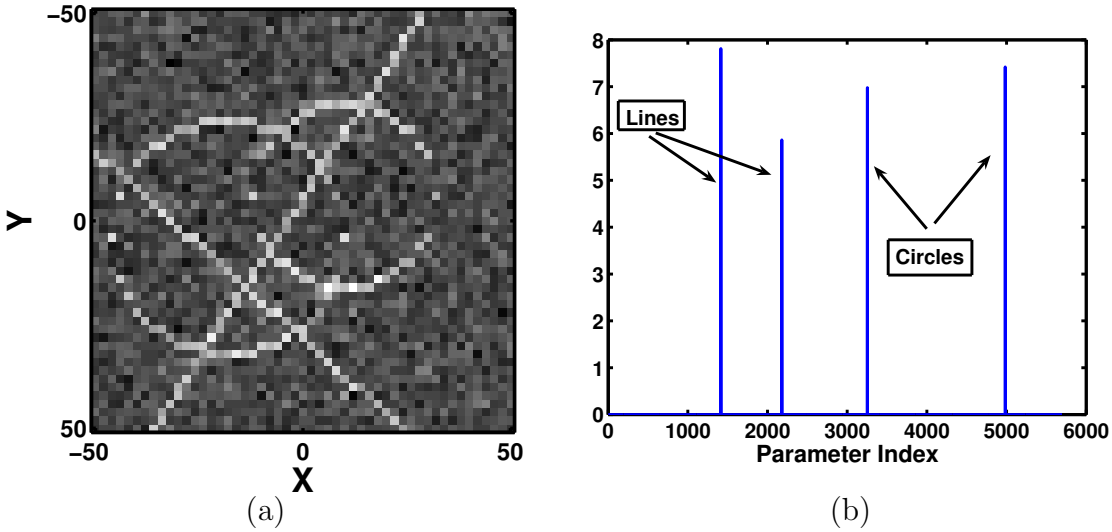

Figure 52: (a) Noisy image with additive white Gaussian noise ($\sigma = 0.2$), (b) Results from ℓ_1-minimization of the Dantzig Selector.

5.1.4 Performance in Noise

To analyze the performance of the CS shape detection with varying noise levels, the algorithm is applied to images with SNRs from $-25\,\text{dB}$ to $10\,\text{dB}$. At each SNR level one random linear structure is corrupted by WGN with zero mean and corresponding variance. Parameters of the linear structure are found using (67). This procedure is repeated 50 times with random initialization of the noise at each time and correct detections are counted. The detection ratio vs. SNR plot for different compressive measurements is shown in Fig. 53(a).

It can be observed that proposed algorithm detects shapes in very noisy images using a small number of measurements and increasing the number of measurements increases the detection ratio for the same SNR value.

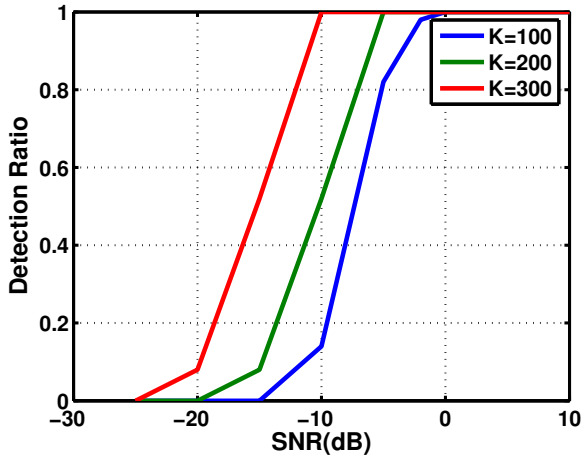

Figure 53: Detection ratio vs. SNR. K is the number of random projections.

5.1.5 Test on Number of Compressive Measurements

For exact recovery of K-sparse signals the required number of compressive measurements is given by (57). This quantity depends on the mutual coherence between the sparsity basis and the random projection matrix used. Here three different types of random matrices are tested (see Fig. 54). The entries of the Type I random matrix are drawn from $\mathcal{N}(0,1)$. The Type II random matrix has random ± 1 entries with probability of $1/2$, and the Type III random matrix is constructed by randomly selecting some rows of an identity matrix of size N which amounts to measuring random pixels of the image at each measurement. Each matrix is normalized to have unit norm rows.

The average mutual coherence between the random matrices and the sparsity basis for a line are $\mu_1 = 5.2751$, $\mu_2 = 5.0059$ and $\mu_3 = 12.7500$ for Type I, II and III random matrices, respectively. This means that the required number of compressive measurements to detect a shape will be similar if Type I or II matrices are used. Using Type III matrix will require approximately 6.5 times more compressive measurements for the same detection capability.

A Monte-Carlo simulation is done to test the required number of compressive measurements for each random matrix type. Each random matrix is tested with 1,

2 and 3 shapes in the image. Figure 54 shows the detection ratio versus the number measurements.

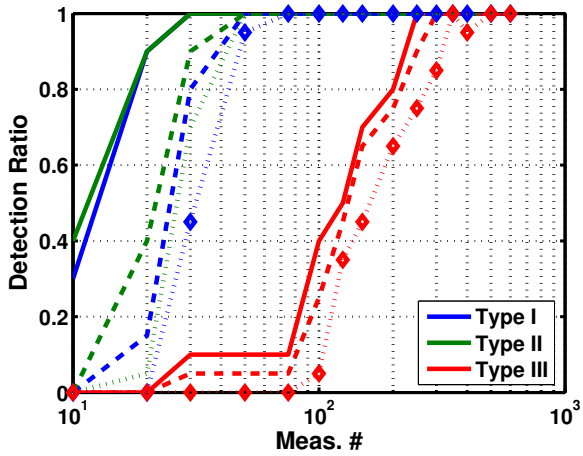

Figure 54: Detection ratio vs. measurement number for varying types of random matrices (Solid, dashed and diamond marked dotted lines correspond to 1, 2, and 3 targets respectively).

It can be observed that the required number of compressive measurements increases for all types of random matrices when used with an increasing number of targets. While Type I and II random matrices require similar numbers of measurements, Type III random matrices require many more measurements to detect the same number of targets as expected from the mutual coherence values given above.

5.1.6 Detecting Buried Pipes in Seismic or GPR Images

We applied the CS shape detection to the problem of finding linear structures in GPR or seismic images. Since the algorithm uses random projections of the images, the sensor data is first inverted to create an image of the subsurface. Although the CS shape detection idea can be extended to 3D images, for now only results for 2D images are generated. Figure 55(a) shows a backprojected seismic surface energy image taken over a single buried pipe [82] (See Section 4.2.3). The standard HT of the image is shown in Fig. 55(b). The two peaks in Hough domain correspond to the two linear structures in the image.

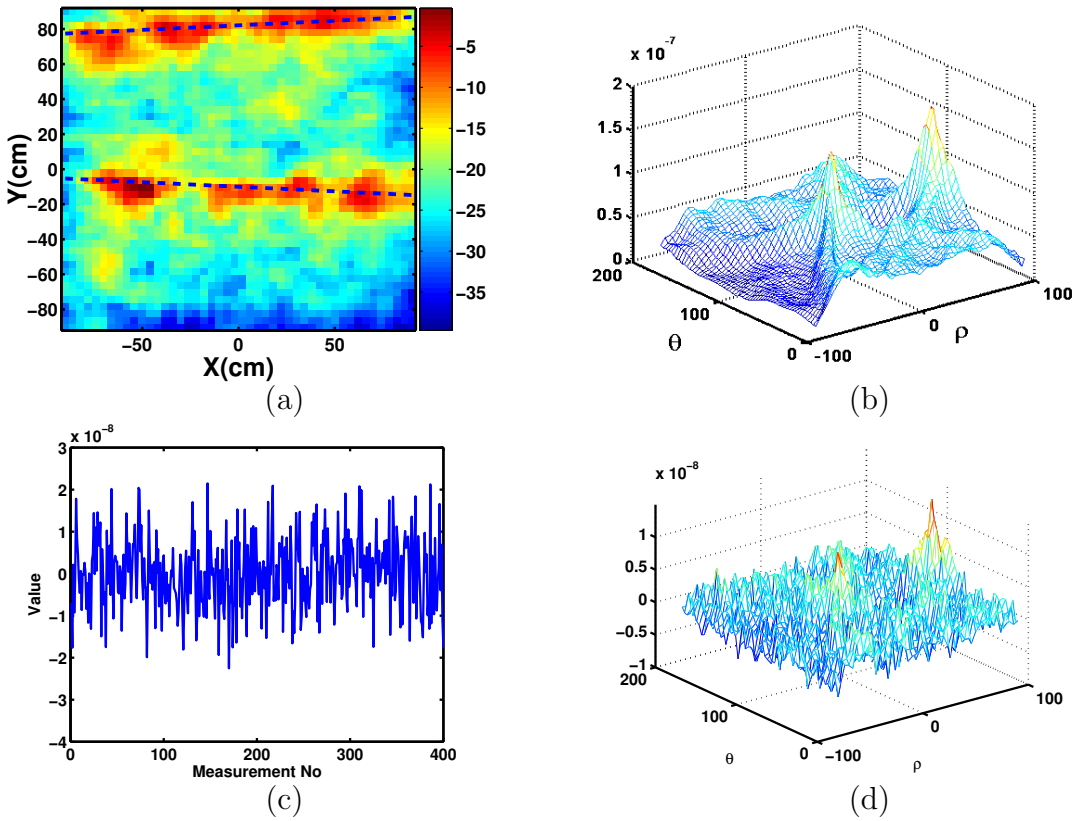

Figure 55: (a) Experimental Backprojected Seismic Image, (b) Hough Transform of the backprojected image, (c) Compressive measurements created by projections of the image in (a) to random Gaussian vectors, (d) The least squares solution.

Instead of using the whole image, 400 compressive samples of the image with random Gaussian vectors are taken for the CS shape detection algorithm. The measurements are shown in Fig. 55(c). The least squares solution with the compressive measurements are given in Fig. 55(d). Although it has higher values close to the true parameter cells, the resultant parameter space is much more cluttered than the HT result.

CS shape detection using the same measurements gives the parameter space shown in Fig. 56. A much cleaner and sparser image than the standard HT is obtained with two peaks only. This way there is no need to search for local maxima in the HT domain to detect the lines. The parameters of the two detected peaks are $\rho = [-10, 82]$ and $\theta = [87, 93]$. The corresponding lines are drawn on the original image in Fig. 55(a).

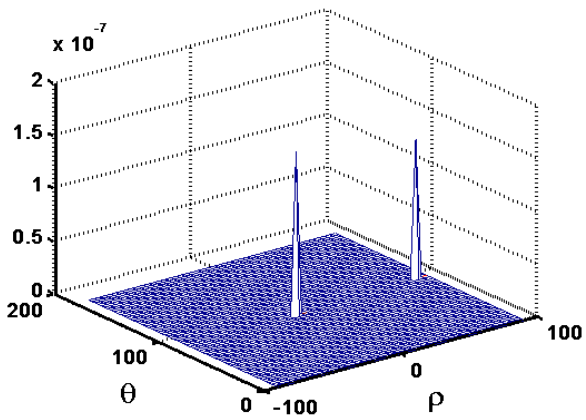

Figure 56: Parameter space created by the CS shape detection algorithm.

Although the resultant parameter space is much sparser than the HT result, we had to compute the subsurface image and then took a small number of projections which seems unnecessary. The next section remedies this nonideal situation by using small number of raw sensor measurements to directly estimate the buried structure parameters.

5.2 Shape Detection Using Compressive Sensor Measurements

Although (55) relates $\boldsymbol{f}$ to $\boldsymbol{p}$, we cannot directly image the target space but can only sense it through sensors like GPR or seismic. To be able to linearly relate $\boldsymbol{p}$ to the sensor measurements $\boldsymbol{\zeta}$, we need the relation between $\boldsymbol{\zeta}$ and $\boldsymbol{f}$. Such a relation depends on the data acquisition process and the target models, and is created by discretizing the target space and synthesizing the GPR model data for each discrete spatial position. Thus, we assume that the targets are combinations of point-like reflectors at discrete spatial positions and these reflectors do not interact so superposition is valid. Representing structures like tunnels with a combination of point reflectors strictly speaking is incorrect, but is done for simplicity. The received data for a point reflector can be easily calculated [53]. The point-like target assumption is not crucial. If the received data can be calculated for other types of target models

like cylinders, then the CS-based ideas presented in this thesis can still be used.

As an example, we develop the $\boldsymbol{f}$-$\boldsymbol{\zeta}$ relation for GPR. The GPR transmissions spanning a region of interest form a synthetic aperture, whose impulse response follows a known curve in the space-time domain. Although the response of actual targets might be more complex, we assume that the received signal at the receiver antenna reflected from a point target at r is a time-delayed and scaled version of the transmitted signal $s(t)$. Thus, the received signal at the GPR receiver antenna can be written as $\zeta_i(t) = As(t - \tau_i(r))$ where $\tau_i(r)$ is the total round-trip delay between the transmitter and the target at position r for the ith aperture point, and A is a scaling factor used to account for attenuation. In our modelling of the received GPR signal, the parameter τ_i is very important and its calculation requires knowledge of the wave velocities in both media as shown in Fig. 57, where the distances $d_{1:4}$ are used to find $\tau_i = (d_1 + d_4)/v_1 + (d_2 + d_3)/v_2$.

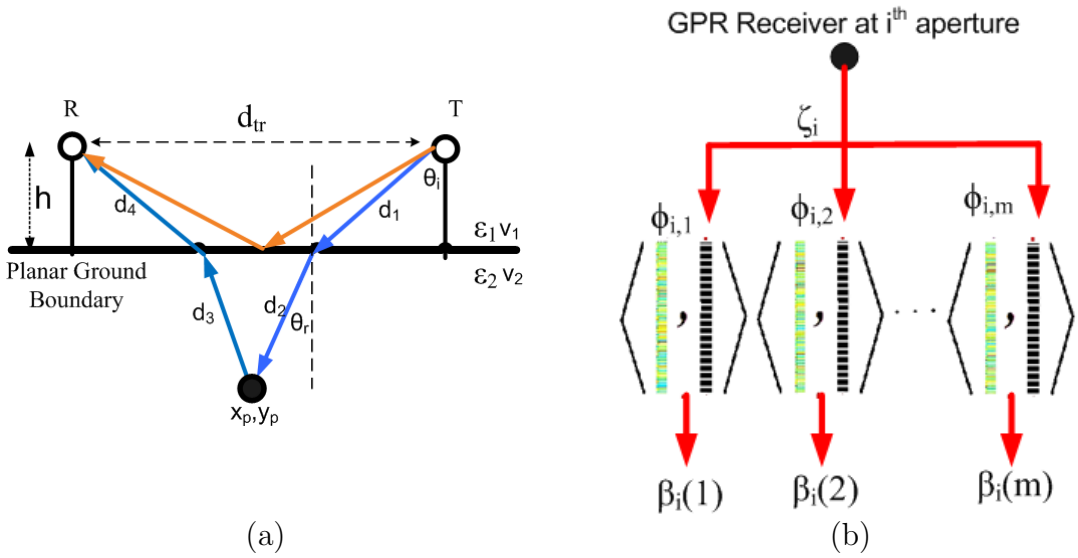

Figure 57: (a) Bistatic GPR measurement scenario, (b) Data Acquisition for GPR at one single aperture point.

To generate the dictionary for the GPR data, the target space $\boldsymbol{\kappa}$ which lies in the product space $[x_i, x_f] \times [y_i, y_f] \times [z_i, z_f]$ is discretized. Here x_i, y_i, z_i and x_f, y_f, z_f denote the initial and final positions of the target space to be imaged along each

axis. Discretization generates the set of possible target points $\mathcal{B} = \{\boldsymbol{\kappa}_1, \boldsymbol{\kappa}_2, \ldots, \boldsymbol{\kappa}_{N_T}\}$, where N_T determines the resolution in the target space and each $\boldsymbol{\kappa}_j$ is a 3D vector $[x_j; y_j; z_j]$.

Using the above model the signal at the GPR antenna can be calculated for a given element of $\mathcal{B}$. This allows us to write a linear relation between the target space indicator $\boldsymbol{b}$ and the measured data at aperture i as

$$\boldsymbol{\zeta}_i = \boldsymbol{\Psi}_i \boldsymbol{b} \tag{63}$$

where the vector $\boldsymbol{b}$ is a weighted indicator function, i.e., a non-zero positive value at index j if $\boldsymbol{b}$ selects a target at $\boldsymbol{\kappa}_j$. In (63), the jth column of $\boldsymbol{\Psi}_i$ is

$$[\boldsymbol{\Psi}_i]_j = \frac{s(t - \tau_i(\boldsymbol{\pi}_j))}{\|s(t - \tau_i(\boldsymbol{\pi}_j))\|_2}. \tag{64}$$

Note that when constructing $\boldsymbol{\Psi}_i$ with (64) each column has unit norm and the spreading factor A doesn't need to be known; only the time delay needs to be calculated.

Using (55) and (63) the measured data can be represented as $\boldsymbol{\zeta}_i = \boldsymbol{\Psi}_i \boldsymbol{H} \boldsymbol{p}$. In the spirit of CS [15, 31], a small number of "random" measurements can carry enough information to reconstruct a signal. Rather than sampling $\boldsymbol{\zeta}_i$ at a high sampling rate, we measure linear projections of $\boldsymbol{\zeta}_i$ onto a second set of basis vectors $\boldsymbol{\phi}_{im}$, $m = 1, 2, ...M$ which can be written in matrix form for the ith aperture point as

$$\beta_i = \boldsymbol{\Phi}_i \boldsymbol{\zeta}_i = \boldsymbol{\Phi}_i \boldsymbol{\Psi}_i \boldsymbol{H} \boldsymbol{p}. \tag{65}$$

The GPR is not directly measuring $\boldsymbol{\zeta}_i$ but only taking inner products of it with the rows of the $\boldsymbol{\Phi}_i$ matrix. The inner product operation can be implemented as shown in Fig. 57(b). Depending on the structure of $\boldsymbol{\Phi}_i$, other implementations can also be used [6, 90].

The result of the CS theory is that the sparse parameter space vector $\boldsymbol{p}$ can be recovered exactly from $M = C\left(\mu^2(\boldsymbol{\Phi}, \boldsymbol{\Psi}\boldsymbol{H}) \log N\right) K$ CS measurements $\boldsymbol{\beta}$ with

overwhelming probability [15], by solving the following ℓ_1 minimization problem

$$\hat{\boldsymbol{p}} = \text{argmin}\, \|\boldsymbol{p}\|_1 \qquad s.t. \quad \boldsymbol{\beta} = \boldsymbol{\Phi}\boldsymbol{\Psi}\boldsymbol{H}\boldsymbol{p} \tag{66}$$

where $\mu(\boldsymbol{\Phi}, \boldsymbol{\Psi}\boldsymbol{H})$ is the coherence between $\boldsymbol{\Phi}$ and $\boldsymbol{\Psi}\boldsymbol{H}$ defined as in [15]. The notations are $\boldsymbol{\beta} = [\boldsymbol{\beta}_1^T, \ldots, \boldsymbol{\beta}_L^T]^T$, $\boldsymbol{\Psi} = [\boldsymbol{\Psi}_1^T, \ldots, \boldsymbol{\Psi}_L^T]^T$, and $\boldsymbol{\Phi} = \text{diag}\{\boldsymbol{\Phi}_1, \ldots, \boldsymbol{\Phi}_L\}$. The optimization problem in (66) is valid for the noiseless case.

Since the GPR signal is generally noisy, we use the stable recovery procedure in [12] that obtains the sparsity pattern vector $\boldsymbol{p}$ by solving the following convex optimization problem

$$\hat{\boldsymbol{p}} = \arg\min \|\boldsymbol{p}\|_1 \qquad \text{s.t.} \quad \|\boldsymbol{A}^T(\boldsymbol{\beta} - \boldsymbol{A}\boldsymbol{p})\|_\infty < \epsilon \tag{67}$$

where $\boldsymbol{A} = \boldsymbol{\Phi}\boldsymbol{\Psi}\boldsymbol{H}$.

5.2.1 Simulation Results

A test example will illustrate the ideas presented in the previous section. A 2-D slice of the target space containing two linear structures with line parameters $(\rho_1, \theta_1) = (-5.2, 44)$ and $(\rho_2, \theta_2) = (2.5, 116)$ is shown in Fig. 58(a). The GPR scans the region with 2 cm spatial resolution at 20 aperture points. Standard time domain GPRs would measure the noisy target space response shown in Fig. 58(b). The signal-to-noise ratio (SNR) is 10 dB. Targets are simulated as a combination of independent point reflectors and the GPR data is generated in MATLAB [52]. To detect the linear features existing methods invert the data to create an image of the target space, and then search the image for features using the HT. The target space image formed with time domain backprojection is shown in Fig. 58(c). The parameter space formed by applying the HT to Fig. 58(c) is shown in Fig. 58(d). Although two peaks corresponding the two targets can be seen, the target space is cluttered since the HT has limited resolution.

Our CS-based method doesn't require sampling of all the space-time domain data. Instead of measuring the space-time domain response at each aperture position, 20

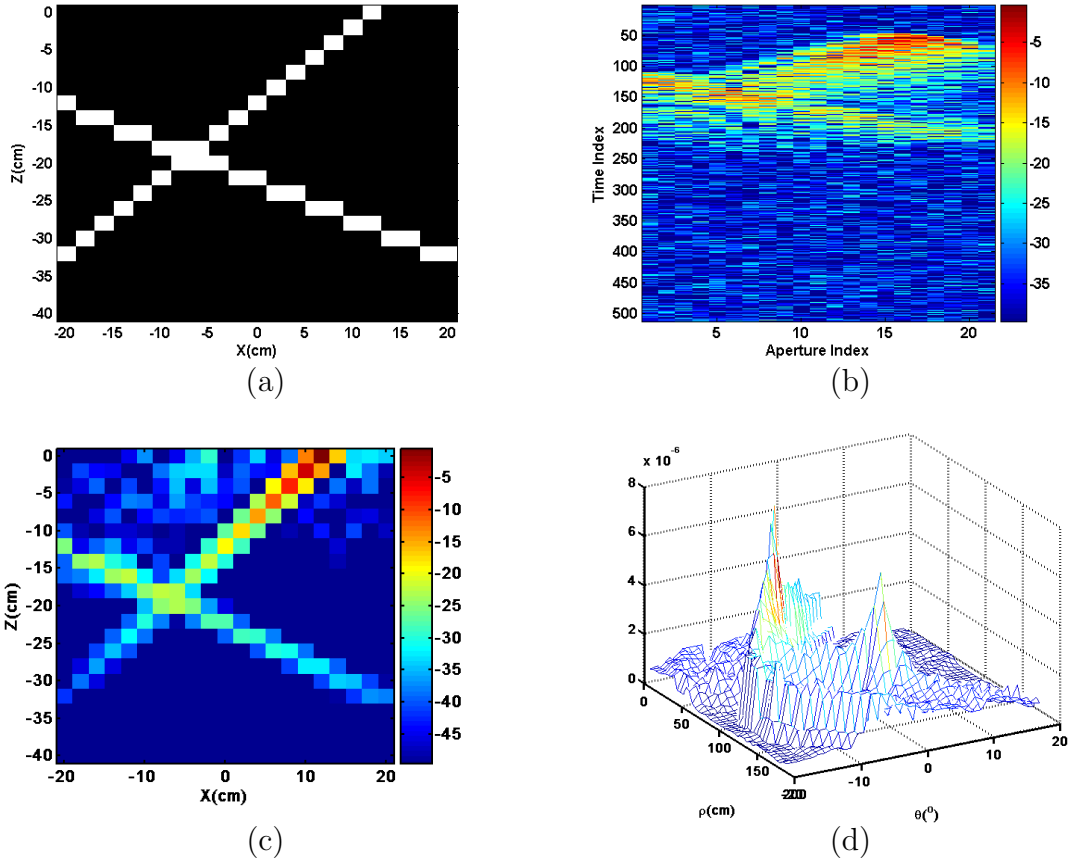

Figure 58: (a) Target space, (b) Noisy space-time domain GPR response, (c) Standard time-domain backprojection algorithm image, (d) HT of the image in (c).

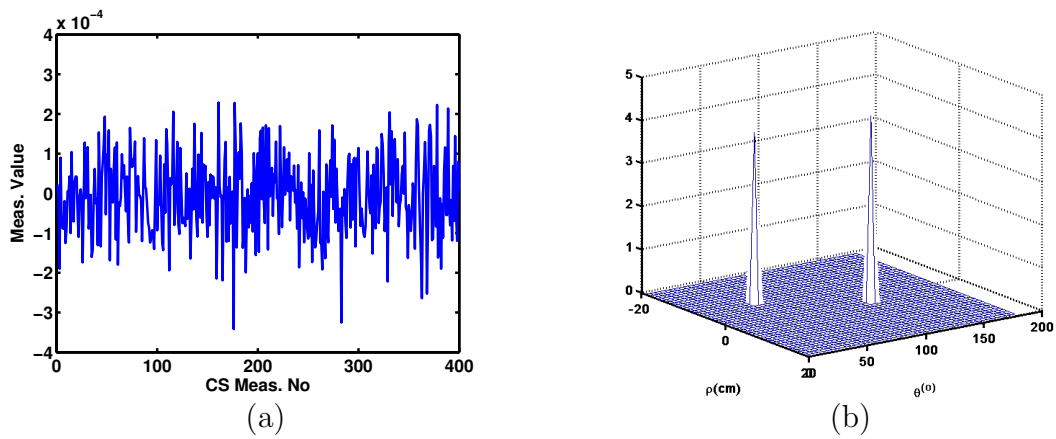

Figure 59: (a) 400 CS measurements, (b) Solution obtained with the proposed method using (67).

inner product measurements are formed at each aperture point making 400 measurements in total for 20 aperture points. This is much less than the 512×20 raw

space-time domain measurements used to make the image in Fig. 58(c). The inner products can be written as the product of the time-domain response with rows of a random matrix $\mathbf{\Phi}_i$ of size 20×512 whose entries are drawn independently from $\mathcal{N}(0, 1/\sqrt{512})$. These 400 measurements, shown in Fig. 59(a), are the only information used to sense the target space area. The number of linear structures is not assumed to be known. The parameter space image created with (67) from the compressive measurements is shown in Fig. 59(b). The CS-based method is able to find the line parameters correctly and directly using a very small number of compressive raw measurements without the image formation step. Also, since the algorithm favors sparse solutions, the resultant parameter space is much sparser than the HT image.

5.2.2 Experimental Results

An experimental scenario has been investigated with scale models of linear structure in an experimental model sandbox [82] filled with nearly-homogeneous sand as shown in Fig. 60(a). In this case, a scale model for a tunnel is buried within a 1.8 m $\times$ 1.8 m region near the center of the tank. The tunnel is 10 cm in diameter and is buried approximately 58 cm deep to give a 20:1 scale model for a shallow tunnel just big enough for a man to slide through. The GPR sensor scans the region with 2 cm spatial resolution, collecting data in the frequency domain. However, for this paper, we inverse transform to create the equivalent time-domain measured data, and at each aperture point we create 20 compressive measurements as projections of the received time-domain responses onto a different random Gaussian measurement matrix.

Figure 60(b) shows the 2-D slice of the backprojected image along the tunnel created using all the space-time domain samples. Solving for the line parameters by the proposed method using the small number of compressed measurements results in the parameter space in Fig. 60(d). The corresponding line is also plotted on the backprojected image. The tunnel could be detected and its parameters are found

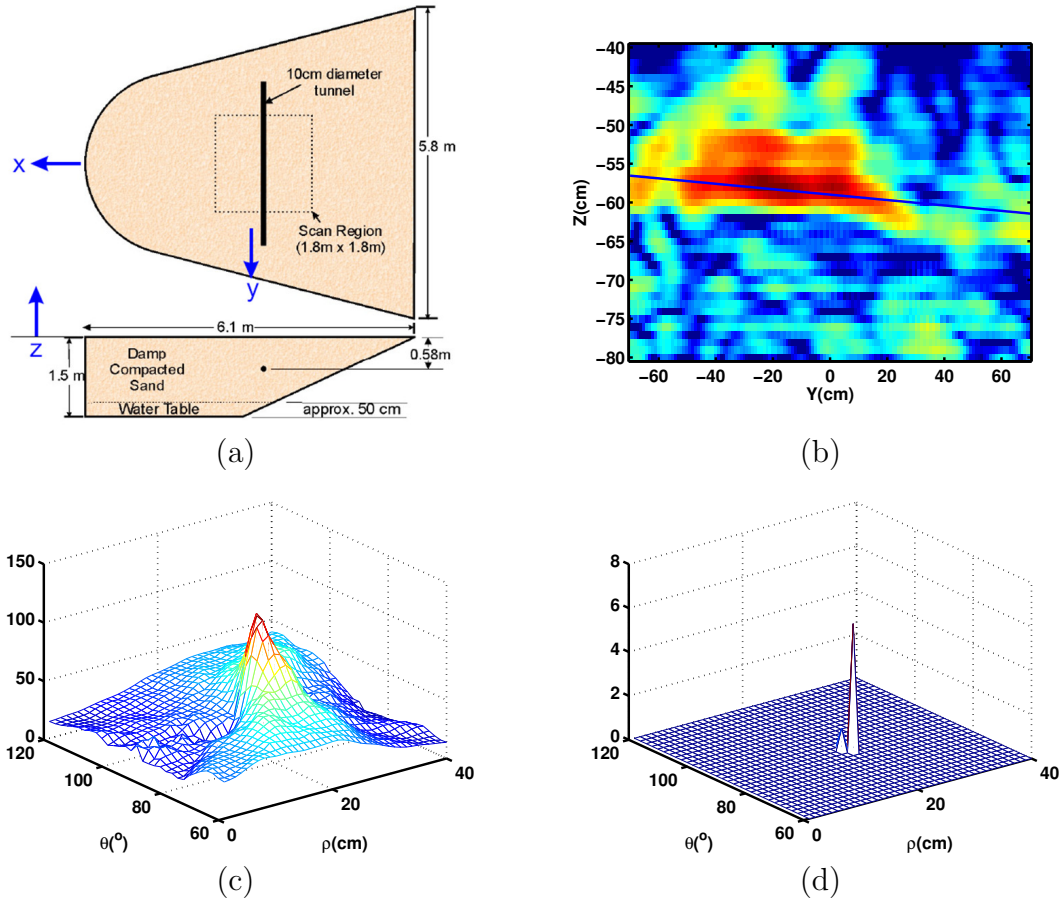

Figure 60: (a) Model in the sand tank of a 10 cm tunnel buried approximately 58–60 cm deep from the surface, (b) Backprojected image using all the space-time raw GPR data. The line drawn is obtained from (d). (c) HT of the image shown in (b), (d) Parameter space obtained by the proposed method.

using a much smaller number of measurements and without the need of creating the image itself.

CHAPTER VI

CONCLUSIONS

The problem of sensing a medium by several sensors and retrieving interesting features is a very general one. The basic framework of the problem is generally the same for applications from MRI imaging, tomography, Radar SAR imaging to subsurface imaging, even though the data acquisition processes, sensing geometries and sensed properties are different. In this thesis we tried to introduce a new perspective to the problem of remote sensing and information retrieval by studying the problem of subsurface imaging using GPR and seismic sensors.

In Chapter 2 we have shown that if the sensed medium is sparse in some domain (i.e., small number of targets) then it can be imaged using many fewer measurements than required by the standard methods now. This leads to much lower data acquisition times and better images representing the medium. We have used the ideas from Compressive Sensing, which show that a small number of "random" measurements about a signal is sufficient to completely characterize it, if the signal is sparse or compressible in some domain. Although we have applied our ideas to the GPR subsurface imaging problem, our results are general and can be extended to other remote sensing applications.

A second objective in remote sensing problems is information retrieval which involves searching for important features in the computed image of the medium. In this thesis we focus on detecting buried structures like pipes, and tunnels. in computed GPR or seismic images. The problem of finding these structures in high clutter and noise conditions, and finding them faster than the standard shape detecting methods like the Hough transform is analyzed in Chapter 3 and 4.

One of the most important contributions of this thesis is in Chapter 5, where the sensing and the information retrieval stages are unified in a single framework using compressive sensing. Instead of taking lots of standard sensor measurements to compute the image of the medium and look for the necessary information in the computed image, a much smaller number of compressed measurements in the form of random projections is taken. The data acquisition and information retrieval stages are unified by using a data model dictionary that connects the information to the sensor data. In this way the information is obtained from a small number of compressed sensor measurements, when the information can be represented sparsely in some domain as in the problem of detecting buried structures.

Future work will include application of sparsity and remote sensing ideas presented in this thesis for the problem of subsurface imaging to a more general framework and different types of problems.

REFERENCES

[1] Aggarwal, N. and Karl, W. C., "Line detection in images through Regularized Hough Transform," *IEEE Trans. on Image Processing*, vol. 15, pp. 582–590, 2006.

[2] Atiquzzaman, M., "Multiresolution hough transform-an efficient method of detecting patterns in images," *IEEE Tran. on Pattern Analysis and Machine Intelligence*, vol. 14, no. 11, pp. 1090–1095, 1992.

[3] Ballard, D. H., "Generalizing the Hough transform to detect arbitrary shapes," *Pattern Recognition*, vol. 13, pp. 111–122, 1981.

[4] Baraniuk, R., "Compressive sensing," *IEEE Signal Processing Magazine*, July 2007.

[5] Baraniuk, R., Davenport, M., DeVore, R., and Wakin, M., "A simple proof of the restricted isometry property for random matrices," *Constructive Approximation*, 2008.

[6] Baraniuk, R. and Steeghs, P., "Compressive radar imaging," in *IEEE Radar Conf.*, pp. 128–133, 2007.

[7] Beylkin, G., "Discrete Radon Transform," *IEEE Trans. Acoustics, Speech, and Signal Processing*, vol. 35, pp. 162–172, 1987.

[8] Boufounos, P., Duarte, M., and Baraniuk, R., "Sparse signal reconstruction from noisy compressive measurements using cross validation," in *Proc. IEEE Workshop on SSP*, August 2007.

[9] Boyd, S. and Vandenberghe, L., *Convex Optimization.* Cambridge University Press, 2004.

[10] Bradley, M., Witten, T., McCummins, R., Crowe, M., Stewart, S., and Duncan, M., "Mine detection with a multi-channel stepped-frequency ground penetrating radar," in *Proc. of SPIE*, vol. 3710, pp. 953–960, 1999.

[11] Breuel, T., "Finding lines under bounded error," *Pattern Recognition*, vol. 29, no. 1, pp. 167–178, 1996.

[12] Candès, E., Romberg, J., and Tao, T., "Stable signal recovery from incomplete and inaccurate measurements," *Comm. on Pure and Applied Math.*, vol. 59, no. 8, pp. 1207–1223, 2006.

[13] Candès, E., Romberg, J., and Tao, T., "Stable signal recovery from incomplete and inaccurate measurements," *Comm. on Pure and Applied Math.*, vol. 59, no. 8, pp. 1207–1223, 2006.

[14] Candes, E. and Tao, T., "The Dantzig Selector: Statistical estimation when p is much larger than n," *Annals of Statistics*, vol. 35, no. 6, pp. 2313–2351, 2007.

[15] Candes, E. J., Romberg, J., and Tao, T., "Robust uncertanity principles: Exact signal reconstruction from highly incomplete frequency information," *IEEE Trans. on Information Theory*, vol. 52, pp. 489–509, 2006.

[16] Candes, E. J. and Tao, T., "Decoding by linear programming," *IEEE Tran. on Information Theory*, vol. 51, pp. 4203–4215, 2005.

[17] Candes, E., "Compressive sampling," in *Proc. of Internaltional Congress of Mathematicians*, Madrid, Spain 2006.

[18] Cands, E., Rudelson, M., Tao, T., and Vershynin, R., "Error correction via linear programming.," in *Proceedings of the 46th Annual IEEE Symposium on Foundations of Computer Science (FOCS)*, pp. 295–308.

[19] Cevher, V., Gurbuz, A. C., McClellan, J. H., and Chellappa, R., "Compressive wireless arrays for bearing estimation," in *ICASSP 2008*, (Las Vegas, Nevada), March 30 –April 4 2008.

[20] Chai, D. and Peng, Q., "Image feature detection as robust model fitting," in *ACCV 7th Asian Conference on Computer Vision*, vol. 3852, pp. 673–682, 2006.

[21] Chen, T. and Chung, K., "A new randomized algorithm for detecting lines," *Real Time Imaging*, vol. 7, pp. 473–481, 2001.

[22] Chen, Y., Yang, Q., Gu, Y., and Yang, J., "Detection of roads in sar images using particle filter," in *Proc. of ICIP*, (Atlanta, GA), pp. 2337–2340, 2006.

[23] Copeland, A. C., Ravichhandran, G., and Trivedi, M. M., "Localized Radon transform-based detection of linear features in noisy images," in *IEEE Computer Society Conference on Computer Vision and Pattern Recognition*, pp. 664–667, 1994.

[24] Counts, T., Gurbuz, A. C., Scott, Jr., W. R., McClellan, J. H., and Kangwook, K., "Multistatic ground-penetrating radar experiments," *IEEE Trans. on Geoscience and Remote Sensing*, vol. 45, no. 8, pp. 2544–2553, Aug. 2007.

[25] Counts, T., Larson, G., Gurbuz, A. C., McClellan, J. H., and W. R. Scott, Jr., "Investigation of the detection of shallow tunnels using electromagnetic and seismic waves," in *Proc. of SPIE*, vol. 6553, May 2007.

[26] Daniels, D. J., "Surface-penetrating radar," *Electronics and Communication Engineering Journal*, vol. 8, pp. 165–182, 1996.

[27] Daniels, D. J., *Surface-penetrating radar.* London : Institution of Electrical Engineers, 1996.

[28] Deans, S. R., *The Radon Transform and some of its applications.* Krieger Publishing, 1993.

[29] Dell'Acqua, A., Sarti, A., Tubaro, S., and Zanzi, L., "Detection of linear objects in GPR data," *Elsevier Signal Processing*, vol. 88, pp. 785–799, 2004.

[30] Donoho, D. and Huo, X., "Beamlets and multiscale image analysis," *Multiscale and Multiresolution Methods, Springer Lecture Notes in Computational Science and Engineering*, vol. 20, pp. 149–196, 2002.

[31] Donoho, D. L., "Compressed sensing," *IEEE Trans. on Information Theory*, vol. 52(4), pp. 1289–1306, 2006.

[32] Donoho, D. L. and Huo, X., "Beamlet pyramids: a new form of multiresolution analysis, suited for extracting lines, curves and objects from very noisy image data," in *SPIE Wavelet applications in signal and image processing VIII*, (San Diego, CA), 2000.

[33] Donoho, D., "Superresolution via sparsity constraints," *SIAM Journal on Mathematical Analysis*, vol. 23, no. 5, pp. 1309–1331, 1992.

[34] Donoho, D., Elad, M., and Temlyakov, V., "Stable recovery of sparse overcomplete representations in the presence of noise," *IEEE Transactions on Information Theory*, vol. 52, no. 1, pp. 6–18, 2006.

[35] Duda, R. O. and Hart, P. E., "Use of Hough transformation to detect lines and curves in pictures," in *Comm. ACM*, vol. 15, pp. 11–15, 1972.

[36] et.al, D. T., "A new compressive imaging camera architecture using optical-domain compression," in *Proc. Comp. Imaging IV at SPIE Electronic Imaging*, 2006.

[37] Feng, X. and Sato, M., "Pre-stack migration applied to GPR for landmine detection," *Inverse Prob.*, vol. 20, pp. 99–115, 2004.

[38] Fischler, M. A. and Bolles, R. C., "Random sample consensus: a paradigm for model fitting with applications to image analysis and automated cartography," *Comm. ACM*, vol. 24, pp. 381–395, 1981.

[39] Frye, G. and Nahman, N., "Random sampling oscillography," *IEEE. Trans. Instrumentation and Measurement*, pp. 8–13, March 1964.

[40] Gader, P. D., Mystkowski, M., and Zhao, Y., "Landmine detection with ground penetrating radar using Hidden Markov Models," *IEEE Trans. Geoscience and Remote Sensing*, vol. 39, pp. 1231–1244, 2001.

[41] Gamba, P. and Lossani, S., "Neural detection of pipe signatures in ground penetrating radar images," *IEEE Trans. Geoscience and Remote Sensing*, vol. 38, pp. 790–797, 2000.

[42] Gazdag, J., "Wave equation migration with the phase shift method," *Geophysics*, vol. 43, pp. 1342–1351, 1978.

[43] Grandjean, G., Gourry, J., and Bitri, A., "Evaluation of gpr techniques for civil-engineering applications: study on a test site," *Journal of Applied Geophysics*, vol. 45, no. 3, pp. 141–156, 2000.

[44] Grant, M. and Boyd, S., "Cvx: Matlab software for disciplined convex programming (web page and software)," http://stanford.edu/ boyd/cvx.

[45] Groenenboom, J. and Yarovoy, A., "Data processing and imaging in gpr system dedicated for landmine detection," *Subsurface Sensing Technologies and Applications*, vol. 3, no. 4, pp. 387–402, 2002.

[46] Gurbuz, A. C., Cevher, V., and McClellan, J. H., "A compressive beamformer," in *ICASSP 2008*, (Las Vegas, Nevada), March 30 –April 4 2008.

[47] Gurbuz, A. C., Counts, T., Kim, K., McClellan, J. H., and W. R. Scott, Jr., "Application of multistatic inversion algorithms to landmine detection," in *Detection and Remediation Technologies for Mines and Minelike Targets XI, Proc. of SPIE*, vol. 6217, May 2006.

[48] Gurbuz, A. C. and McClellan, J. H., "Iterative detection of linear objects in GPR and seismic images," in *IEEE Workshop on Sensor Array and Multichannel Signal Processing*, pp. 118–121, July 2006.

[49] Gurbuz, A. C., McClellan, J. H., and Scott, Jr., W. R., "Predicting gpr target locations using time delay differences," in *Proc. SPIE Detection and Remediation Technologies for Mines and Minelike Targets XI*, vol. 6217, 2006.

[50] Gurbuz, A. C., McClellan, J. H., and Scott, Jr., W. R., "Feature detection in highly noisy images by random sample theory," in *15th International Conference on Digital Signal Processing*, July 2007.

[51] Gurbuz, A. C., McClellan, J. H., Scott, Jr., W. R., and Larson, G. D., "Seismic Tunnel Imaging and Detection," in *ICIP 2006*, pp. 3229–3232, 8-11 Oct. 2006.

[52] Gurbuz, A. C., McClellan, J. H., and W. R. Scott, Jr., "Subsurface target imaging using a multi-resolution 3d quadtree algorithm," in *Detection and Remediation Technologies for Mines and Minelike Targets X, Proc. of SPIE*, vol. 5794, pp. 1172–1181, June 2005.

[53] Gurbuz, A., McClellan, J. H., and Scott, W., "Compressive Sensing for GPR Imaging," in *Asilomar Conf.*, 2007.

[54] Hansen, K. V. and Toft, P., "Fast curve estimation using preconditioned generalized Radon transform," *IEEE Trans. Image Processing*, vol. 5, pp. 1651–1661, 1996.

[55] Haupt, J. and Nowak, R., "Signal reconstruction from noisy random projections," *IEEE Trans. on Information Theory*, vol. 52, no. 9, pp. 4036–4048, 2006.

[56] Hough, P. V. C., "A Method and Means for Recognizing Complex Patterns," in *US Patent 3069654*, Dec. 1962.

[57] Hubbard, S., Jinsong, C., Williams, K., Rubin, Y., and Peterson, J., "Development status of a stepped frequency ground penetrating radar," in *Proc. of SPIE*, vol. 1942, pp. 34–40, 1993.

[58] Hubbard, S., Jinsong, C., Williams, K., Rubin, Y., and Peterson, J., "Environmental and agricultural applications of gpr," in *Proc. of IWAGPR 05*, pp. 45–49, 2005.

[59] Iizuka, K., Freundorfer, A., Wu, K., Mori, H., Ogura, H., and Nguyen, V., "Step frequency radar," *Journal of Applied Physics*, vol. 56, no. 9, pp. 2572–2583, 1984.

[60] Illingworth, J. and Kittler, J., "The adaptive hough transform," *IEEE Tran. on Pattern Analysis and Machine Intelligence*, vol. 9, no. 5, pp. 690–698, 1987.

[61] Illingworth, J. and Kittler, J., "A survey of the Hough Transform," *Computer Vision, Graphics and Image Processing*, vol. 44, pp. 87–116, 1988.

[62] Johansson, E. M. and Mast, J. E., "Three dimensional ground penetrating radar imaging using a synthetic aperture time-domain focusing," in *Proc. SPIE Conference on Advanced Microwave and Millimeter Wave Detectors*, vol. 2275, pp. 205–214, 1994.

[63] Kahrs, M., "50 years of rf and microwave sampling," *IEEE Tran. on Microwave Theory and Techniques*, vol. 51, no. 6, pp. 1787–1805, 2003.

[64] Kim, K., Gurbuz, A. C., McClellan, J. H., and Scott, Jr., W. R., "A multi-static ground-penetrating radar with an array of resistively loaded vee dipole antennas for landmine detection," in *Detection and Remediation Technologies for Mines and Minelike Targets X, Proc. of SPIE*, vol. 5794, pp. 495–506, June 2005.

[65] Kim, K. and Scott, Jr., W. R., "Improved resistively-loaded vee dipole for ground-penetrating radar applications," in *IEEE Antennas and Propagation Society International Symposium*, vol. 3, pp. 2548–2551, 2004.

[66] Kim, K. and Scott, Jr., W. R., "Design of a resistively-loaded vee dipole for ultra-wideband ground-penetrating radar applications," *IEEE Trans. Antennas and Propagation*, vol. 53, 2005.

[67] Kiryati, N., Eldar, Y., and Bruckstein, A. M., "A probabilistic Hough transform," *Pattern Recognition*, vol. 24, pp. 303–316, 1991.

[68] Kiryati, N., Kalviainen, H., and Alaoutinen, S., "Randomized and probabilistic Hough transform: unified performance evaluation," *Pattern Recognition Letters*, vol. 21, pp. 1157–1164, 2000.

[69] Li, H., Lavin, M., and Master, R. L., "Fast hough transform: A hierarchical approach," *Computer Vision, Graphics and Image Processing*, vol. 36, pp. 139–161, 1986.

[70] Liu, R., Ruan, Z., and Wei, S., "Line detection algorithm based on random sample theory," in *SPIE Second International Conf. on Image and Graphics*, vol. 4875, 2002.

[71] Lobo, M., Vandenberghe, L., Boyd, S., and Lebret, H., "Applications of second-order cone programming," *Linear Algebra Its Applicat.*, no. 284, pp. 193–228, 1998.

[72] Lustig, M., Donoho, D., and Pauly, J. M., "Sparse MRI: The application of compressed sensing for rapid MR imaging," *Preprint*, 2007.

[73] Malioutov, D., Cetin, M., and Willsky, A., "A sparse signal reconstruction perspective for source localization with sensor arrays," *IEEE Tran. on Signal Proc.*, vol. 53, no. 8, pp. 3010–3022, 2005.

[74] Matas, J., Galambos, C., and Kittler, J., "Robust detection of lines using the progressive probabilistic Hough transform," *Computer Vision and Image Understanding*, vol. 78, pp. 119–137, 2000.

[75] Metje, N. and et. al, "Mapping the underworld- state of the art review," *Tunneling and underground space technology*, vol. 22, pp. 568–586, 2007.

[76] Oh, S.-M., *Iterative space-time domain fast multiresolution SAR imaging algorithms*. PhD thesis, Georgia Institute of Technology, Atlanta, GA, 2001.

[77] Olson, C., "Locating geometric primitives by pruning the parameter space," *Pattern Recognition*, vol. 34, pp. 1247–1256, 2001.

[78] Romberg, J., "l1-magic," http://www.acm.caltech.edu/l1magic/.

[79] Sachs, J., "M-sequence ultra-wideband-radar: state of development and applications," in *Radar Conf.*, pp. 224–229, 2003.

[80] Schneider, W., "Integral formulation of migration in 2 and 3 dimensions," *Geophysics*, vol. 43, pp. 49–76, 1978.

[81] Sciotti, M., Colone, F., Pastina, D., and Bucciarelli, T., "Gpr for archaeological investigations: real performance assesment for different surface and subsurface conditions," in *Proc. of IGARSS 03*, pp. 2266–2268, 2003.

[82] Scott, Jr., W. R., Counts, T., Larson, G. D., Gurbuz, A. C., and McClellan, J. H., "Combined ground penetrating radar and seismic system for detecting tunnels," in *IEEE IGARSS*, pp. 1232–1235, July 2006.

[83] Scott, Jr., W. R., Kim, K., Larson, G. D., Gurbuz, A. C., and McClellan, J. H., "Combined seismic, radar, and induction sensor for landmine detection," in *Geoscience and Remote Sensing Symposium*, vol. 3, pp. 1613–1616, 2004.

[84] Shope, S. and Greenfield, R. J., "Electromagnetic cross-hole tomography for tunnel detection," in *Third Technical Symposium on Tunnel Detection Proceedings*, pp. 123–136, 1988.

[85] Steinway, W. and Barrett, C., "Development status of a stepped-frequency ground penetrating radar," in *Proc. of SPIE*, vol. 1942, pp. 34–43, 1993.

[86] Stolt, R., "Migration by Fourier Transform," *Geophysics*, vol. 43, pp. 23–48, 1978.

[87] Toft, P., *The Radon Transform Theory and Implementation.* PhD thesis, Technical University of Denmark, Lyngby, Denmark, 1996.

[88] Toft, P., "Using the generalized Radon transform for detection of curves in noisy images," in *ICASSP-2006*, vol. 4, pp. 2219–2222, 1996.

[89] Toft, P. and Hansen, K. V., "Fast Radon transform for detection of seismic reflections," in *In Signal Processing VII - Theories and Applications EURASIP EUSIPCO94*, vol. 1, pp. 229–232, 1994.

[90] Tropp, J., Wakin, M., Duarte, M., Baron, D., and Baraniuk, R., "Random filters for compressive sampling and reconstruction," in *ICASSP-2006*, vol. 3, pp. 872–875, 2006.

[91] Xu, L. and Oja, E., "Randomized Hough Transform (RHT): Basic mechanisms, algorithms, and computational complexities," *CVGIP: Image Understanding*, vol. 57, pp. 131–154, 1993.

[92] Xu, L., Oja, E., and Kultanan, P., "A new curve detection method: Randomized Hough Transform (RHT)," *Pattern Recognition Letters*, vol. 11, pp. 331–338, 1990.

VITA

Ali Cafer Gurbuz was born in Doganhisar, Konya, Turkey in July 1981. He received his B.S. degree from Bilkent University, Ankara, Turkey in 2003 and M.S. degree from Georgia Institute of Technology in 2005 both in Electrical Engineering. He will receive his PhD degree from the Georgia Inst. of Technology Dept.of Electrical and Computer Engineering in summer 2008. His research interests include compressive sensing, fast feature detection techniques, array signal processing, ground penetrating radar applications.